Universitá degli studi di Perugia
Dottorato di ricerca in Fisica
XX Ciclo

High Charge Cosmic Rays Measurement with the AMS-02 Silicon Tracker

Dott. Alberto Oliva

Tutori:
Prof. Bruna Bertucci
Dott. Paolo Zuccon

Coordinatore del corso di Dottorato:
Prof. Maurizio Busso

A.A. 2006/07

Contents

Introduction

Cosmic Rays (CR) are high energy particles reaching the Earth atmosphere from space in all directions. The origins of these particles range from energetic processes in the Sun (solar CRs with energies up to the MeV) to neutron rotating stars, supernovae and astrophysical objects in our Galaxy (galactic CRs with energies 10^7–10^{17}eV) all the way to unidentified extragalactic sources of the ultra high energy cosmic rays reaching energies up to 10^{20} eV.

The main components of galactic cosmic rays are protons (~ 90 %) and Helium nuclei (~ 9 %); the remaining ~ 1 % is composed by electrons, fully ionized nuclei and traces of anti-matter (positrons, antiprotons) produced in the interaction of the CRs with the interstellar medium.

The chemical and isotopic composition as well as the differential energy spectrum of the Galactic Cosmic Rays Nuclei (GCRN) in the Earth proximity carry important information both on their origin (sources and acceleration mechanisms) and on the properties of the interstellar medium where they are transported in their journey to the Earth (galactic magnetic fields, interstellar matter density, diffusion mechanisms). Therefore, accurate measurements of the GCRN properties contribute not only to a deeper understanding of their astrophysical source characteristics but also to a better modeling of the CR propagation in the galaxy, as needed in order to assess the existence of primary sources of anti-matter in the CR flux due to dark-matter annihilation signals.

The GCRN flux intensity is of the order of 1 $(\mathrm{m}^2\ \mathrm{sr\ s\ GeV/n})^{-1}$ at kinetic energies of ~ 1 GeV/n, and decreases with a power law down to $\sim 10^{-6}$ $(\mathrm{m}^2\ \mathrm{sr\ s\ GeV/n})^{-1}$ at TeV/n: a large acceptance and a long exposure time are the key points to perform the GCRN energy spectrum measurement with high statistical accuracy.

The Alpha Magnetic Spectrometer (AMS-02) is a large acceptance (0.45 m^2sr) and long duration (3 years) space experiment, which aims to perform a precise measurement of the galactic CRs components in the rigidity range between 0.5 GV and 3.7 TV [1]. The AMS-02 detector has been designed to measure the most rare components of the cosmic rays searching for the presence of primordial anti-matter nuclei and for signals from the dark matter component of the Universe. AMS-02 will also perform a very accurate measurement of the GCRN differential energy spectrum in the GeV–TeV energy range, providing an excellent chemical element separation up to Iron and isotopic identification up to Beryllium at energies below 10 GeV/n.

Ion energies are evaluated from the bending of their trajectories in the AMS-02 magnetic field: eight layers of double sided silicon microstrip sensors are used to determine with an accuracy of 5 (20) μm in the bending (not-bending) coordinate the ion transit position. The simultaneous measurement of the ionization energy loss in the different layers accurately determines the ion absolute charge value.

In this thesis, the response of the AMS-02 Silicon Tracker elements, the *ladders*, to $Z > 2$ nuclei has been studied by means of a detailed analysis of ion beam test data recorded with six flight spare ladders. A set of algorithms to optimize the spatial resolution and the ion charge identification has been developed and tested against the data. Modeling of the nuclear fragmentation within the detector has been also investigated by means of a FLUKA-based Monte Carlo simulation of the beam test setup.

The outline of the thesis is as follows:

Chapter 1: a brief review of the CR physics is given and the relevance of GCRN measurements in different astrophysical topics is discussed. Experimental techniques for GCRN detection are then introduced and the actual experimental status in the direct GCRN measurements presented.

Chapter 2: A general overview of the AMS-02 detector is followed by a more detailed description of the techniques adopted in AMS-02 for GCRN energy spectra and composition measurements. The expected AMS-02 performances in the GCRN fluxes measurements are also discussed.

Chapter 3: The working principles of double sided Silicon microstrip sensors are discussed and the solutions implemented in the AMS-02 Tracker are presented. The beam test setup and the data sets used for our analysis are then described.

Chapter 4: The analysis of the detector response to ions is presented both in terms of charge collection and spatial resolution on the two sensors sides. Results from likelihood-based charge identification algorithms are used to estimate the charge separation power in the AMS-02 Tracker. The charge based association algorithm used to reconstruct 3D hits from the signals collected on the two sensors sides is then presented.

Chapter 5: Ion fragmentation occurrence in AMS-02 ladders is measured and compared with a simulation developed in the FLUKA framework. Details on the event selection and MC simulation are given.

Chapter 1

Cosmic Rays Nuclei

Cosmic Rays (CR) are charged particles reaching the Earth atmosphere in all directions from the outer space. Protons and helium nuclei constitute $\sim 99\%$ of the whole CR flux: completely ionized stable nuclei of higher charge ($Z > 2$), electrons and faint traces of anti-matter particles account for the remaining flux components. Galactic astrophysical sites are the sources of CRs with energies between 10^9–10^{18}eV/n. Cosmic ray particles are energized by shock waves, as in supernova explosions, and confined by galactic magnetic fields during a journey of ~ 10 Myr before their arrival to the Earth. As they wonder in the galaxy, CRs might experience re-accelerations and interact with the inter-stellar medium: as a result CR original energy spectrum and composition are modified. Detailed measurements of the energetics, chemical and isotopic composition of the CR nuclear species, as well as of the ISM properties, are key ingredients to trace-back and clarify the major steps of the all-species galactic cosmic rays life.

A general overview on CRs basic figures will be given in the first part of this chapter. Then, discussion will be focused on the chemical composition of Galactic CRs and on the astrophysical implications of their isotopic abundances. Finally, experimental direct measurements of nuclear cosmic rays at intermediate energies will be reviewed.

1.1 Cosmic Rays

The CR energies span over a very wide interval: ~ 20 orders of magnitude from eV to 10^{21}eV. Correspondingly, the all-species CR differential fluxes vary from particle/cm^2/second/MeV to 1 particle/km^2/century/ZeV (figure 1.1).

CRs with the lowest energy have a solar origin and make up solar wind.

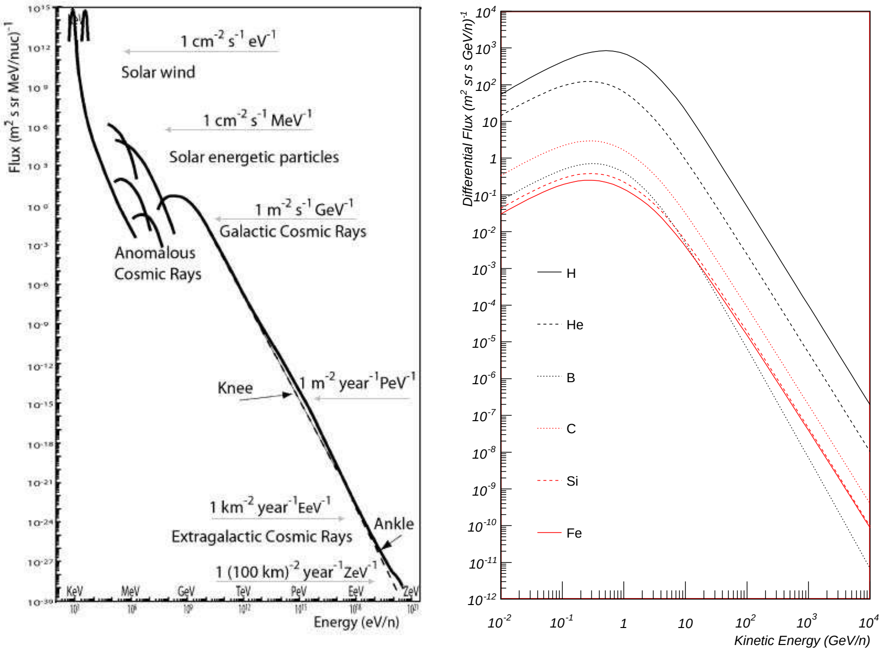

Figure 1.1: Left: The observed energy spectrum for the all-species CRs [2]. Flux in the energetic interval from 10^{11} to 10^{20} eV can be expressed by a power law with a slight change of slope around 10^{15} eV (knee) and 10^{19} eV (ankle). The integral fluxes above the *knee* and the *ankle* are approximately 1 particle/m^2/year and 1 particle/km^2/year. Right: The standard model spectrum below the knee for some specific Galactic CRs chemical species as calculated by a GALPROP simulation [3].

Solar CRs, also known as *Solar Energetic Particles* (SEP), are transient phenomena originated mostly from solar flares explosions or by Coronal Mass Ejections (CME). SEP have energies up to several hundred MeV/n, sometimes up to few GeV/n, and their abundances are strongly related to the solar cycle variation. The solar termination shocks in the interplanetary medium is also at the origin of the so called *Anomalous* CRs with typical energies of ~ 10 MeV/n. These are mainly interstellar nuclei with high ionization potential (He, N, O, Ne, Ar), entering as neutral particles in the solar system, being subsequently ionized and accelerated in the solar termination shock.

CRs rays with energy between 10^9 eV/n and 10^{18} eV/n are assumed to originate in the Milky Way and accelerated in supernova explosions occurring in the Galaxy [4]. In this picture, particles are scattered across the shock fronts of the SN, gaining energy at each crossing by the first order Fermi process [5]. This acceleration model is strongly supported by recent observations of γ-ray emission from SN remnants revealing the presence of energetic particles near these objects [6]. After acceleration, particles propagate in the Galaxy, confined by the randomly oriented galactic magnetic fields ($\sim$ 3µG), for an average time of $\sim$ 15 Myr before reaching Earth [7].

The low energy GCR flux in the Earth proximity is strongly influenced by the solar and terrestrial environments. The interstellar CRs reaching the solar system are *modulated* by the solar wind, the expanding magnetized plasma generated by the Sun, which decelerates and partially excludes the lower energy galactic cosmic rays from the inner solar system. There is a significant anti-correlation between solar activity (which has an alternating eleven-year cycle) and the intensity of the cosmic rays with energies below 10 GeV. In addition, the lower-energy cosmic rays are affected by the geomagnetic field, which they must penetrate to reach the top of the atmosphere. Thus the intensity of any component of the cosmic radiation in the GeV range depends on both location and time.

The inter-stellar Galactic Cosmic Rays (GCR) spectrum is described by a power law $\Phi = \Phi_0(E/\mathrm{TeV})^{-\gamma}$ $(\mathrm{m}^2\ \mathrm{s}\ \mathrm{sr}\ \mathrm{TeV})^{-1}$, where the spectral index γ takes values from 2.5 to 2.8 for the different atomic species.

At energies $\sim 10^{15}$ eV the CRs spectrum has a steeping, the *knee*, characterized by a sudden variation of the all-species spectral index from 2.7 to 3.1. Two main effects are believed to be at the origin of the knee: (a) the reach of the maximum energy transferable by the cosmic accelerators; (b) with increasing energy the galactic magnetic confinement becomes less and less efficient, corresponding to a CRs leakage from the Galaxy. Since these two processes depend on the magnetic rigidity of the particle, the energy spectra for individual elements should exhibit a break at energies being proportional to the elemental charge [8]. Recently the energy spectra of five elemental groups, derived by the KASKADE collaboration, exhibit the individual separated knees [9].

At higher energies the transition occurs between galactic and extra-galactic origin of the CR fluxes: two breaks, a *second knee* and the *ankle*, are observed in the spectrum at $E \sim 10^{17}$ eV and $E \sim 10^{18}$ eV respectively. Historically, the overtaking of an extragalactic CRs population of higher energy over the GCRs has been originally related to the *ankle*. As the experimental evidence for the *second knee* consolidated [10], different scenarios have been postulated. In the *ankle* region, a dip structure has been predicted due to the energy losses related to e^+e^- pair production of extragalactic protons in the interactions on the 2.7 K Cosmic Microwave Background radiation (CMB)

[11]. In this picture, the most likely explanation of the second knee would be the termination of the galactic cosmic ray flux, the ankle being a feature of the extragalactic flux component.

The nature and the origin of Ultra-High-Energy Cosmic Rays (UHECRs), which are observed at the extreme energies $E > 10^{19}$eV, are as of today under a quite lively debate. Not only the cosmological sources and acceleration mechanisms that could produce such energetic particles are still unclear, but even their possibility to reach us is highly suppressed due to their inelastic interaction (π production) with the CMB, which suggests a drastic flux reduction at the Greisen-Zatsepin-Kuzmin (GZK) cut-off limit [12]. In recent years, overabundance of UHECR particles has been experimentally measured by the Japanese experiment AGASA [13] in contrast with results from the HiRes collaboration [14]. However, a detailed re-analysis of AGASA excess and the latest results from the ongoing Pierre Auger Observatory (PAO) project [15] seem to confirm the GZK effect. Recent PAO results point out to possible correlations between the UHECRs incoming direction and astrophysical sources: UHECRs have such large energy that their propagation is not influenced by the galactic magnetic field and this actually can open a new vision in the astronomy with Cosmic Rays.

1.2 Galactic Cosmic-Rays Nuclei

Chemical composition of CR nuclei spans over the whole periodic table, with relative abundances of different components reflecting their origin. The Big Bang Nucleosynthesis (BBN), occurred in the early Universe [16], is at the origin of the light elements: Hydrogen (H, D, ^{3}H), Helium (^{3}He, ^{4}He) and Lithium (^{6}Li, ^{7}Li) isotopes. Heavier elements up to Nickel, with a prevalence of the Carbon, Oxygen and Nitrogen group, are synthesized in the stellar evolution by the nuclear fusion of lighter elements in the star core (Star Nucleosynthesis). Elements above Iron are typically produced by fast fusion during supernova explosion (Explosive Nucleosynthesis).

Different time delays between production and accelerations are expected depending on the distance between the production and the accelerator sites: nuclei produced in supernovae or super-bubbles are close to the acceleration places, while stellar matter or interstellar dust and gas must be transported by flares or winds towards astrophysical accelerators.

After acceleration, GCRs spend a substantial part of their life in the Galaxy, confined by the galactic magnetic field. The simplest description of this phase, the leaky-box model [17], assumes a galaxy with uniform density from which cosmic rays escape or *leak out* with an energy-dependent proba-

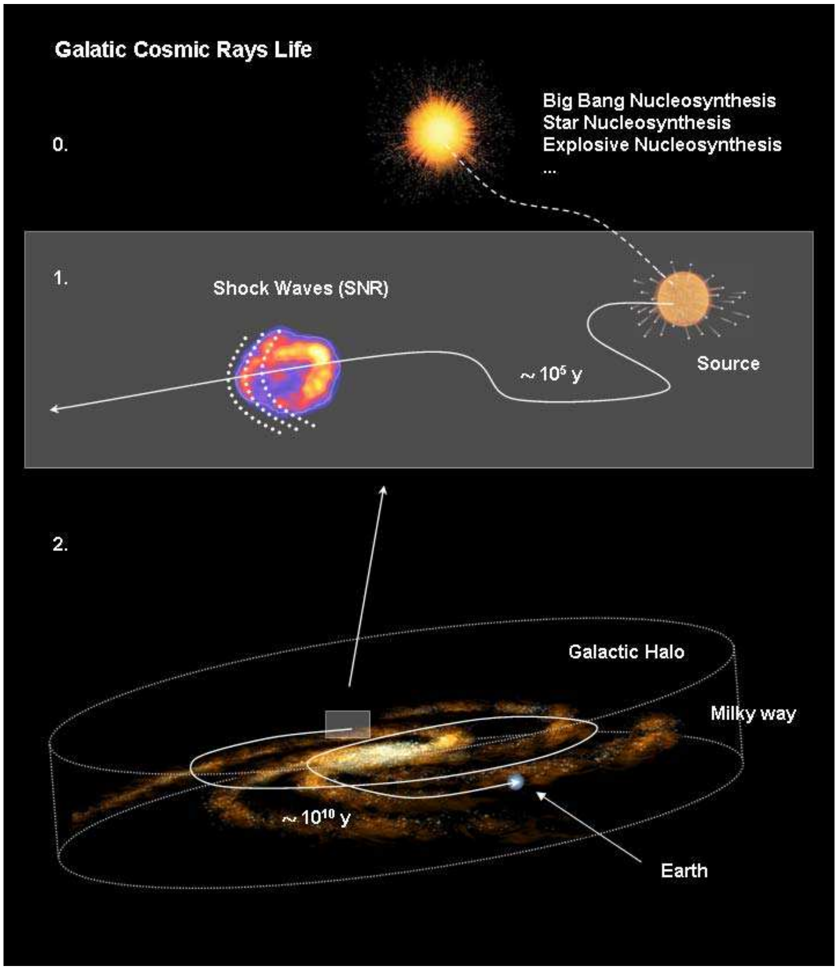

Figure 1.2: A schematic view of the Galactic cosmic-ray nucleus life. Step 0: The nucleus is synthesized by BBN, or in a stellar process; Step 1: the injection in the astrophysical accelerator can be due to SN explosion, solar flares or simply by solar winds; Step 2: after the acceleration GCR wonders in the Galaxy trapped by the magnetic field for $\sim$ 10 billions years. In this interval the composition and energetics of the CRs change, due to the spallation processes. In particular *secondary* nuclei are freshly produced in the spallation processes, whereas *primary* CR nuclei preserve their identity after nuclear interactions.

bility per unit time. More realistic models account for the actual structure of the Galaxy, incorporating both a high-density central disk and a low density halo and transport mechanisms within the Local Bubble. In this phase CRs might lose or gain energy, their initial spectra and composition can change, they can produce secondary particles and γ-rays. All these effects, enter explicitly in the current *diffusion models* where a steady-state equilibrium of the CR distribution in the galaxy is obtained taking into account galactic wind (convection), diffusive reacceleration in the ISM, energy losses, nuclear fragmentation and decay, as described by the transport equation:

$$\begin{aligned}\frac{\partial\psi}{\partial t} &= q(\vec{r},p) + \vec{\nabla}\cdot(D_{xx}\vec{\nabla}\psi - \vec{V}\psi) + \frac{\partial}{\partial p}p^2 D_{pp}\frac{\partial}{\partial p}\frac{1}{p^2}\psi + \\ &- \frac{\partial}{\partial p}\left[\dot{p}\psi - \frac{p}{3}(\vec{\nabla}\cdot\vec{V})\psi\right] - \frac{1}{\tau_f}\psi - \frac{1}{\tau_r}\psi\end{aligned}$$

- $\psi(\vec{r};p;t)$ is the density per unit of total particle momentum with $\psi(p)dp = 4\pi p^2 f(\vec{p})$ in terms of the phase-space density $f(\vec{p})$;
- $q(\vec{r};p)$ is the source term;
- D_{xx} is the spatial diffusion coefficient;
- $\vec{V}$ is the convection velocity;
- D_{pp} reacceleration described as diffusion in momentum space;
- $\dot{p}$ is the momentum loss rate described for nucleons by ionization and Coulomb interactions, and for electrons by ionization, Coulomb interactions, bremsstrahlung, inverse Compton, and synchrotron;
- τ_f is the time scale for fragmentation
- τ_r is the time scale for the radioactive decay

Different approaches can be found in literature in solving the transport equation [18], and different computational techniques have been developed for a customizable treatment of the GCRs propagation for different species (i.e. GALPROP [3]). Nevertheless, the difficulty to disentangle experimentally measurable effects due to a single physics process, results in an effective degeneracy of the parameters that rule these models.

Several complementary constraints on GCR sources and propagation can be extracted from the measurement of their chemical and isotopic composition: they will be reviewed in the following sections.

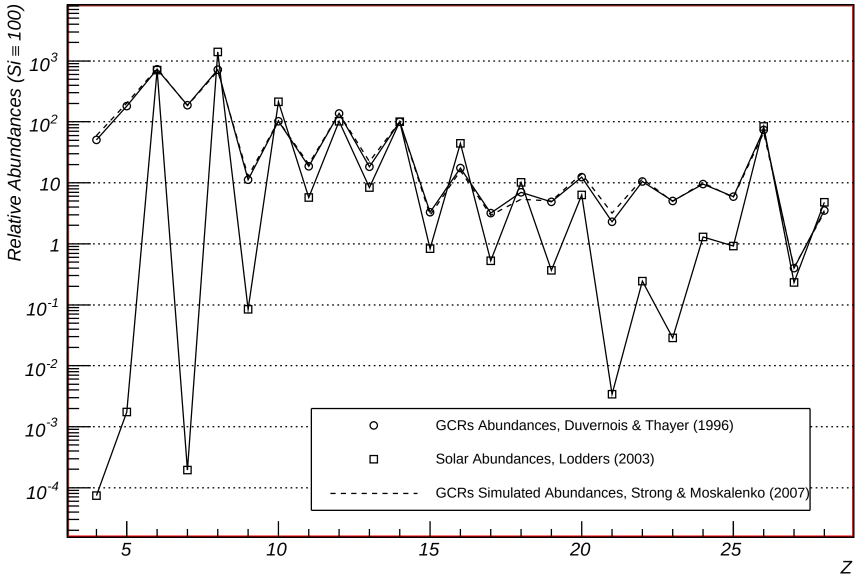

Figure 1.3: The relative abundances for GCRs: real [19], and simulated [20] compared to the solar system [21] ones. The differences between the two chemical composition are the fingerprint of secondary CRs, as the Beryllium, Boron and sub-Iron group.

1.3 Primary and Secondary CRs Physics

The *primary* galactic CRs nuclei are accelerated at astrophysical sources. Their energy spectra and chemical composition are modified from the astrophysical sources to the Earth by the spallation processes on the Inter-Stellar Medium (ISM) producing *secondary* CRs. Electrons, Protons and Helium, as well as Carbon, Oxygen, Iron, and nuclei synthesized in stars, are mainly primaries. Nuclei such as Lithium, Beryllium, and Boron (which are not abundant end-products of stellar nucleosynthesis) or sub-Iron group (poorly produced in the last phases of the stellar burning) are typically of secondary origin. Primary nuclei abundances are representative of the sources composition, revealing details about the nucleosynthesis processes in stars, in supernova or in the Big Bang. Secondary elements abundances can be used to estimate the traversed material (in the leaky-box models) or the diffusion parameters in the Galaxy (in the diffusion models).

In figure 1.3 the relative abundance of different elements as observed in the solar system and in the CR are presented, together with the GALPROP model predictions. Considering the solar system as representative of a typical CR source, the observed over-abundances of CR cosmic nuclides can be explained as a secondary production contribution.

Li-Be-B, sub-Iron ($22 \leq Z \leq 25$) and nuclei with odd atomic number exhibit an excess. While odd atomic number nuclei are weakly bounded and can be destroyed in the stellar thermonuclear reactions, even nuclides are much more stable and then more abundant. Even Z nuclei spallation can contribute to a secondary fraction of the odd nuclei abundance.

Unstable CRs isotopes (a list of them is presented in table 1.1) can be used as *cosmic clocks*. Their abundances relative to those of stable elements undergoing the same processes can reveal the time scale of the different phases in the CRs life, as the delay between production and acceleration (primary K-decay CRs) or the time of confinement in the Galaxy (secondary β-decay CRs).

1.3.1 Primary: Source Composition

Elements with a negligible secondary component are a sample of the CRs at origin. These elements have a chemical composition quite similar to the solar system. This is particularly true when the comparison is restricted to refractory nuclides (Mg, Al, Si, Ca, Fe, Co and Ni) which appear to have undergone minimal elemental fractionation. This is due to the preference of acceleration of dust grains, a chemical composition of refractory elements, respect to volatile elements in interstellar gas [22]. These abundances are in a very good agreement with the solar system values [23], indicating in the stellar flares the origin of most of all CRs species before acceleration. Bearing in mind that the solar system has condensed 4.6 Gyr ago, while CRs are much younger, the close similarity can be used to constrain models of Galactic chemical evolution.

A puzzling exception to this similarity between solar and CRs abundances is the ratio ^{22}Ne/^{20}Ne. The ^{22}Ne/^{20}Ne abundance ratio measured in CR is nearly five time larger than that observed in the solar system. This result cannot be interpreted as due to spallation of heavier elements [24], thus must be related to the peculiar characteristics of their primary source. An enrichment of Wolf-Rayet stars material in the pool of matter from which cosmic rays are accelerated is the most widely accepted mechanism to explain such an excess, indicating *super-bubbles* as astrophysical sites contributing to CR production. The ratios of ^{58}Fe/^{56}Fe and ^{26}Mg/^{24}Mg are also under investigation in order to provide a confirmation.

Nuclide	**Decay Mode**	**Half-life**
^{7}Be	K-capture	53 days
^{10}Be	β-	1.5 Myr
^{14}C	β-	5730 yr
^{26}Al	β+	0.87 Myr
	K-capture	4.0 Myr
^{36}Cl	β-	0.30 Myr
^{37}Ar	K-capture	35 days
^{41}Ca	K-capture	0.10 Myr
^{44}Ti	K-capture	49 yr
^{49}V	K-capture	330 days
^{51}Cr	K-capture	28 days
^{53}Mn	K-capture	3.7 Myr
^{54}Mn	K-capture	312 days
	β+	400 Myr
	β-	0.8 Myr b
^{55}Fe	K-capture	2.7 yr
^{56}Ni	K-capture	6.1 days
	β+	$\sim$ 1 yr
^{57}Co	K-capture	270 days
^{59}Ni	K-capture	76000 yr

Table 1.1: Decay channels for the most interesting unstable and quasi-stable isotopes in GCRs. This elements are astronomic clocks of the cosmic radiation, and their relative abundance, respect to products and progenitors, can estimate the time scale of the different comic-rays life phases.

1.3.2 Primary: Acceleration Delay Clocks

If supernova are at the same time the production and the acceleration place for cosmic rays the time between production and acceleration has to be relatively short. Conversely, if stellar or ISM material has to be injected into the accelerator sites the time has to be longer. The scale time for the acceleration delay can be evaluated with unstable primary isotopes. In supernova explosions, nucleosynthesis of elements above Iron occurs and ^{59}Ni is produced. ^{59}Ni is an unstable primary decaying due to K-electron capture with a half-life of 76 Kyr. This decay is effectively prohibited when ^{59}Ni nuclei are accelerated and stripped of all their atomic electrons. Experimental data [25] indicate that decay of ^{59}Ni in ^{59}Co occurred, leading to the conclusion that a time longer than the ^{59}Ni lifetime elapsed before nuclei were accelerated.

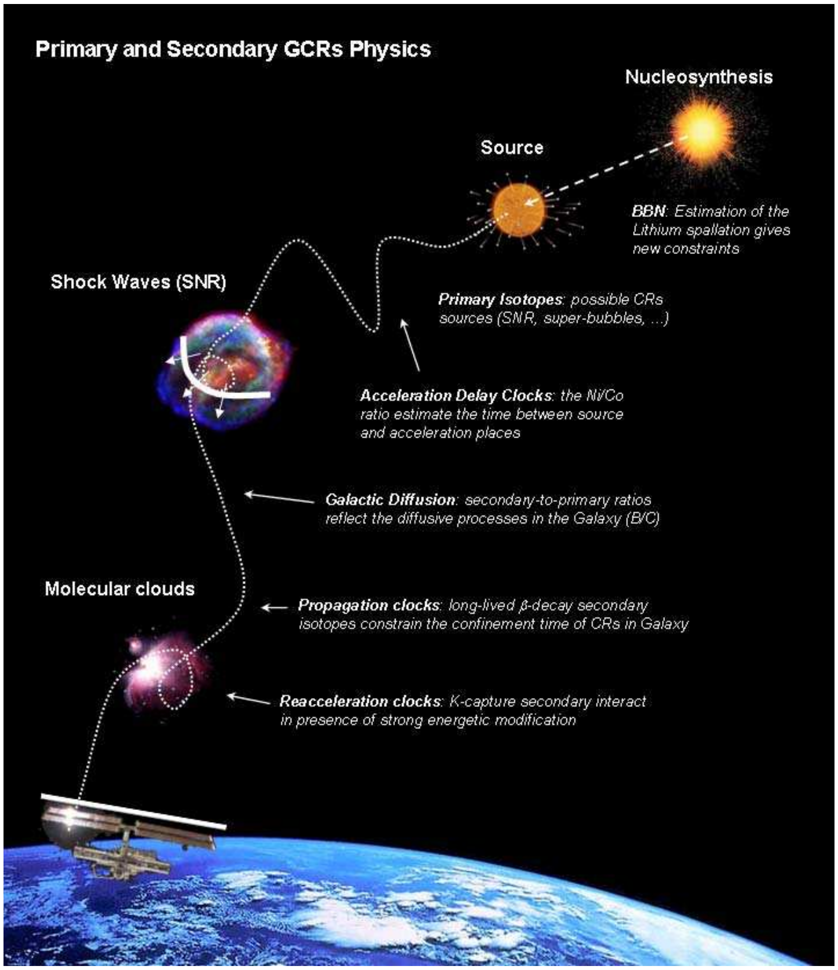

Figure 1.4: A schematic view of the GCRs physics. Primary nuclei reveal details about the CRs origin while secondary nuclei estimate the diffusion parameters of the Galaxy. Unstable isotopes act as cosmic clocks evaluating the time scale of the different phases of the CRs life.

Such long delays would favor models where the cosmic-ray seed population consists of old-stellar, or inter-stellar material, or supernova ejecta not mixing with interstellar matter for at least ~ 100 Kyr before acceleration occurs.

1.3.3 Secondary: Nucleosynthesis Test

The primordial nucleosynthesis, taking place at the very early stages of the universe evolution, is believed to be responsible for the formation of Deuterium, the Helium isotopes ^{3}He and ^{4}He, and the Lithium isotopes ^{6}Li and

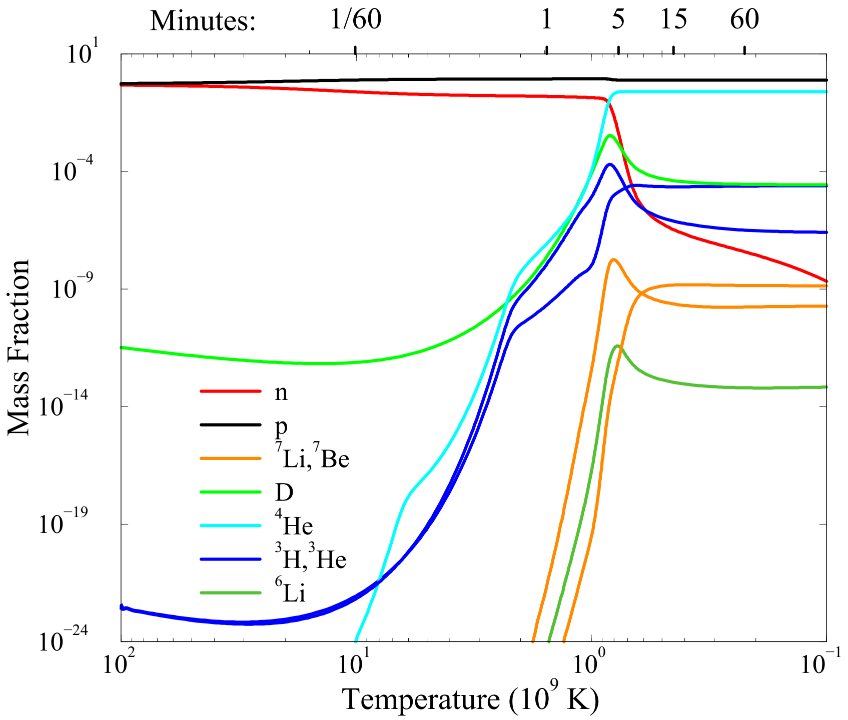

Figure 1.5: Big Bang Nucleosynthesis chemical evolution. The chemical composition of the light elements of the Universe was completely determined within the first 20 minutes after the Big Bang singularity. After that, the temperature and density of the universe fell below the nuclear fusion threshold. While the Helium isotopes abundances are nowadays the same, the much less produced Lithium isotopes are strongly changed due to CRs spallation and stellar nucleosynthesis [16]

.

^{7}Li (figure 1.5).

Chemical and isotopic primordial abundances, as described in the Big Bang Nucleosynthesis model, are in very good agreement with observation of abundances of young astrophysical object (objects with a poor abundance of stellar synthesis elements as CNO). Lithium abundance is an exception: the measured abundance is ~ 2 times larger than the predicted primordial one. This can be related to the fact that Lithium is one of the most fragile isotopes: it can be both synthesized and consumed by stars nuclear fusion processes, as well as produced by cosmic ray spallation. More accurate experimental measurements of the ^{6}Li/^{7}Li ratio (left of figure 1.7) in CRs are needed

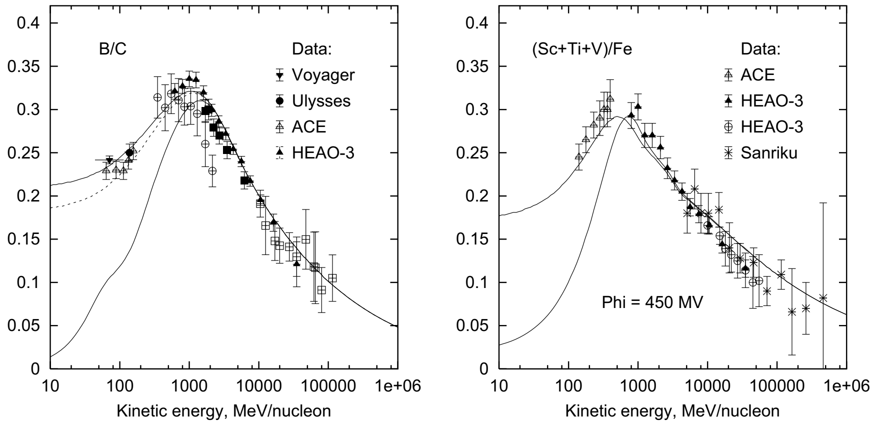

Figure 1.6: Boron-to-Carbon and sub-Iron-to-Iron ratios. The peak at energies around 1 GeV/n can be interpreted in terms of diffusive reacceleration. Different GALPROP models are superimposed [20].

in order to validate or discard the hypotheses put forward to explain the measured excess [26].

1.3.4 Secondary: Galactic Diffusion Coefficient

Secondary stable elements as Deuterium, ^{3}He, Li-Be-B group and the sub-Fe group (Sc, Ti and V), are almost entirely originated in the spallation of primary Hydrogen, ^{4}He, CNO and Iron respectively. Their abundances depend on the original primary composition and on the all-species galactic CRs propagation mechanism.

In the context of the diffusion models [3], the secondary-to-primary ratios, as Boron-to-Carbon and sub-Iron-to-Iron, can be used to constrain the diffusive coefficient of CRs in the Galaxy. An increase of the diffusion coefficient would corresponds to faster escaping of primary nuclei from the Galaxy and would result into a smaller amount of produced secondaries, and vice-versa. The peak structure observed in these ratios (left of figure 1.6) is explained as a diffusive reacceleration of CRs due to the scattering of charged particles on the magnetic turbulence in the interstellar plasma. More accurate measurements of the B/C ratio over an extended energy range could help in solving degeneracy of free parameters in different propagation models [27].

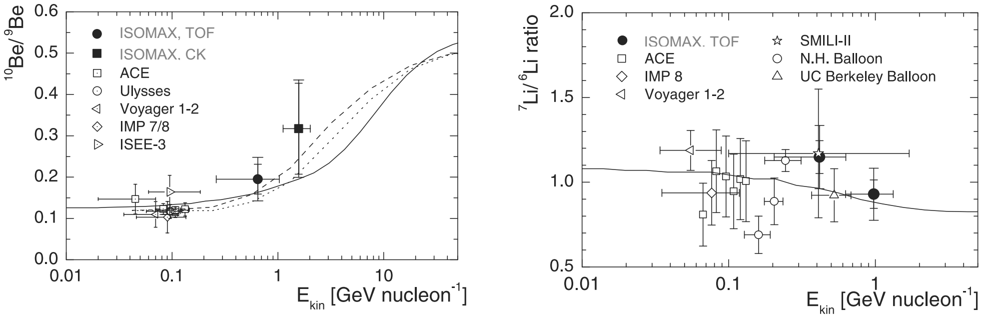

Figure 1.7: Left: Full review of experimental measurements of the ^{10}Be/^{9}Be abundances ratio. Right: Full review of experimental measurements of the ^{7}Li/^{6}Li ratio, that can constraint some properties of the chemical evolution of the universe [28].

1.3.5 Secondary: Propagation Clocks

The confinement time of CRs in the Galaxy is evaluated with *propagation clocks*, i.e. long-lived unstable secondary isotopes. Isotopes as ^{10}Be, ^{14}C, ^{26}Al, ^{36}Cl, ^{54}Mn, are exclusively produced by spallation of heavier elements and subsequently undergo to β-decay, having long lifetimes (table 1.1) extended by the relativistic time-dilation.

In particular Beryllium isotopes, ^{9}Be and ^{10}Be, have a complete secondary origin. While ^{9}Be is stable, ^{10}Be has an half-life of 1.5 Myr. Their production cross section are very similar, however the observed ^{10}Be/^{9}Be abundance ratio is significantly below the unity (right of figure 1.7). This indicates that most of Beryllium has decayed in propagation, setting a lower limit to confinement time of cosmic rays to 15 Myr [7].

1.3.6 Secondary: Reacceleration Clocks

Isotopes that decay only by K-electron capture, ^{37}Ar, ^{44}Ti, ^{49}V, ^{51}Cr, ^{55}Fe and ^{57}Co, although have very short life-times (table 1.1), are effectively stable because at galactic CRs propagation energies their probability to attach an electron is very low. However, if a deceleration occurs and the kinetic energy of ambient electrons is comparable to the binding energy of the K-shell electrons, the electron attachment is allowed and the isotope decays. An excess of their decay products with respect to the unstable parents abundances could indicate a deceleration phase and a subsequent reacceleration of CRs during propagation. Current experimental data do not yet permit a clear conclusion on this subject [29].

1.4 Measurement of GCRNs

The CR flux decreases of about 30 orders of magnitude from the MeV region to the 10^{20}eV (figure 1.1): different experimental approaches are then needed to measure CR energy spectra and composition at different energies.

Direct measurements of CRs, before their interaction with the atmosphere, are carried out by compact detectors on board of high altitude balloons or spacecrafts. The strict requirements on weight and power consumption for flying equipment constraint the size, and therefore the acceptance, of such experiments which are limited by the collectable statistics at energies of TeV/n.

At very low energies (<GeV) the flux is intense enough to allow even relatively small detectors, with acceptances of O(100) cm^2sr, to directly measure chemical composition and isotopic abundances of GCR with good statistical accuracy. The High Energy Telescope (HET) on Ulysses spacecraft [19] or the Cosmic Ray Isotope Spectrometer (CRIS) on board of the Advanced Composition Explorer (ACE) satellite [30], have performed accurate measurements of chemical and isotopic composition of GCRN using the full absorbtion technique in solid state compact detectors.

In the GeV–TeV energy domain, much larger exposures are required in order to reach the statistical sensitivity for direct measurements of light ($Z = 1, 2$) and heavier ($Z > 2$) CR energy spectra and composition. Light nuclei energy spectra and isotopic composition studies in this energy range have been performed by means of magnetic spectrometers on board of stratospheric balloons as the Balloon-Borne Experiment with a Superconducting Spectrometer (BESS) [31][32], the Cosmic Anti-Particle Ring Imaging Cherenkov Experiment (CAPRICE) [33], the Matter Antimatter Superconducting Spectrometer (MASS) [34] and the Alpha Magnetic Spectrometer AMS-01 [35] flown on the shuttle *Discovery*. A clear advantage of the magnetic spectrometric technique is the simultaneous measurement of the absolute value and the sign of the charge, allowing the study of anti-matter CR components. The drawback of such spectrometric approach is the intrinsic limits of its geometrical acceptance, typically < 1 m^2sr). In fact, large bending power BL^2 is needed to extend the spectrometric measurement to high rigidities. For a given effective area of the tracking device, an increase in the length L over which the bent track is measured directly translates on a limit on the tracker angular acceptance, whose typical values are $\sim 40°$. For what concerns the B intensity, either light-weight magnet are used to generate intense B field in a reduced volume (hence reducing the geometrical acceptance) or much heavier equipment is needed (at the expenses of a critical mass budget for the whole instrument).

At higher energies, up to 10^{14} eV, the extreme rigidity of the CR tracks and the need of large exposure factors effectively prohibit the use of magnetic spectrometers and satellite experiments. Detection techniques based either on calorimetry, as the Advanced Thin Ionization Calorimeter (ATIC) [36], or on transition radiation emission as the Transition Radiation Array for Cosmic Energetic Radiation (TRACER) [37] or on both techniques as in the Cosmic-Ray Energetics and Mass (CREAM) experiment [38] are used.

At higher energies, only ground based experiments can actually reach the required exposures for CR detection: the properties of energetic CRs are inferred from the characteristics of Energetic Air Showers (EAS) produced in their interactions with the atmosphere. Large arrays of detectors disposed on areas up to 3000 km^2 are used to reconstruct the shower shape and composition, measuring either the charged shower components as KASKADE [9] or the emitted radiation accompanying the shower as HiRes [14], or AGASA [13] or both as the Pierre Auger Observatory (PAO) [39]. Monte Carlo techniques are then used to extract the original CR identity and energy from the differences in the expected interactions with the atmosphere.

EAS observatories in space, based on the detection of UV light accompanying the shower as in the Extreme Universe Space Observatory (EUSO) [40] or as in JEM-EUSO [41], as well as the PAO upgrade with a Northern Site of $\sim$ 10.000 km^2 [42] of existing ground based installation are being proposed to extend experimental measurements at energies above the GZK limit.

In the following, we will briefly review direct measurements on GCR nuclei with $Z > 2$, referring to [43] for more general reviews on the subject.

1.5 Direct Measurement of GCRs Nuclei

Starting in the sixties, the GCR chemical composition has been extensively studied in balloon-borne experiments (see table 1.2), even if the most precise absolute flux measurements have been obtained by two space-borne experiments: C2 on the High Energy Astrophysics Observatory 3 (HEAO-3) [52] and Cosmic Rays Nuclei (CRN) instrument on-board of the Spacelab-2 mission [53]. C2 was able to discriminate among nuclei from Beryllium up to Nickel in the energy 0.6–35 GeV/n. This high statistics measurement was extended by CRN up to TeV/n energy for the most abundant elements (measurement presented in figure 1.9).

The present generation of experiments measuring the chemical composi-

GRCs Chemical Composition Measurement	**Date**	**Experimental Method**	**Carrier**	**Elements**	**Energy (GeV/n)**	Exposure (m^2·sr·h)
Juliusson et al. [44]	1971	Cherenkov Counters	Balloon	$3 \leq Z \leq 28$	20–120	7.6
Orth et al. [45]	1972	Magnetic Spectrometer	Balloon	$3 \leq Z \leq 26$	2–150	1.15
Maehl et al. [46]	1973	Cherenkov Counters	Balloon	$5 \leq Z \leq 26$	0.32–2.20	2.4
Caldwell et al. [47]	1974	Cherenkov Counters	Balloon	$5 \leq Z \leq 28$	5–90	4.5
Lezniak et al. [48]	1974	Cherenkov Counters	Balloon	$3 \leq Z \leq 28$	0.3–50	23.
Simon et al. [49]	1976	Ionization Calorimeter	Balloon	$5 \leq Z \leq 26$	2–100	15.5
Dwyer et al. [50]	1978	Cherenkov and MWPC	Balloon	$5 \leq Z \leq 28$	1–10	38.
JACEE [51]	1979–1995	Emulsions Calorimeter	Balloon/LDB	$1 \leq Z \leq 26$	1000–10^6	1432.
C2 on HEAO-3 [52]	1979–1980	Cherenkov Counters	Satellite	$4 \leq Z \leq 28$	0.6–35	430.
CRN on Spacelab-2 [53]	1985	TRD and Cherenkov Count.	Shuttle	$6 \leq Z \leq 27$	50–1500	70.
Buckley et al. [54]	1991	Ring Imaging Cherenkov	Balloon	$2 \leq Z \leq 8$	40–320	1.4
RUNJOB [55]	1995–1997	Emulsions Calorimeter	Balloon	$1 \leq Z \leq 26$	10^4–10^6	1000.
TIGER [56]	1997	Cherenkov Counters	LDB	$26 \leq Z \leq 40$	0.8–5	—
TRACER [37]	1999	TRD and Proportional Tube	LDB	$16 \leq Z \leq 26$	10–$2 \cdot 10^5$	100.
ATIC [36]	2002	Si Matrix and Calorimeter	ULDB	$1 \leq Z \leq 26$	100–10^5	300.
GRCs Isotopic Composition Measurement						
EIS on IMP-7 & 8 [17]	1973–1978	Solid State Detector	Satellite	$2 \leq Z \leq 26$	0.01–0.100	
CRISIS [57]	1977	Cherenkov and Emulsion	Balloon	$10 \leq Z \leq 28$	0.4–0.9	
HET on Voyager 1 & 2 [58]	1977–now	Solid-State Detector	Spacecraft	$1 \leq Z \leq 28$	0.001–0.500	
HIST on ISEE-3 [59]	1978	Solid State Detector	Satellite	$2 \leq Z \leq 10$	0.005–0.030	
HET on Ulysses [19]	1990–now	Solid-State Detector	Spacecraft	$4 \leq Z \leq 28$	~ 0.185	
CRIS on ACE [30]	1997–now	Solid-State Detector	Satellite	$2 \leq Z \leq 30$	0.05–0.5	
ISOMAX [28]	1998	Magnetic Spectrometer	Balloon	$3 \leq Z \leq 8$	0.2–2	

Table 1.2: Summary table of the principal experiments devoted to chemical and isotopic GCR composition measurements. Experiments performing only chemical composition measurements are reported in the first part of the table. A schematic plot summarizing table is in figure 1.8.

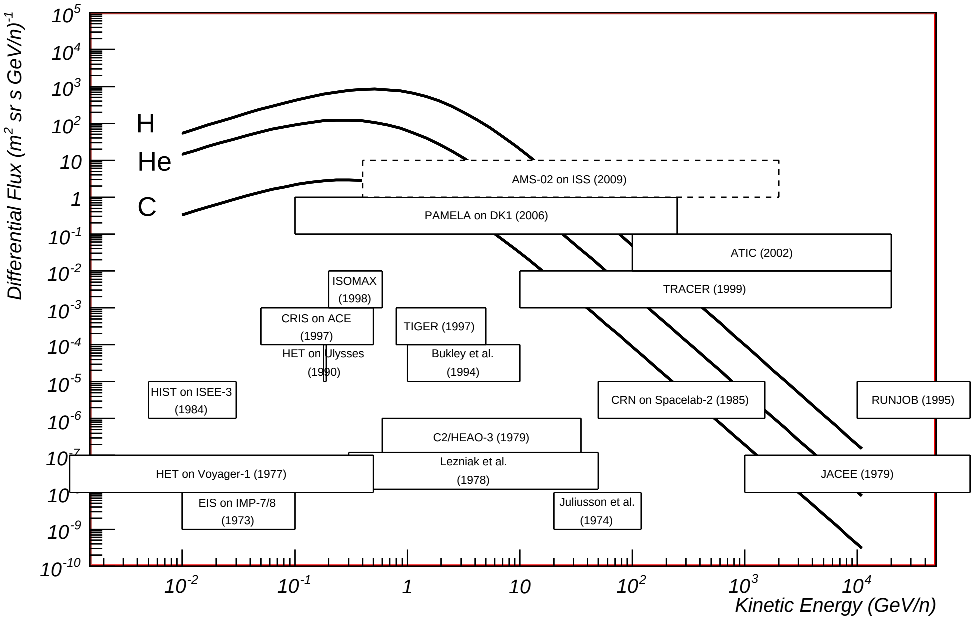

Figure 1.8: The principal experiments devoted to chemical and isotopic composition. (a) on the left spatial-borne experiments of reduced dimension, narrow energy range with an high accuracy isotopic distinction are placed; (b) on the right balloon-borne experiments with wide acceptances devoted to the chemical composition studies toward knee are positioned; (c) the spatial spectrometry, placed on the upper part, conjugate the wide energetic spectra and the high accuracy isotopic distinction.

tion is devoted to reveal the composition toward the knee energies following the road opened by the JACEE collaboration [51]. Instruments as TRACER [37], ATIC [36] and CREAM [38], are designed to provide differential flux measurements of different GCRN species at energies between GeV/n and 10^2 TeV/n. All these new instruments are profiting of an increased ballooning time (up 42 days in the record 2004 flight of the CREAM experiment) provided by the NASA Ultra-Long Duration Balloon program on Antarctica.

The isotopic composition, instead, has been mostly matter of space experiments as the series of High Energy Telescopes (HET) flying with the Voyager 1, Voyager 2 [58] and Ulysses [60] spacecrafts, or the Cosmic Rays Isotope Spectrometer (CRIS) instrument on the Advanced Composition Explorer (ACE) satellite [30]. All these instruments are characterized by solid-state

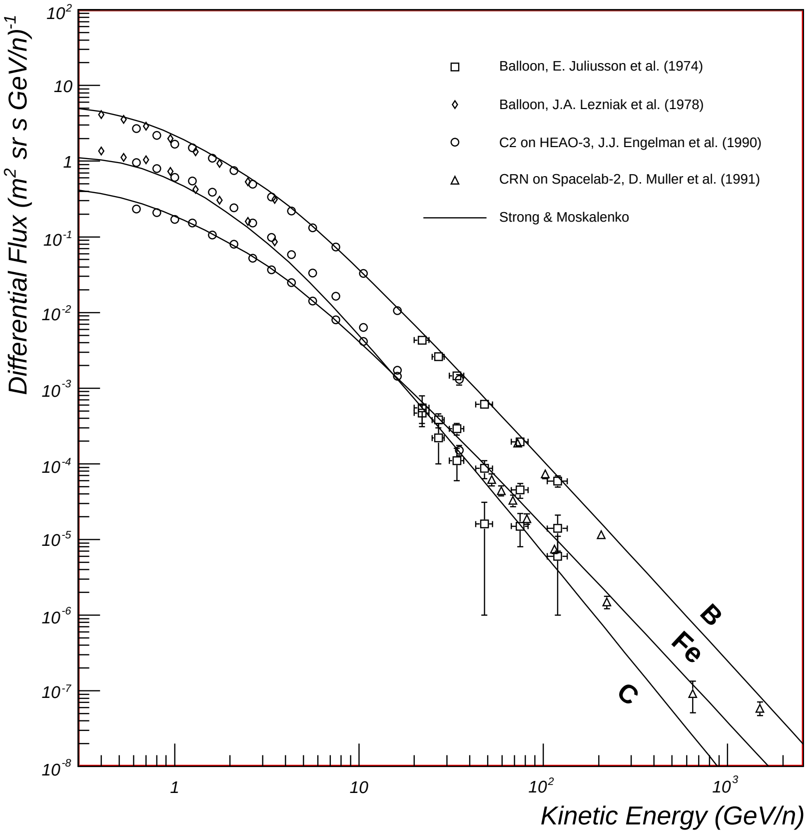

Figure 1.9: Points: experimental measurements of Carbon, Boron and Iron energy spectra. Lines: expected fluxes from the GALPROP 2007 model.

Silicon detectors able to distinguish a wide number of isotopes (almost all the species in cosmic rays up to Iron) in a narrow energetic range around $\sim$ 100 MeV/n. An exception to this picture is the magnetic spectrometer ISOMAX, flown in 1998, which extended the ^{10}Be/^{9}Be ratio measurement up to 2GeV/n.

1.5.1 Chemical Composition and Spectrum

A wide experimental program devoted to direct measurements of CRs chemical compositions in complementary energy ranges was initiated in the early '70s with a series of balloon-borne and satellite based experiments.

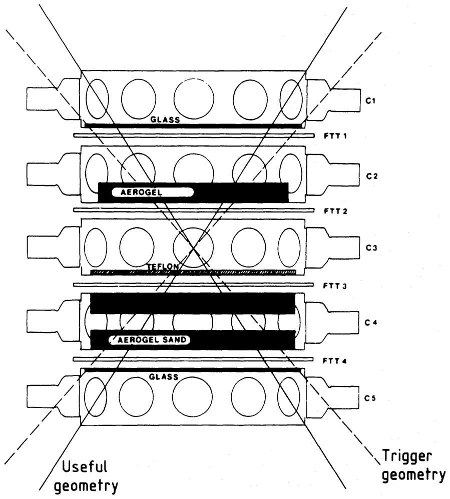

Figure 1.10: The C2 on HEAO-3 experiment is a typical multi-Cherenkov experiment. Scintillator layers, used for trigger, are separated by the 5 Cherenkov counters. Three different radiators are used in order to extend the energy range of the measurement [52].

Low accessible energies (10–100 MeV/n) and isotope identification capabilities were the key features of solid state instruments developed for the Interplanetary Monitoring Platform (IMP) satellite series [17]. These series of successful satellite measurements were extended at lower energies (5–30 MeV/n) through the series of the three International Sun-Earth Explorer (ISEE) until 1997.

CR Chemical composition up to Nickel was studied by balloon borne instruments, mostly based on Cherenkov detection technique; these experiments were sensitive to energies ranging from few hundred MeV up to $\sim$ 100 GeV.

In spite of this large experimental effort, only in the 1980s the chemical composition has been measured with an high statistics by two space-borne experiments: the French-Danish C2, an ensemble of Cherenkov counters aboard on the NASA High Energy Astrophysics Observatory 3 (HEAO-3) satellite [52] and the University of Chicago Cosmic Rays Nuclei (CRN), an instrument based on a transition radiation detector on-board of the Shuttle *Challenger* in the mission Spacelab-2 [53].

The C2 experiment on board of the HEAO-3 satellite was based on multiple Cherenkov counters detectors: a schematic view of the instrument is reported in figure 1.10. It consisted of five layers of Cherenkov counters interleaved with four planes of scintillator layers used for trigger. The Cherenkov radiation is emitted when a charged particle passes through an insulator at a speed greater than the speed of light in that medium. For a radiator material with refractive index n, the counter threshold corresponds to a minimum particle velocity $\beta > 1/n$, approximately equivalent to a threshold of $K_n > n/\sqrt{\beta^2 - 1}$ in kinetic energy per nucleon. Over threshold, and in a narrow energy range, simultaneous measurements of β and charge can be efficiently performed with a single Cherenkov counter thanks to the dependence of the photon production on the square of the absolute particle charge, as described by the Frank-Tamm relation:

$$\frac{dN^2}{dx d\lambda} = \frac{2\pi\alpha Z^2}{\lambda^2} \cdot \left(1 - \frac{1}{\beta^2 n^2}\right)$$

λ being the emitted photons wavelength. However, in an extended energy range, photon production of high energy Z-particles ($\beta \rightarrow 1$) and low energy $(Z+1)$-particles ($\beta \rightarrow 1/n$) can be easily confused.

Three different radiator materials (glass, aerogel and teflon) were therefore used in C2 order to obtain charge discrimination in an extended energy range, 0.6–35 GeV [52].

Calorimetric techniques based on emulsion stacks were used by the Japanese-American Collaborative Emulsion Experiment (JACEE) [51] flown yearly from 1979 to 1995 and the subsequent RUssian Nippon JOint Balloon experiment (RUNJOB) [55].

A typical JACEE emulsion module is shown in right picture in figure 1.12. Multiple layers of emulsion plates, interleaved with lead foils, are stacked. The pattern in Emulsion/Lead plates arrangement is optimized in order to have a clean measurement of ionization loss, i.e. Z charge of incident particles, in the topmost emulsion layers while favoring nuclear interactions in the central part of the apparatus.

In left plot of figure 1.12 results from JACEE and RUNJOB experiments on GCRN fluxes are presented: uncertainties in the energy calibration and statistical fluctuations do not allow to draw definite conclusions on the spectral indexes of heavy nuclear components from these measurements.

Modern calorimetric techniques are used by ATIC [36] and CREAM [38] instruments.

A quite different and interesting experimental approach is used in CRN [53] and the recent TRACER [37] experiment, flown in 1999, 2003 and 2006

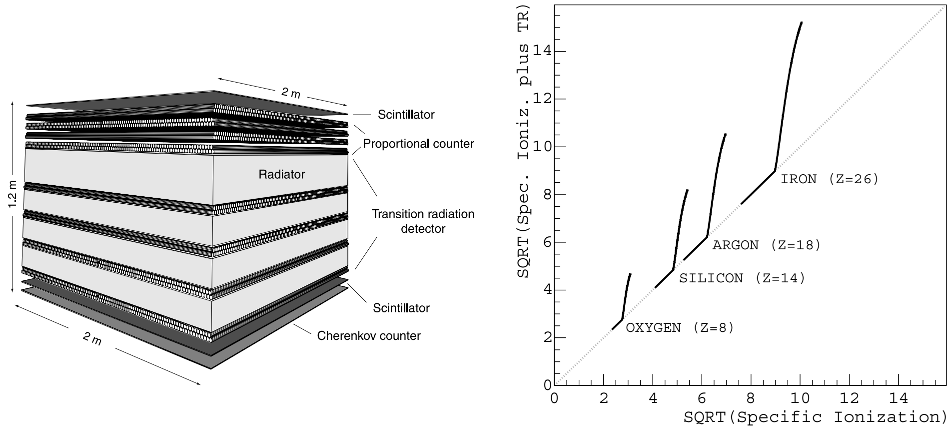

Figure 1.11: The TRACER instrument is based on the experience developed with the CRN experiment. A TRD core is surrounded by proportional tubes, a Cherenkov counter and scintillators as presented on the left picture. The energy deposition by ionization, measured by the tubes on the top of the instrument, versus the energy measured in the TRD tubes, sum of the energy loss by ionization and the transition radiation produced in the radiator, gives a characteristic pattern different for each chemical species, as presented in the right plot. The resulting charge separation is very clean [37].

on long duration balloon flights [61]. In these experiment the measurement at high energy is based on the transition radiation detection.

Transition Radiation (TR) is emitted by charged particles when crossing the boundary between two media with different dielectric constants. The probability of photon emission is negligible for values of the Lorentz boost factor $\gamma < 1000$, while above this threshold is nearly constant, depending only on the particle absolute charge $\sim 0.5\% \times Z^2$. The low production rate at the single boundary crossing is overcome by stack of radiator foils, i.e. multiple vacuum-matter interfaces, interleaved with proportional tubes. Being sensitive to the γ of incident particles, TRD detectors are typically used to discriminate between relativistic electrons and protons (or pions) up to several hundred GeV. In TRACER the Z^2 dependence of emission process is exploited for nuclei charge-discrimination at high energy ($>$ TeV). While the similar Lorentz factor characterizes nuclei with the same kinetic energy per nucleon ($\gamma = K/m$), the number of emitted photons varies significantly in different species.

In TRACER layers of scintillators (for the trigger), Cherenkov counters

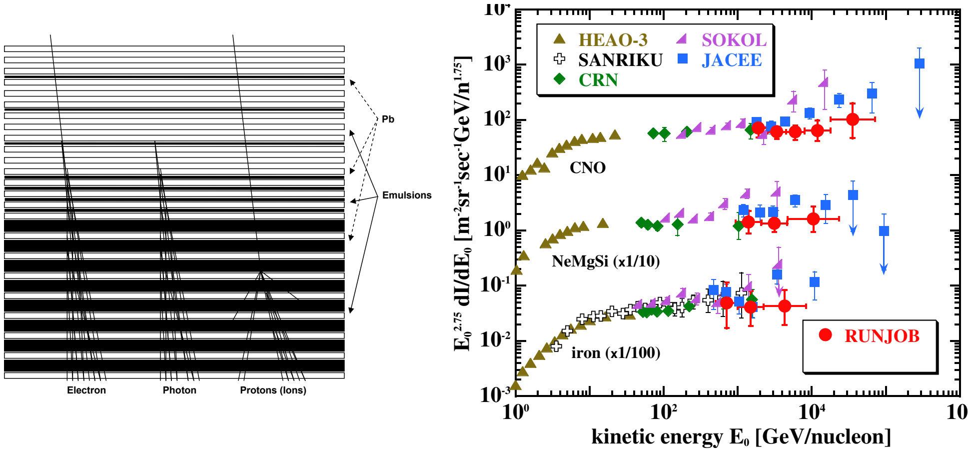

Figure 1.12: Left: the JACEE emulsion module. Layers of emulsion plates, measuring the hadronic shower development, are interleaved with lead foils maximizing the probability of inelastic collision. Right: The heavy component spectra measurements from RUNJOB, JACEE and other experiments [55].

and proportional tube arrays surround a central TR detector (TRD) core. The TRD is composed by radiator fibers and single-wire proportional tubes for the X-ray detection (the apparatus is presented on the left of figure 1.11). At low energies separation between different chemical species is achieved using the energy loss by ionization in the proportional tubes on the top of the instrument, or by the signal in the Cherenkov counter. At high energies, the signal released in the TRD tubes is the sum of the ionization signal and the transition radiation photons. The comparison between the ionization energy loss in the proportional tubes outside and inside the TRD results in a very clean pattern characteristic of each single chemical species (right of figure 1.11).

In figure 1.13 the first TRACER results of the differential flux measurement for different CR nuclides are reported together with a collection of previous experiments results.

1.5.2 Isotopic Composition and Isotopic Ratios

As of today, CRs isotopic composition measurements have been mainly performed by a few space instruments, with similar characteristics, launched in the eighties on board of NASA missions. Among these experiments, the Cosmic Ray Isotope Spectrometer (CRIS) has collected the largest statistics and

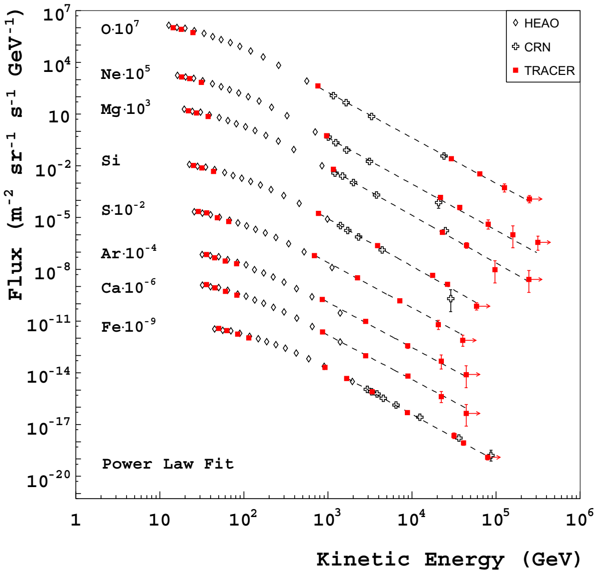

Figure 1.13: Differential energy spectra for GCRNs as measured by the TRACER, HEAO and CRN experiments [62].

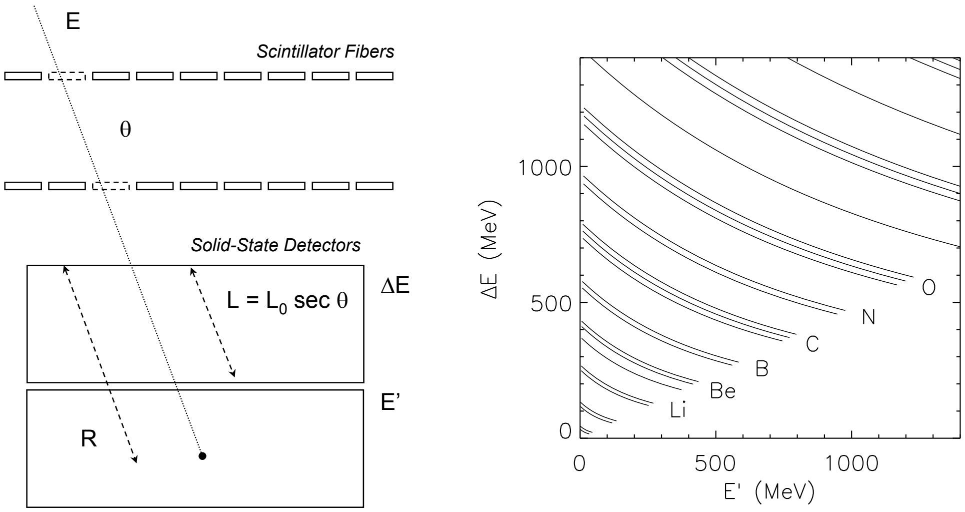

Figure 1.14: The CRIS/ACE schematic setup. The scintillator fibers system provides for trigger and for the precise measurement of the particle angle θ. Using the measured ΔE and the residual energy E in the solid-state detectors chain a complete isotopic distinction is feasible.

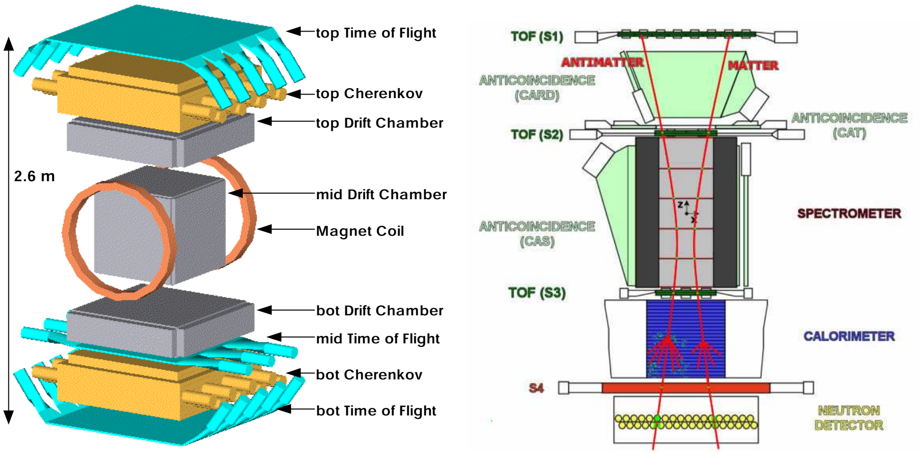

Figure 1.15: Schematic view of the ISOMAX balloon-borne magnetic spectrometry instrument (on the right) and of PAMELA, a space-borne magnetic spectrometer (on the left).

provided the most impressive results. Its experimental approach is similar to the high energy telescopes carried on the Voyager and Ulysses missions or on the ISEE-3 satellite (see table 1.2).

A schematic view of the experimental setup and of the measurement principle are presented in figure 1.14. Two layers of scintillator fibers are used to determine the trajectory of the particle impinging on a first layer of Lithium-doped Silicon, where an energy loss $\Delta E \propto Z^2$ is released due to ionization. Particle is then stopped in a second Silicon-Lithium layer, releasing its residual energy E'. Using the empirical relation between range R in silicon and energy deposition [30]:

$$R(E, Z, M) \simeq k \frac{M}{Z^2} \left(\frac{E}{M} \right)^a \qquad a \simeq 1.7$$

is possible to reconstruct energy E, charge Z and mass M of the impinging particle. Since particles are assumed to be absorbed in the detector, their energy cannot exceed the O(100)MeV/n. These detectors perform a very precise isotopic distinction, with a good statistical accuracy thanks to the long satellite lifetimes, but in a very narrow energy interval.

The Isotope Magnet Experiment (ISOMAX) [28] experiment, a superconducting balloon borne magnet spectrometer has provided the only measurements of isotopic composition for $3 \leq Z \leq 8$ elements in the GeV/n energy region. The ISOMAX detector was designed to achieve a mass resolution better than 0.25 amu by using a rigidity versus velocity technique. A schematic view of the instrument is presented in figure 1.15. Three detector subsystems can be identified: the magnetic spectrometer using a drift chamber tracker, a time of flight system providing the trigger, charge and velocity measurements up to ~ 1 GeV/n, two silica-aerogel Cherenkov counters, providing independent measurement of β at higher kinetic energy (~ 2 GeV/n). The mass of the impinging particle could be reconstructed from the relation:

$$m(\beta, Z, R) = RZe\frac{\sqrt{1-\beta^2}}{\beta c}$$

where R is the particle rigidity. ISOMAX primary goal was to measure the ^{10}Be/^{9}Be ratio up to $E = 4$ GeV/n in a program of multiple balloon flights. Unfortunately, during the second flight in 2000, the scientific program was definitely stopped by a sudden rupture of the pressure vessel and the total loss of the instrument due to a catastrophic landing.

1.5.3 Perspectives of GCRN Measurements

As presented beforehand, a new generation of balloon-borne experiments is presently devoted to the measurement of GCRs spectra for single chemical species up to *knee* energies. These experiments have typically larger acceptances O(m^{2}sr) with respect to space-borne experiments, overcoming the limited ballooning exposure time with multiple long duration missions. In the next few years results from these experiments will greatly increase our knowledge of GCRN composition and energy spectra. However, all these measurements will suffer of common systematic uncertainty coming from the atmospheric corrections needed in order to extract Top of the Atmosphere (TOA) fluxes from the measured ones at few g/cm^2 of residual atmosphere. The quite delicate issue of energy calibration over extended energy ranges can lead to *hidden* experimental errors which could partially spoil the expected measurement accuracies.

A new generation of magnetic spectrometers, PAMELA on board of the Russian satellite DK1 [63] and AMS-02 on the International Space Station, will provide long duration measurements of CR fluxes from space, allowing the simultaneous measurements of nuclear, electron and anti-matter components in the GeV–TeV energy range.

The PAMELA spectrometer was launched in June 2006 with the RESURS DK1 satellite along an elliptical orbit at an altitude ranging between 350–610 Km with an inclination of 70.0 °. A schematic view of the instrument is presented on the right of figure 1.15. The spectrometric core has a geometrical acceptance of ~ 20.5 cm^{2}sr. Tracking is performed with high resolution double sided microstrip silicon sensors, with an expected Maximum Detectable

Rigidity (MDR) of 1.2 TV. A sampling imaging calorimeter, in which pairs of orthogonal ministrip silicon sensor planes are interleaved with tungsten absorber, and a neutron monitor, composed by ^{3}He counters and polyethylene neutron moderators, are used to distinguish primary protons and electrons. A Time-of-Flight system, using plastic scintillation detectors, measures the charge of the incident particles, the versus of their flight and the velocity of low energy particles, to determine, combined with the rigidity, the mass. Nuclear charge separation up to Oxygen is achieved by means of energy loss measurement in the Tracker and Calorimeter silicon sensors, while isotope separation will be possible for light nuclei (H, He) up to $\sim$ 1 GeV. The PAMELA will reach in three years an exposure of $\sim$ 50 m^{2} sr h, insuring $3 < Z < 8$ nuclear spectra accurate measurement up to $\sim$ 200 GeV/n.

The AMS-02 detector, whose characteristics will be discussed in detail in the following chapters, has been conceived for a three-years mission in space. With an exposure factor of $\sim 25 \cdot 10^{3}$ m$^{2}\cdot$sr$\cdot$h, a MDR of 3 TeV and a nuclear charge separation up to Iron, it will provide the most precise measurement of nuclear energy spectra up to the TeV/n energy. Moreover, thanks to an extreme accuracy in the β measurement, it will be able to extend the ^{10}Be/^{9}Be measurement up to 10 GeV/n, thus providing an unique experimental constraint on confinement times of CR in the galaxy.

Chapter 2

The Alpha Magnetic Spectrometer

The Alpha Magnetic Spectrometer (AMS) is a large acceptance (0.45 m^2sr) cosmic rays detector which will be installed on the International Space Station (ISS) in 2009 for an operation time of three years.

AMS has been designed and built taking advantages from the experience of the high energy particle physics experiments. It is made of a superconducting magnet generating a field of about ~ 0.8T within a cylindrical shaped volume (diameter and height $\simeq 1$ m). In the magnet bore eight planes of Silicon detectors measure the coordinate of the points used to reconstruct the tracks. The magnetic spectrometer as a whole is able to measure rigidities from fractions of GVs to few TVs.

At both ends of the magnet a couple of segmented scintillator planes is placed. They measure the Time of Flight (ToF) of the particle and provide the trigger of the experiment. An anti-coincidence scintillator system (ACC) provides the veto signal in the trigger for the high inclined particles. The AMS-02 detector is completed by other three sub-detectors which provide the particle identification: a Ring Image Cherenkov (RICH) below the magnet for the measurement of the particle velocity; the Transition Radiation Detector (TRD) placed on top and an Electromagnetic Calorimeter (ECAL) at the bottom for the accurate distinction between leptons and hadrons.

The main goal of the AMS experiment is to search for antimatter of primordial origin looking for the presence of anti-nuclei into the cosmic rays flux. The detection of a never seen presence of anti-nuclei in GCRs, as a nucleus of $\overline{\mathrm{He}}$, can be a direct proof of the existence of antimatter domains, since the probability of a spallation production of $\overline{\mathrm{He}}$ is very low [64].

Another interesting discover potential for AMS concerns the indirect dark matter detection. Thanks to the large acceptance, the long exposure time and the excellent particle identification capabilities AMS can measure the spectra of the CR rare components ($\overline{p}$, e^+, $\overline{D}$, γ) with a great accuracy over a never explored energy range. Deformation in those spectra could arise from the annihilation of the particles composing the dark matter (for example the neutralino χ_0). In particular the positron channel is very promising as suggested by the AMS-01 experiment [65].

The high statistic AMS-02 measurements of all the charged species of the cosmic rays, including chemical species up to Iron and isotopes up to Carbon, will largely improve our knowledge of the cosmic rays and will help to solve several astrophysics fundamental questions (see chapter 1).

The AMS-02 detector has also a γ-rays astronomy capabilities. The γ are detectable in two ways: by measurement of a couple of tracks produced in a pair conversion ($\gamma \rightarrow e^+ + e^-$) in the material before the Tracker, or by an electromagnetic shower initiated in the electromagnetic calorimeter (in this case ECAL is used as a stand-alone detector) [66]. A star tracker gives the orientation of the detector with respect to the fixed stars with an accuracy of few arc seconds.

In this chapter the sub-detectors of the AMS-02 detector are briefly reviewed with particular emphasis to the Silicon Tracker. Techniques for the ion fluxes measurement are then discussed and, at the end, the expected AMS-02 results in terms of collected statistics and attended fluxes are presented.

2.1 AMS-02 Apparatus

Requirements for a space-borne high energy physics experiment are extremely challenging. Several constraints are imposed by the transport on the Space Shuttle, by the transfer and the permanence on the ISS, as the strict weight limit of 7 tons, the very low power consumption ($\leq$2 kW) and the data rate limited to 2 Mbits per second. In addiction the AMS-02 experiment must work properly in space without any external operation for more than three years, has to survive accelerations up to 9 G and vibrations up to 150 dB during shuttle launch, and withstand temperature cyclic variations between $-80°$C and $50°$C in vacuum. Each sub-system and electronic component is produced in prototypes (engineering, qualification and flight models) tested in order to provide the expected physic performance and the mandatory Space safety [67].

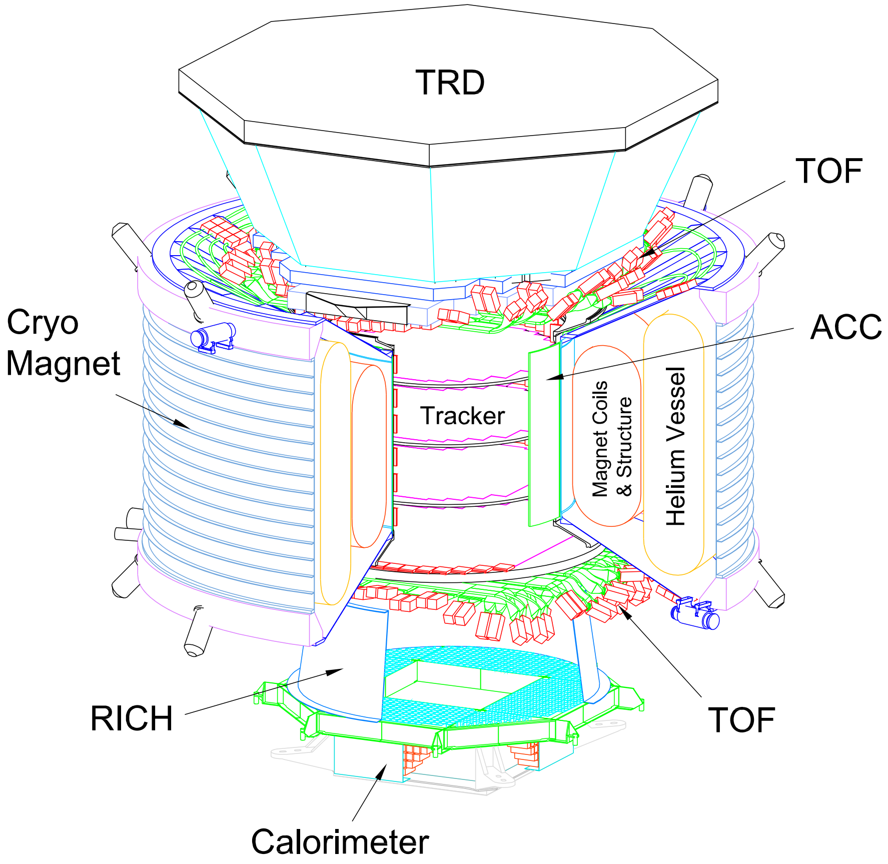

Figure 2.1: An AMS-02 detector schematic view.

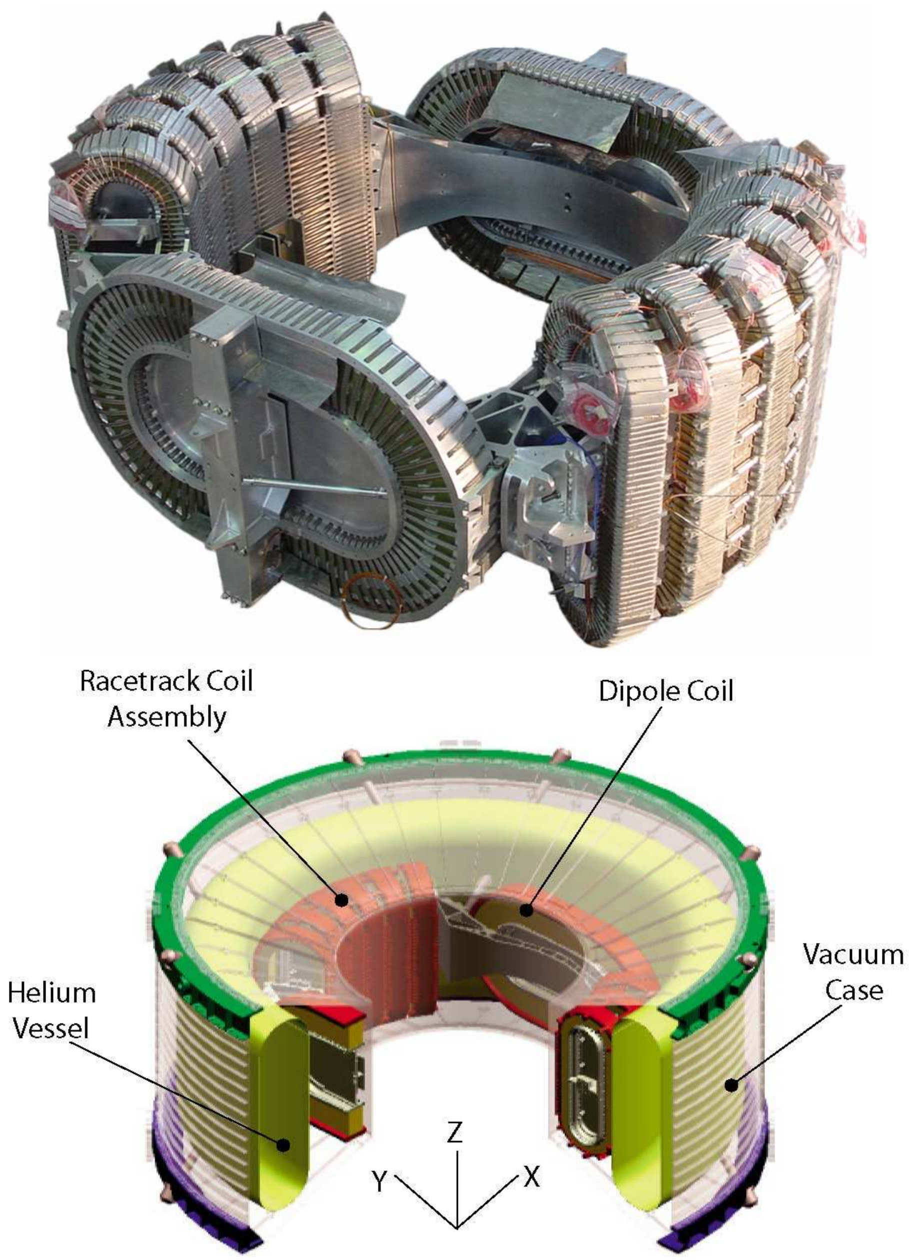

Figure 2.2: The AMS-02 magnet is composed by 14 superconducting coils developing a dipolar magnetic field of $\simeq 0.87$ T in the center. The magnetic field is developed along the direction of the two biggest coils and defines the AMS x-axis (upper picture). The system is cooled by a cryogenic system composed by a toroidal vessel of 2500 l of superfluid Helium at the temperature of 1.8 K. The magnet, the Helium vessel, and the components of the cryogenic system are all situated inside a vacuum tank as sketched on the lower scheme.

2.1.1 Cryogenic Magnet

The superconducting magnet system for AMS-02 consists of a pair of large dipole coils together with two series of six smaller racetrack coils circumferentially distributed between them (upper photo of figure 2.2). The dipole coils are used to generate the majority of the transverse magnetic field which defines the AMS x-axes. In the center a magnetic field of about 0.87 T can be obtained. The racetrack coils are included for minimizing the magnitude of the stray field outside the magnet and to minimize the magnetic dipole moment of the magnet system to avoid an undesirable torque on the ISS resulting from the interaction with the Earth magnetic field (0.27 Nm).

The magnet operates at a temperature of 1.8 K, cooled by a surrounding toroidal vessel of 2500 l of superfluid Helium. The cryogenic magnet will be launched at the operating temperature, while the field will be charged only after installation on the ISS. Because of parasitic heat loads, the Helium will gradually boil away throughout the lifetime of the experiment. After the project time of 3 years, the Helium will be used up and the magnet will warm up and no longer be operable [68].

A complex cryogenic system is been developed in order to preserve the cryogenic temperature and to maximize the life of the superfluid Helium. The basic components are:

- a Passive Phase Separator (PPS) separate the heated gaseous Helium from the superfluid (in zero-gravity there is no separation between the liquid and gas);
- a Cooling system composed by 4 concentric shields encloses magnet and Helium vessel. The Helium vapor is guided in these shield reducing dramatically the heat leak of the superfluid;
- 4 Cryocoolers are added in order to reduce significantly heat at higher temperature;
- a Mass Gauging system evaluate the mass of the helium fluid measuring the temperature variation occurring after a small heat pulse;
- 2 Thermo-mechanical cooling pumps are added for cooling down the cryogenic system in the case of a quenching, and in case of charging and discharging of the whole apparatus.

The magnet, the Helium vessel and the cryogenic system are all enclosed in a toroidal vacuum tank with inner diameter of 1.1 m, outer diameter of 2.7 m and a length of the central cylinder surrounding the tracker of 0.9 m (all the cryogenic system is sketched on the lower plot of figure 2.2).

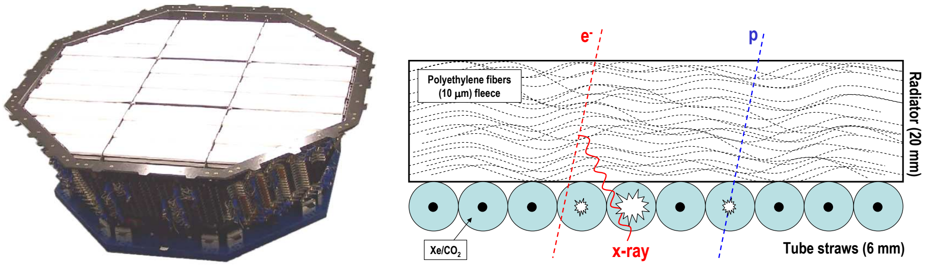

Figure 2.3: Left: a picture of the truncated octagonal pyramid AMS-02 TRD. Right: the principle of measurement, the TR X-rays ($\sim$ 10 keV) produced by electron in the fleece are efficiently absorbed in the straw tubes, producing a signal significantly larger with respect a $\mathrm{MIP}_{\mathrm{gas}} \sim$ keV. [69].

2.1.2 Transition Radiation Detector (TRD)

In the AMS-02 TRD the transition radiation is used to discriminate between electrons, emitting TR X-rays, and protons up to 300 GeV [70].

The AMS-02 TRD, placed on top of the magnet vacuum case (figure 2.1), is made by 328 modules. The modules are arranged in 20 layers supported by a conical octagon made of aluminum-honeycomb walls with carbon-fiber skins and bulkheads. To provide a 3D tracking, the lower and upper four layers are oriented parallel to the AMS-02 magnetic field while the middle 12 layers run perpendicular.
Each modules contains:

- 20 mm of radiator made of polypropylene/polyethylene fiber fleece corresponding to 0.06 g/cm^3. The large number of interfaces increases the probability of production of X-rays.
- 16 tube straws filled with a Xe:CO$_2$ (80%:20%) gas mixture operating at 1600 V (full avalanche regime). The Xenon-rich gasses have an high efficiency for X-rays detection.

A 20 layer prototype built with final design components was tested on lepton/hadron beam test. Figure 2.4 presents the signal collected in the straw tubes for pions, protons, muons and electrons. The larger tail observed in the electron distribution is populated by the transition radiation X-ray.

Using both a likelihood selection and a neural network algorithm to combine the 20 measurements, it is possible to obtain a proton/electon rejection ranging 100–2000 for protons to 250 GeV and with a 90% electron efficiency [70].

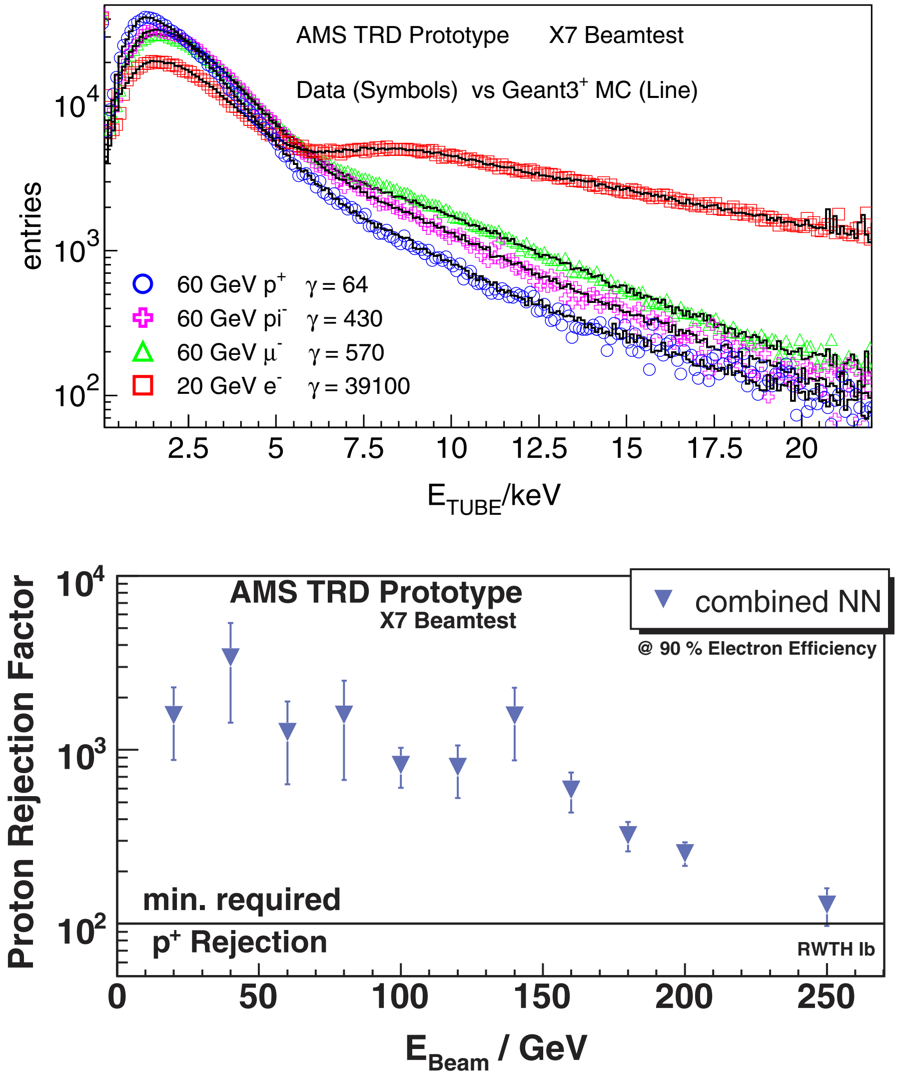

Figure 2.4: Beam test results for the TRD prototype. In the upper plot measured data for p, π^-, μ and e are compared with a GEANT4 simulation. In the lower plot is presented the obtained proton rejection with the request of 90% electron efficiency with a Neural Network based probability test [70].

Figure 2.5: The completed upper and lower ToF before the final shielding. The scintillator paddles, the bent light guides and the PMT are exposed.

2.1.3 Time-of-Flight System (ToF)

Charged particle ionization in a scintillating medium causes molecular exitation/disexcitation processes with the fast emission ($\tau \sim 10^{-8}$s) of fluorescence light. The photon collection provide a very precise timing measurements and an estimation of the particle energy deposit. Scintillation counters placed at both ends of a particle detection experiment measure the time of flight of the traversing particle, i.e. the particle velocity, and provide the trigger for other detectors.

The AMS-02 ToF system is composed by 4 planes of scintillation counters 2 above and 2 below the magnet (figures 2.1 and 2.5). The four planes contain, beginning from top, 8, 8, 10 and 8 scintillator paddles. The upper ToF and the lower ToF planes are alternatively positioned along the x and y coordinates providing a granularity of 12×12 cm^2 cells. The ToF single counter consists of 1 cm thick polyvinyltoluene scintillator of trapezoidal (18.5–26.9×117–134 cm^2) or rectangular (12×117–134 cm^2) shape, at both ends coupled, via plexiglass light guides, to 4 (rectangular) or 6 (trapezoidal) photo-multipliers (PMTs). A particular class of PMTs, the *fine mesh*, with a compact dynodes structure and high voltage ($\simeq 1600$ V) has been selected

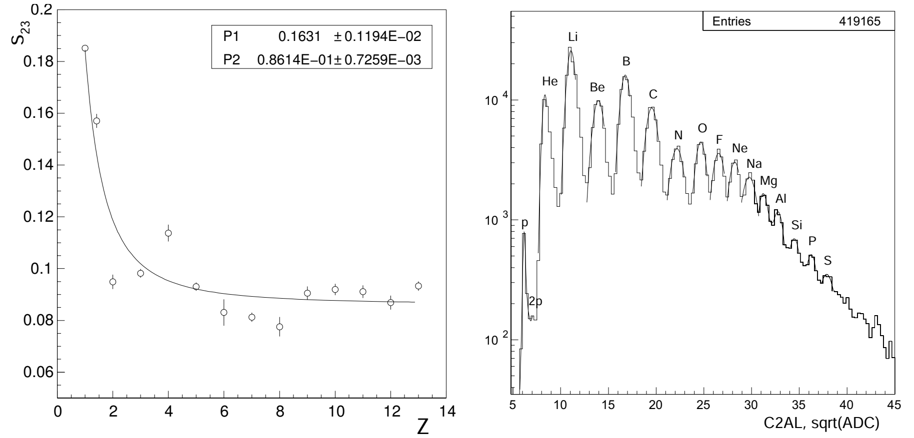

Figure 2.6: Measured ToF performances in the 2003 ion beam test. On the left the time-of-flight resolution function of the particle charge. The distribution is fitted with the expected behavior $\sqrt{P_0 + 1/P_1}$. A time-of-flight resolution of 160 ps is achieved for protons, while a resolution of 100 ps is measured for $Z \geq 2$. In the right plot the charge distinction resulted by a low gain counter is presented, gaussian fits on the charge peaks are superimposed [72].

in order to reduce the dependence of the photo-induced multiplication by the stray magnetic field (of about ~ 2 kG). Tilted and bent light guides have been used to optimized the angle between PMT along the y-axis and the magnetic field (figure 2.5) [71].

The performances of the ToF scintillation counters were tested in a ion beam test in 2003 [72]. The measured timing resolution on the time-of-flight is $\simeq 160$ ps for protons and $\simeq 100$ ps for particles with $Z \geq 2$ (left plot of figure 2.6). The resulting resolution on velocity β is $\sigma_\beta/\beta \simeq 3\%$ for protons and $\sigma_\beta/\beta \simeq 1\%$ for ions.

The measured time-of-flight resolution gives a distinction power between up-going and down-going nuclei $\gtrsim 10^9$. This performance is a mandatory requirement for the anti-matter detection.

The energy deposition in a single ToF counter gives also an evaluation of the particle charge exploiting the relation between the energy loss by ionization ($\propto Z^2$) and the produced scintillation light. Figure 2.6 presents the charge discrimination for only one low gain counter tested on a ion beam test. In AMS the ToF will provide 4 independent charge measurements.

The ToF system provides the charged particles fast trigger signal for the whole apparatus.

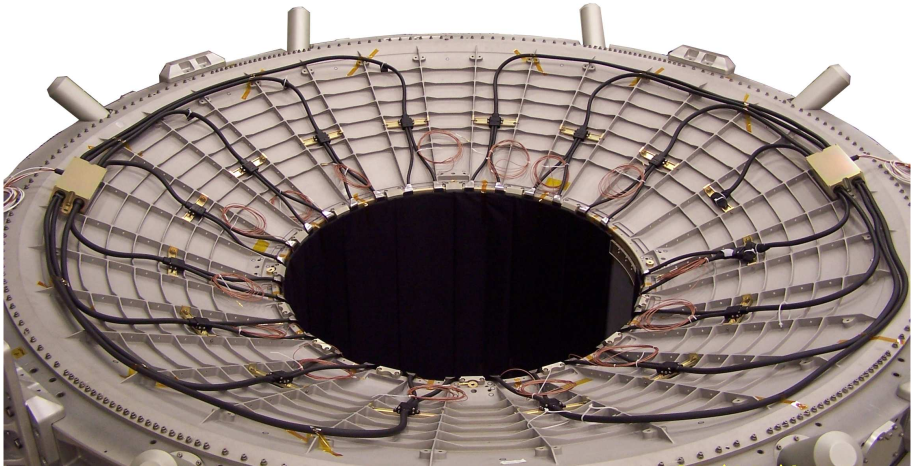

Figure 2.7: The ACC system mounted inside the vacuum tank. The signals from the 16 scintillation paddles, arranged on the inner cylinder of the vacuum case, are guided and coupled by wavelength shifter fibers to 8 PMTs on the border of the toroidal structure. A similar fiber/PMTs readout scheme is repeated on the other side of the vacuum case in order to provide redundancy of the veto system.

2.1.4 Anti-Coincidence Counter (ACC)

The Anti-Coincidence Counter (ACC) is composed by 16 paddles arranged on a cylinder surrounding the Tracker (figure 2.1). The light coming from the scintillation panels is collected in wavelength shifter fibers of 1 mm diameter, embedded in grooves milled into the scintillation panels. At both ends of the counters, the fibers are routed in 2 bunches of 37 fibers each to transition connectors located on the conical flanges of the magnet vacuum case. From these connectors the light is routed through clear fibers up to the 8 PMTs mounted on the rim of the vacuum case. The ACC PMTs, similar to the ToF ones, are placed approximately 40 cm from the racetrack coils and are oriented with their axes parallel to the stray field.

The very high efficiency and a high degree of homogeneity of the scintillating fibers will ensure a reliable and fast ACC veto trigger signal for the high inclination particles with also some impact point determination capabilities [73].

2.1.5 Silicon Tracker

When a ionizing particle crosses a silicon detector electron/hole pairs ($\sim 10^4$) are produced. Charges are rapidly drifted ($\tau \sim$10 ns) by the sensor electric field, generated by the inverse bias regime, toward the segmented electrode strips. The obtained signal is proportional to the energy deposit and identifies the coordinate of the traversing particle (details about the Silicon sensors are given in chapter 3).

The AMS-02 Silicon Tracker is composed by 8 layers of Silicon double-sided sensors disposed on 5 planes, two inside and three outside the magnet. Each planes located inside (outside) have a composite structure with two 220 (700) µm thick layers of Carbon fiber surrounding a 12 (40) mm thick, low density Aluminum honeycomb interior of density $\rho = 16.02$ (32.0) kg/m^3. The diameter of the interior (exterior) planes is 1.0 (1.4) m (upper photos of figure 2.8). A Carbon fiber cylindrical shell, supporting planes 2 to 4 located inside the magnet, and two Carbon fiber flanges, supporting the exterior planes 1 and 5 provide an high precision Silicon sensor positioning and the mandatory structure resistance for vibrations due to the Shuttle launch (lower photo of figure 2.8).

Each one of the 8 layer has a diameter of $\sim$ 1 m and contains approximately 24 *ladders*. Each ladder is composed by a variable number of double-sided silicon sensors (from 7 to 15) grouped along the x direction and coupled to a read out chain characterized by a low power consumption ($\sim$ 0.7 mW per channel), a low noise and a large dynamic range.

The basic Tracker element, the double-sided Silicon sensor, has dimensions of $\sim 72.045 \times 41.360 \times 0.300$ mm^3. Biasing of n-type high resistivity 300 µ thick Si sensors is made with a dynamic resistive coupling, as punch-through and surface-through techniques. On the two surfaces p^+ strips with an implantation (readout) pitch of 27.5 (110) μm and n^+ strips, along the orthogonal direction, with implantation (readout) pitch of 104 (208) μm are placed. The finer pitch p-side strips is used to measure the bending, or y, coordinate while the orthogonal n-side strips measure x (for details see chapter 3).

A global sensitive active area of 6.6 m^2, for 2264 Silicon sensors arranged on 192 ladders, makes the Silicon Tracker the largest precision position detector in space.

In order to keep the event size at a manageable level, an early suppression of the $\sim$ 196k Tracker readout channels with no significant signal is performed in the online processing of the Tracker data by dedicated Tracker Data Reduction (TDR) boards.

The Tracker system is completed by two sub-system: the Tracker Ther-

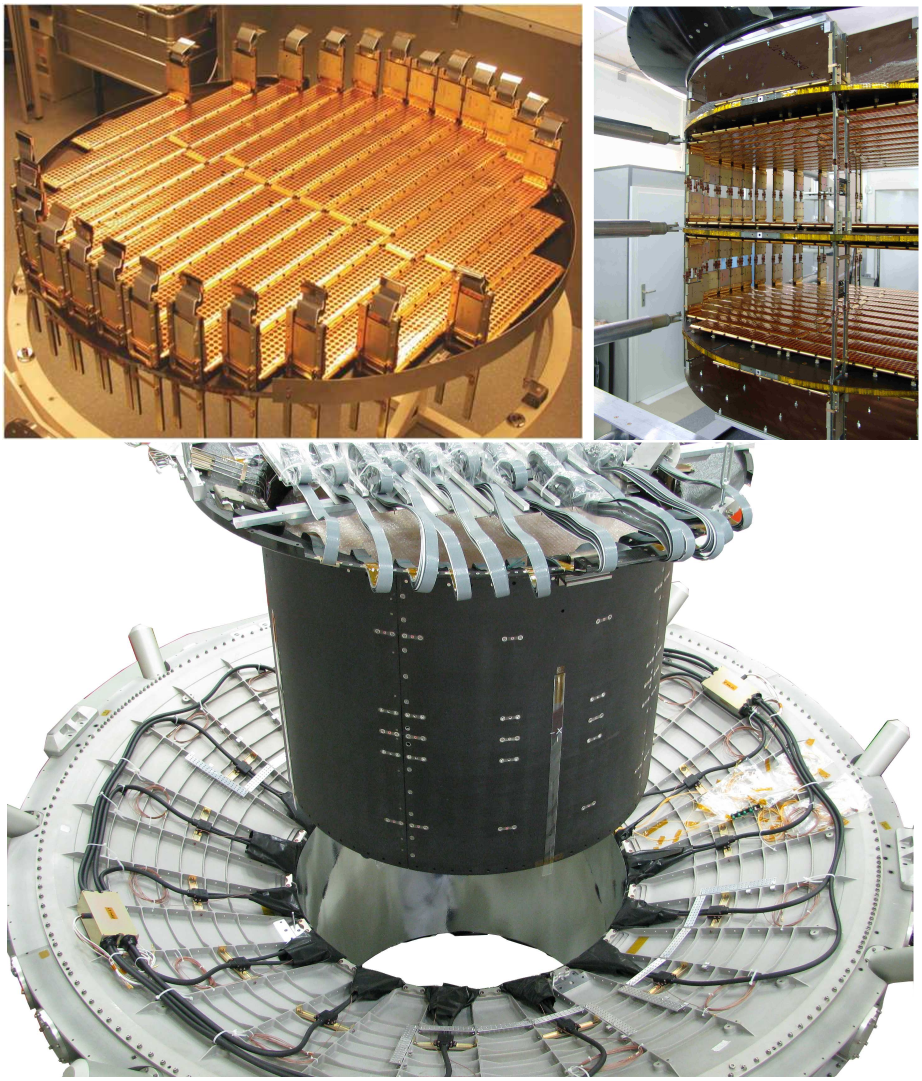

Figure 2.8: Some of the steps of the Tracker integration. Top left: an assembled layer. Top right: the assembling of the inner Tracker layers, note the 6 layers arranged on 3 supporting planes. Bottom: the pre-integration of the Silicon Tracker in the AMS vacuum case.

mal Control System (TTCS), a two phases (liquid, gas) CO_2 heat exchanging system that chills the Tracker electronics minimizing the heat conduction toward the cryogenic magnet; and the Tracker laser Alignment System (TAS) providing optically generated signals in the 8 layers that mimic straight (infinite rigidity) tracks allowing the tracing of changes of the tracker geometry with a position accuracy of better than 5 µm.

The Silicon Tracker performances in terms of calibration stability, spatial resolution and charge discrimination have been studied with several beam using electron, photon, protons and ions beam lines. The measured spatial resolution of 10.7 (6.5) µm for protons (Helium) for the bending coordinate gives a Maximum Detectable Rigidity (MDR) of few TV [1].

The characterization of the Silicon signal in presence of ions is developed in chapter 4.

2.1.6 Ring Imaging Detector (RICH)

The Cherenkov radiation cone is emitted by a charged particle with velocity larger than the phase velocity of the electromagnetic field in the material. The properties of the cone depend on the velocity of the charged particle and on the refractive index of the material. The measurement of the opening angle of the Cherenkov cone by the detection of the Cherenkov ring in the imaging detectors evaluate the particle velocity and, the estimation of the number of detected photons, provide an independent measurement of the incoming particle charge.

The AMS-02 Ring Imaging Cherenkov detector (RICH) consists of a radiator plane, a conical mirror and a photon detection plane. The radiator is composed by a dodecahedral polygon with a 118.5 cm internal tangent diameter. It consists of an array of 2.7 cm thick aerogel tiles with a refractive index between 1.03–1.05, which surrounds a central 35×35 cm^2 region equipped with 5 mm thick sodium fluoride (NaF) radiator ($n_{NaF} = 1.335$). This radiators combination optimizes the overall counter acceptance (0.4 m^{2}sr) since the Cherenkov photons radiated by the NaF in large cones will fall within the detection area. In fact the detector plane has an empty 64×64 cm^2 area in its center, matching the active area of the electromagnetic calorimeter located below. Outside the “ECAL hole”, 680 4×4-multi-anode PMTs (gain 10^6 at 800 V) are arranged to cover the circular 134 cm diameter surface at the basis of the conical mirror. The radiator and the detection plane are enclosed in the volume of a conical reflector multi-layer structure on a Carbon fiber reinforced composite substrate of height 47 cm. The mirror increases the RICH acceptance reflecting high inclination photons and provide the necessary photon drift ring expansion (figure 2.10).

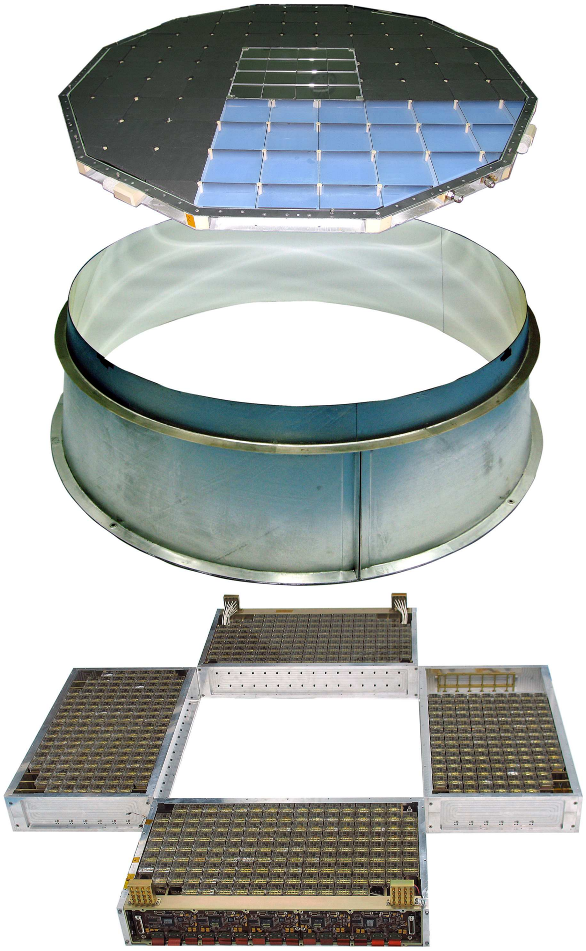

Figure 2.9: Exploded view of the RICH detector. It is composed by three parts: the radiators layer, the conical mirror and t he detection plane (the angular sectors of the detection plane are not shown).

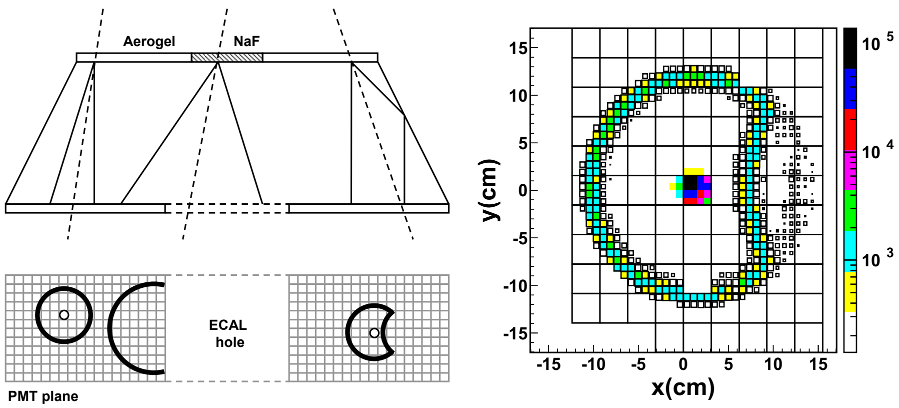

Figure 2.10: Left: The overall RICH acceptance is increased by (a) a conical mirror is used in order to collect high inclination photons, (b) the use of a larger refractive index radiator (NaF) in the center of radiator minimizing the loss of efficiency due to the detection plane hole in corresponding to the calorimeter position. Right: Cherenkov ring for a position fixed beam measured in the 2003 test beam [74].

RICH provides the β measurement with a resolution $\sigma_\beta/\beta \sim 0.1\%$, for unitary charge particles, and $\sigma_\beta/\beta \sim 0.01\%$ for ions. It also provides a particle charge measurement with a charge confusion of the order of 10 %. Its performances will be described in detail later in this chapter.

2.1.7 Electromagnetic Calorimeter (ECAL)

The AMS-02 Electromagnetic Calorimeter (ECAL) is a fine grained lead-scintillating fiber sampling calorimeter which allows for precise, 3-dimensional imaging of the longitudinal and lateral shower development. The system provides an high $\sim 10^6$ electron/hadron discrimination, in combination with the TRD, and good energy and angular resolution [75].

The calorimeter consists by a pancake composed from 9 *super-layers* for an active area of 648×648 mm^2 and a thickness of 166.5 mm. Each super-layer is 18.5 mm thick and made of 11 grooved, 1 mm thick lead foils interleaved with layers of 1 mm diameter scintillating fibers, glued together with epoxy resin.

The detector imaging capability is obtained by stacking super-layers with fibers alternatively parallel to the x-axis (4 layers) and y-axis (5 layers) (figure 2.11). The pancake has an average density of 6.9 ± 0.2 g/cm^3 for a total weight of 496 kg.

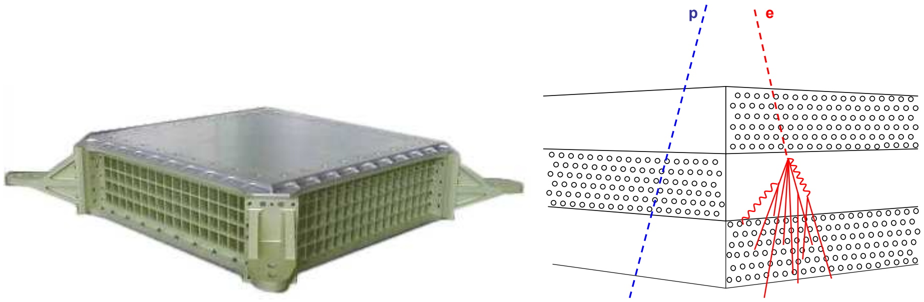

Figure 2.11: Left: the ECAL before the installation of PMTs. Right: the scintillating fibers and lead foils structure of three assembled super-layers are presented to show the principle of the measurement.

Each super-layer is read out by 36 PMTs, arranged alternately on the two opposite ends. Fibers are read out, on one end only, by four anode Hamamatsu PMTs, each anode covers an active area of 9×9 mm^2, corresponding to 35 fibers, defined as a *cell*, the minimum detection unit.

In total the ECAL is subdivided into 1296 cells for 324 PMTs and this allows a sampling of the longitudinal shower profile by 18 independent measurements.

The ECAL thickness corresponds to about 16.7 radiation length, including almost all the electromagnetic shower generated by incident electrons or photons. The sum of the energetic deposit in the super-layers estimates the incident particle generating the shower original energy E. The energetic resolution were evaluated in an electron/proton beam test on a ECAL prototype in 2002 [75]. According to figure 2.12:

$$\frac{\sigma_E}{E} = \frac{(10.2 \pm 0.3)\%}{\sqrt{E(\mathrm{GeV})}} \otimes (2.31 \pm 0.05)\%$$

The longitudinal profile of the shower, in terms of depth in units of radiation length $t = x/X_0$, can be described as a gamma function [76]:

$$\frac{\mathrm{d}E}{\mathrm{d}t} = E_0 \frac{b^{\alpha+1}}{\Gamma(\alpha+1)} t^{\alpha} e^{-bt}$$

with the maximum placed at $t_{max} = X_0 \log E(GeV) + cost$ (figure 2.12). By the 3D reconstruction of the profile an evaluation of the direction of the incident particle can be derived. The measured angular resolution is:

$$\Delta\theta_{68\%} = \frac{(8.0 \pm 0.1)^\circ}{\sqrt{E(\mathrm{GeV})}} \otimes (0.57 \pm 0.04)^\circ$$

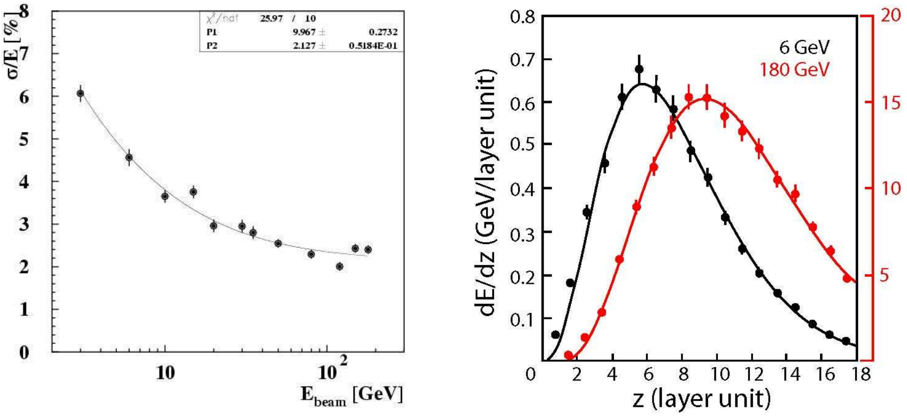

Figure 2.12: Results from the ECAL 2002 beam test are presented. Left: the energy resolution as a function of electron energy. Right: the longitudinal profile for electron induced showers in terms of the layer units ($\sim t$). The X_0 can be derived from the maximum of these distribution [75].

The calorimeter also provides a stand-alone photon trigger capability to AMS. The trigger efficiency is 90% at 2 GeV and more than 99% for energies larger than 10 GeV.

2.2 Ion Reconstruction

A correct estimation of the GCR ions fluxes is based on an accurate measurement of distinct incoming particle properties. They include the absolute charge (identifying chemical species), the momentum, the charge sign (separating matter from anti-matter), and eventually the mass (identifying the isotopic composition).

In AMS-02 the cosmic ion detection is performed by a simultaneous measurement of magnetic rigidity, charge and particle velocity by means of the AMS-02 sub-detectors, the relevant particle properties are then obtained by the combination of these measurements:

- **Chemical composition**: the particle absolute charge is estimated either from the number of photons in the RICH Cherenkov rings ($\propto Z^2$) or from the energy deposition ($\propto Z^2$) in the Tracker Silicon sensors and in the ToF scintillator paddles.

- **Energy spectra**: track reconstruction in the magnetic field provides the rigidity measurement. Momentum is obtained multiplying the rigidity with the measured charge. The energy can then be obtained using the measured mass or assuming an average isotope mixture.

- **Anti-nuclei detection**: the reconstructed track curvature combined with the up-going to down-going particle discrimination from the ToF gives the particle charge sign;

- **Isotopic composition**: the velocity measurement performed by the ToF, and with more accuracy, by the RICH combined with the momentum measurement allow to estimate the particle mass;

In addition a correct evaluation of the trigger efficiency and the estimation of the ions inelastic fragmentation within the AMS materials is fundamental in order to reconstruct the ion absolute fluxes.

A detailed description of the measurement principles and of the expected performance is presented in the following.

2.2.1 Charge Measurement

In AMS-02 the absolute value of the charge is measured independently in each of the 8 layers of the silicon Tracker, in the four scintillator planes of the TOF and with the RICH detector.

In the Tracker the signal measured on the readout channels is proportional to the energy deposited by the particle while crossing the Silicon. This ionization energy is given by the well known Bethe-Block formula [76]:

$$-\frac{\mathrm{d}E}{\mathrm{d}x} = Kz^2\frac{Z}{A}\frac{1}{\beta^2}\left[\frac{1}{2}\ln\frac{2m_ec^2\beta^2\gamma^2T_{\max}}{I^2} - \beta^2 - \frac{\delta(\beta\gamma)}{2}\right]$$

where:

- x is the amount of traversed material in g/cm^2;

- $K \simeq 0.307$ MeV g^{-1} cm^2;

- Z, A and I are characteristics of the traversed material and correspond to the atomic number, the mass number and the mean excitation energy;

- z, β, $T_{\max}$ are the incoming particle charge, speed and maximum energy transferable in a collisions with an electron;

- $\delta(\beta\gamma)/2$, is a *density* effect correction.

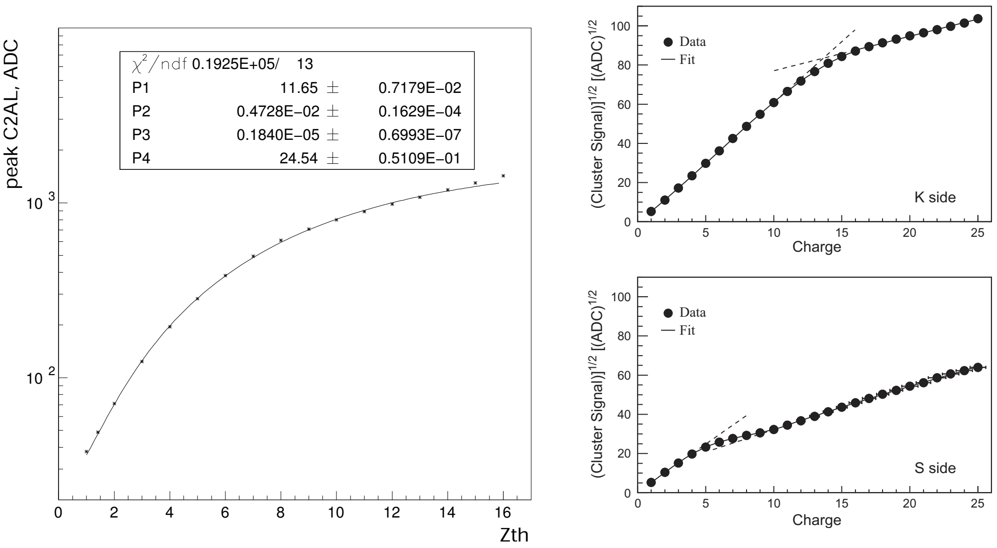

Figure 2.13: The MPV signal measured for different charges measured by ToF (on the left) and Tracker (on the right). The non-linearities are due: (a) non-linear light response (Birks-Chou law) and saturation effect for scintillator system [72]; (b) non-linear charge collection or electronic saturation effects for Tracker [77].

Indicating with H the energy loss for a Minimum Ionizing Particle and applying the usual approximations of the Bethe-Block formula results:

$$-\frac{\mathrm{d}E}{\mathrm{d}x} \approx H\,z^2$$

considering a 300 µm Silicon sensor the average MIP energy loss results $H_{300\mu\mathrm{m,Si}} \simeq 80keV$. The energy deposition in thin materials is distributed as a Landau convoluted with Gaussian, a distribution with an high energy asymmetric tail caused from the sporadic Δ-rays production high energy losses. The Most Probable Value (MPV) of these distributions, as measured for the different charges on a ion test beam, is not strictly proportional to z^2 (figure 2.13) as a consequence of readout electronic effects (saturation, non-linearities). The study of an algorithm for an efficient charge identification with the Tracker is discussed in detail in 4.

The scintillation light produced by particle traversing a plastic scintillator is related to the energy deposited by ionization as described by the Birks-Chou formula [78]:

$$L = \frac{A\mathrm{d}E/\mathrm{d}x}{1 + B\mathrm{d}E/\mathrm{d}x + C(\mathrm{d}E/\mathrm{d}x)^2}$$

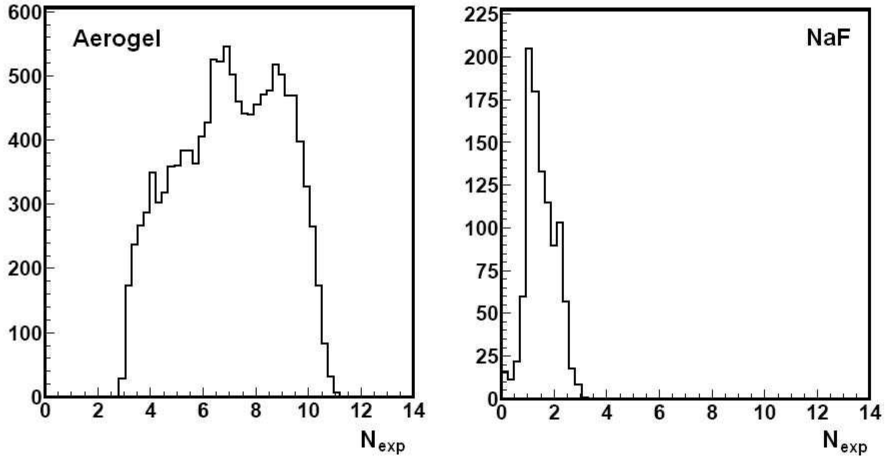

Figure 2.14: The RICH simulated number of expected photons in the Cherenkov rings for charge 1 particles. The structures in the plot are due to the non-linear geometric efficiency [74].

where A, B and C are constant determined experimentally. Typical values for AMS scintillators are: $A \approx 10$, $B \approx 10^{-2}$ and $C \approx 10^{-5}$ (figure2.13 left). Given the small values of B and C the scintillation light is roughly proportional to z^2 and a efficient charge separation can be done also with ToF. However saturation effects and the details of the light transportation in the scintillator introduce a degradation of the charge separation power for $z \geq 10$.

The number of photons emitted in the Cherenkov cone $N_{\text{p.e.}}$ depends on the particle velocity β and on its absolute charge z as described by the Frank-Tamm formula:

$$\frac{\mathrm{d}^2 N}{\mathrm{d}x\mathrm{d}\lambda} = \frac{2\pi\alpha Z^2}{\lambda^2} \cdot \left(1 - \frac{1}{\beta^2 n^2}\right)$$

where λ is the wavelength of the emitted photon, and n is the radiator refraction index.

Indicating with N_{exp} the expected number of photons for $z = 1$ particles, the incoming particle charge is obtained with a simple formula:

$$z = \sqrt{N_{\text{tot}}/N_{\text{exp}}}$$

The value of N_{exp} however depends on many factors as a consequence of the

RICH acceptance inhomogeneities. It is approximately given by:

$$\frac{\mathrm{d}^2 N_{\mathrm{exp}}}{\mathrm{d}x\mathrm{d}\lambda} = 2\pi\alpha\frac{q(\lambda)}{\lambda^2}\sin^2\theta_C(n,\beta)\epsilon(x,\lambda)f(x,\lambda)$$

where λ is the wavelength of the emitted photon, n is the medium refraction index, $q(\lambda)$ is the quantic efficiency, $\epsilon(x,\lambda)$ is the detection efficiency and $f(x,\lambda)$ is a term accounting for photon losses. All these terms must be integrated over the path of the emitted photon and over the Cherenkov light energetic spectrum. Figure 2.14 presents the simulated behavior for the N_{exp} for the Aerogel and NaF [74].

A comparison of the different charge performances among ToF, Tracker and RICH was done for the 2003 ion beam test data. In this test a prototype of RICH (the mini-RICH), 6 flight model ladders and 4 scintillating counters where tested together with an external trigger (figure 2.15).

While ToF provide charge measurement with a very good resolution for charges $Z \leq 10$, the RICH and Tracker can distinguish particles up to Iron and beyond. A RICH charge confusion at 10 % and a Tracker charge confusion of the order of 5 % per plane have been achieved in the beam test ([72], [74] and this work).

2.2.2 Rigidity Measurement

The magnetic rigidity R of a particle with momentum p and charge eZ is related to the magnetic field B by the measurement of the curvature radius r:

$$R = \frac{p}{eZ} = Br$$

the rigidity can be measured by the sagitta method. Following conventions presented in figure 2.16 where S is the sagitta, L the external planes distance, θ the angle of the circular sector, in the approximation of small angles results:

$$L = 2r\sin\frac{\theta}{2} \approx r\theta$$

$$S = r\left(1-\cos\frac{\theta}{2}\right) \approx r\frac{\theta^2}{8} = \frac{BL^2}{8R}$$

considering a minimum of three points x_1, x_2 and x_3 for the determination of the sagitta,

$$S = x_2 - \frac{x_1+x_3}{2} \qquad \sigma_S = \sqrt{\frac{3}{2}}\sigma_x$$

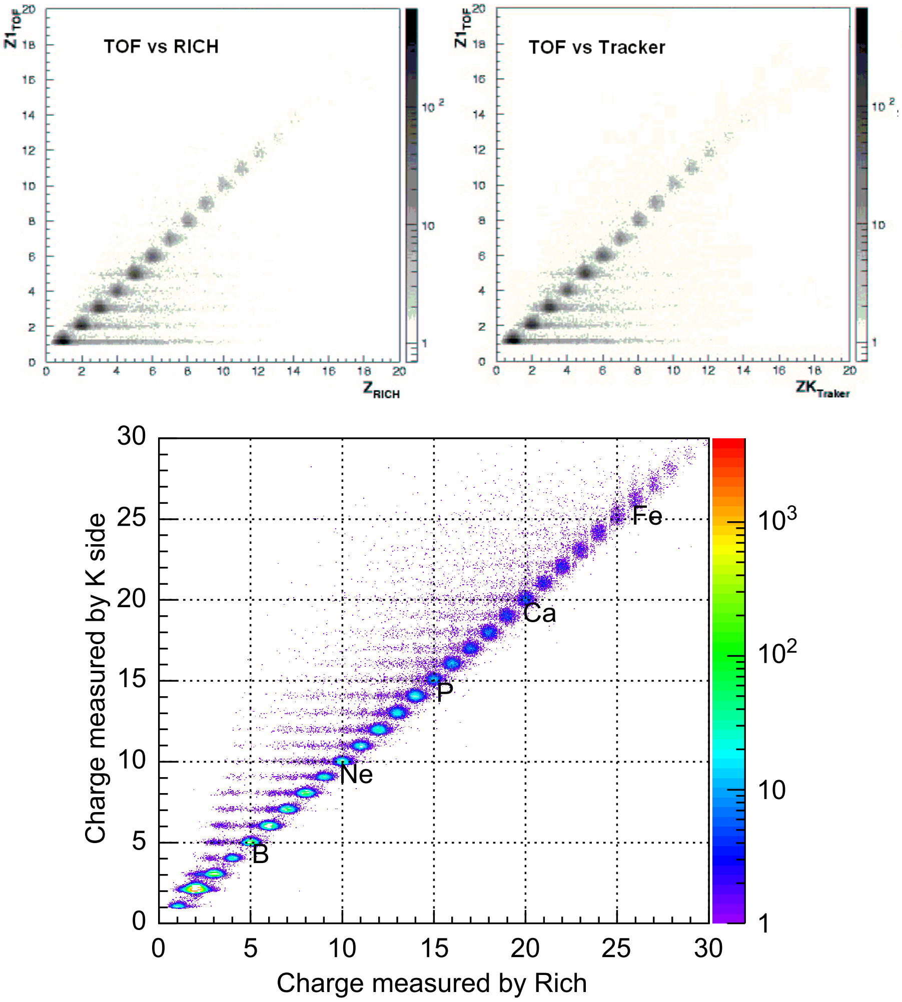

Figure 2.15: A comparison in a window of 50k events of the combined charge estimation from RICH prototype, 6 flight ladder modules and 4 scintillation counters [72] [77].

from the relation $S = BL^2/8R$ sagitta and rigidity has the same relative error, resulting:

$$\frac{\sigma_R}{R} = \frac{\sigma_S}{S} = \sqrt{\frac{3}{2}\frac{8R}{BL^2}}\sigma_x$$

In the real case the precise description of the AMS-02 magnetic field allows the numerical calculation of the charged particle track and the consequent reconstruction of the magnetic rigidity.

Figure 2.16 presents the simulated rigidity resolution for 8 Tracker planes.

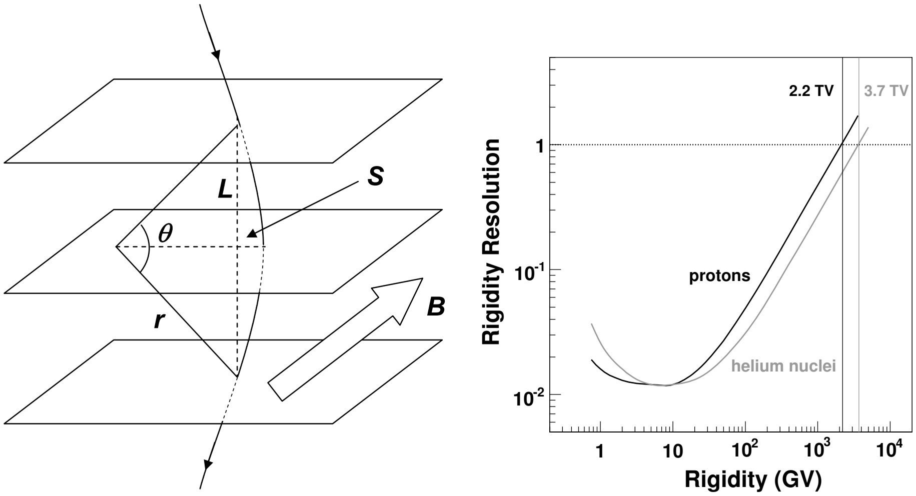

Figure 2.16: The sagitta method of rigidity calculation is schematized in the left plot. On the right the simulated behavior of the rigidity resolution for protons and Helium nuclei [1].

Considering a spatial resolution of ~ 10.7 (6.5) µm for protons (Helium) in the bending direction and a bending power $BL^2 = 0.87$ Tm^2 a Maximum Detectable Rigidity (MDR) of 2.2 (3.7) TV and a rigidity resolution of ~ 10 % up to GV rigidities is obtained. The observed resolution degradation at low rigidities is a consequence of the *multiple Coulomb scattering* [76].

2.2.3 Velocity Measurement

In AMS-02 velocity measurement are performed by the ToF system and by the RICH detector. The RICH performs a better β evaluation respect to ToF system, it is available only in the ~ 60% of the events while ToF measurement is always available.

Particle velocity measurement with ToF is done considering the length of the reconstructed track in the magnetic field (L), and the time difference between the passage of the particle in the upper and lower scintillators (Δt):

$$\beta = \frac{1}{c}\,\frac{\Delta t}{L}$$

The error on β is dominated by the time-of-flight resolution:

$$\frac{\sigma_\beta}{\beta} = \frac{\beta\, c}{L}\,\sigma_{\Delta t}$$

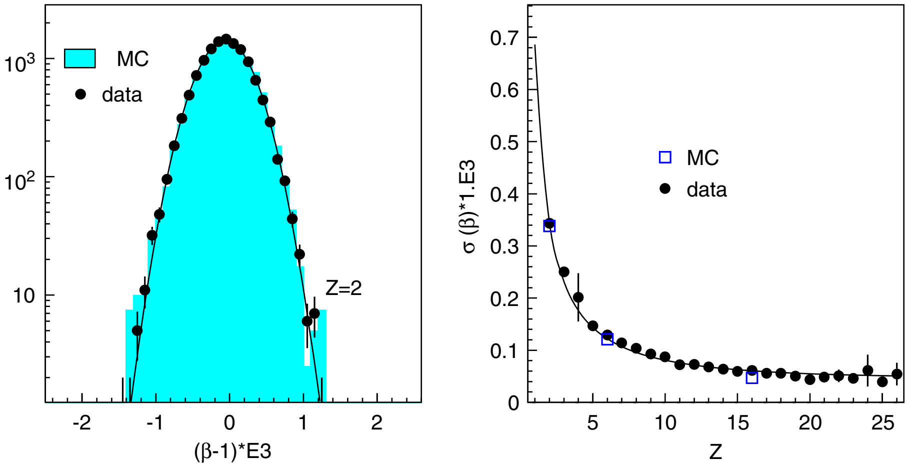

Figure 2.17: On the left the RICH Gaussian fit to reconstructed β spectrum for Helium particles. On the right the charge dependence of the velocity resolution [74].

where $\sigma_{\Delta t}$ accounts for three different sources:

- $\sigma_1/\sqrt{N_{\text{p.e.}}}$: a term depending on the number of emitted photon;
- $\sigma_2 \Delta x/\sqrt{N_{\text{p.e.}}}$: a term which takes in account the light attenuation between the scintillation site and the PMT (Δx). Also this term depends on the number of emitted photon;
- σ_3: a term accounting for electronic noise.

The measured resolution at test beam (figure 2.6) results $\Delta\beta/\beta \simeq 3\%$ for protons and $\Delta\beta/\beta \simeq 1\%$ for ions.

A very precise particle velocity determination is obtained measuring the radius of the Cherenkov ring in the RICH detection plane. The shape of this ring, however, can be rather complicated and depends strongly on the incidence point on the radiator. The RICH reconstruction algorithm exploits the tracker information to get the incident point and the incidence direction, then it estimates, for each single detection cell over threshold, the possible β value (for the case of reflection on mirror, or for the direct arrival). The group of cells with similar β is selected as the Cherenkov ring, and the β measurement is the average value of the distribution. A RICH stand-alone algorithm has also been developed, in this case a reconstruction of the whole Cherenkov cone must be performed and the resulting reconstruction efficiency is smaller. Figure 2.17 (left) shows the beam test β distribution measurement achieved for Helium.

The charge dependence of the velocity resolution is obtained by integration of the Frank-Tamm formula which gives the number of Cherenkov photons:

$$N = N_0\, Z^2\, L \sin^2\theta_C$$

where L is the radiator length and N_0 is the detector response, that includes RICH acceptance, efficiency and transmittance. The number of emitted photons follows the Poisson statistics:

$$\frac{\sigma_N}{N} = \frac{1}{\sqrt{N}} = 2\sigma_{\theta_C}\frac{1}{\tan\theta_C}$$

considering $\beta = (n\cos\theta_C)^{-1}$ results:

$$\frac{\sigma_\beta}{\beta} = \tan\theta_C\sigma_{\theta_C} = \frac{\tan^2\theta_C}{2\sqrt{N}}$$

Since $N \propto Z^2$ a β resolution improvement is observed for increasing charges of the incident particle.

Figure 2.17 (right) shows test beam measurements of the β resolution for different particles, $\Delta\beta/\beta \simeq 0.1\%$ is observed for protons and $\Delta\beta/\beta \simeq 0.01\%$ for ions.

2.2.4 Mass Measurement

The mass determination is the combination result of the rigidity, charge and velocity measurements.

$$m = \frac{Z\,e}{c}\,\frac{R}{\beta\,\gamma}$$

the resulting relative error is:

$$\left(\frac{\Delta m}{m}\right)^2 = \left(\frac{\Delta R}{R}\right)^2 + \gamma^4\left(\frac{\Delta\beta}{\beta}\right)^2$$

With a Tracker rigidity resolution better than 5% up to 50 GV the velocity resolution term is the leading term in the mass relative error equation. A clean separation between two isotopes with a mass difference of 1 amu requires a maximum gaussian spread of $\Delta m \sim 0.3$ amu. As a consequence the isotopic distinction results possible up to energies of 10 GeV/n and for masses up to Carbon nucleus. Figure 2.18 shows an example of the expected separation of ^{9}Be and ^{10}Be nuclei obtained with the AMS-02 Monte Carlo simulation.

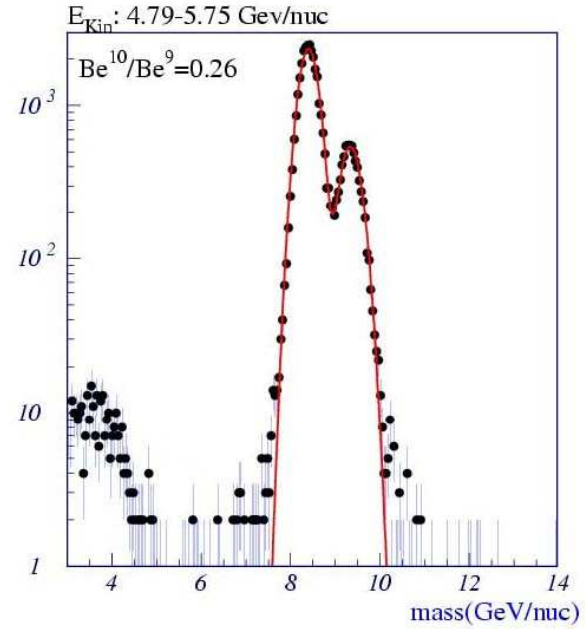

Figure 2.18: The expected ^{10}Be ^{9}Be mass separation calculated with the AMS-02 Monte Carlo simulation. Only an energetic bin around 5 GeV/n is here presented.

2.2.5 Trigger for Ions

The AMS-02 trigger for charged particles is built from the coincidence of at least 1 upper and 1 lower scintillators of the ToF detector and the anti-coincidence with the ACC system signals. The request of an ACC hit is meant to veto particles entering in the Tracker with a large inclination. Several other effects, however, can also fire the anti-coincidence system:

- Δ-rays production in the TRD, in the ToF and in the planes of the Silicon Tracker. The number of Δ-ray increases with Z^2 of the incident particle;
- inelastic nuclear interaction (fragmentation) in TRD, ToF, Tracker and in passive materials may generate a large number of nuclear products;
- ions or electrons incident on the ECAL, (~ 20 % of AMS-02 acceptance) can generate back-splash particles.

The number of ACC hits due to these effects depend both on the particle charge and energy. Figure 2.19 presents the trigger efficiency for simulated

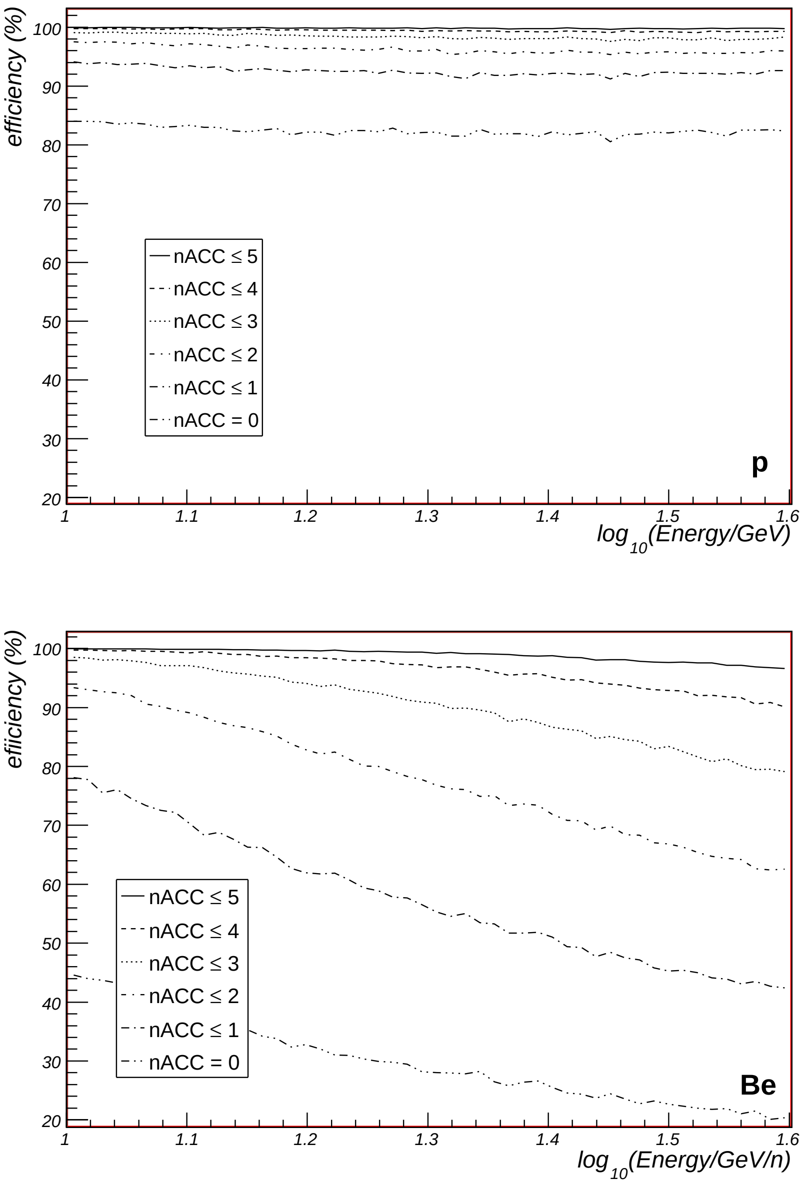

Figure 2.19: Trigger efficiency for 10^6 simulated protons and Beryllium nuclei with energies in the range [10, 40] GeV/n. The different curves correspond to an increasing number of ACC hits accepted in the trigger.

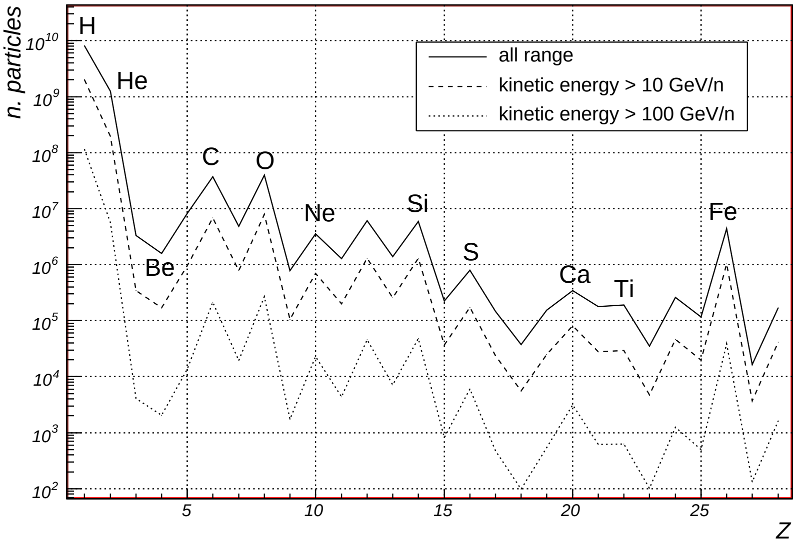

Figure 2.20: The AMS-02 expected statistic considering the geomagnetic cut-off in different energy ranges: (a) full spectrum, (b) kinetic energies ≥ 10 GeV/n, (c) kinetic energies ≥ 100 GeV/n.

protons (top) and Beryllium nuclei (bottom) with energies in the interval [10, 40] GeV/n, each line corresponds to a different trigger configuration, in which we accept at maximum $N_{\rm Max}^{\rm ACC} = 0, 1, 2, 3, 4$ or 5 hits in the ACC system.

It appears evident that a trigger with $N_{\rm Max}^{\rm ACC}$=2 which has an efficiency of 90 % for protons, introduces a serious bias for the Beryllium (and higher) nuclei. Conversely a trigger with $N_{\rm Max}^{\rm ACC}$=5, would include a lot of protons crossing the tracker with a large angle and increase significantly the trigger rate to a not acceptable value.

The solution adopted in AMS-02 is to implement distinct trigger for $Z = 1$ and $Z > 1$ particles, the two triggers differ for the value of $N_{\rm Max}^{\rm ACC}$. The event by event selection of the active trigger, is based on the amount of scintillation light produced while traversing in the first ToF plane.

2.3 Expected GCRN Measurements

Cosmic rays fluxes, simulated with the GALPROP galactic cosmic rays propagation tool, have been modulated for the 2009 solar activity and for the

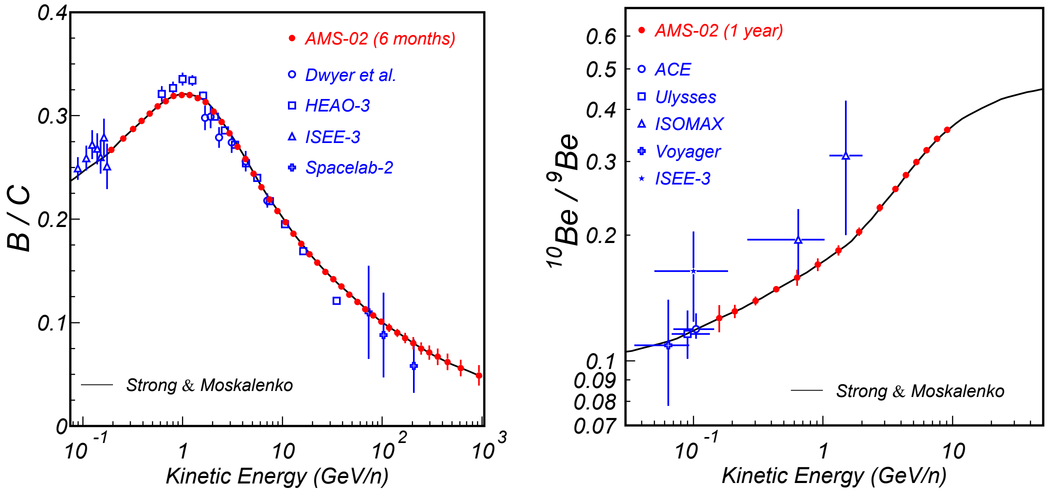

Figure 2.21: Projected ratio measurements: (left) 6 months of AMS-02 $\sim 10^6$ particles of Boron and Carbon, (right) 1 year of AMS-02 for $\sim 10^6$ particles of Beryllium isotopes [79].

geomagnetic rigidity cutoff at the ISS orbit (50° inclination and $\sim$ 400 km altitude). The integral of these fluxes within the AMS-02 acceptance and energy range (100 MeV/n to few TeV/n) gives the expected particle rates.

Considering the AMS-02 large geometric acceptance (0.45 m^2sr) and a three years data taking period, the resulting exposure factor is $\approx 10^4$ $m^2 \cdot sr \cdot h$. Multiplying the rates by three years of data taking it is possible to obtain an all species expected statistic of the order of 10^{10} particles, substantially dominated by the proton flux.

The expectations for GCRN are: 10^7–10^8 events for the most abundant species, as Carbon, Boron and Iron, and 10^5–10^6 events for the less abundant species, as the sub-Iron group (figure 2.20).

A large statistic is expected also restricting to the high energy part of the spectrum ($>$ 100 GeV/n) where as example 10^5 Boron and Carbon events are expected. As a consequence the secondary-to-primary ratios, as B/C or sub-Fe/Fe, will be measured with high precision up to few TeV/n.

On figure 2.21 (left) the AMS-02 Monte Carlo simulation of B/C ratio is presented (statistic errors only) compared to the most precise present measurements (as described in chapter 1).

An isotopic separation up to Carbon and up to 10 GeV/n is foreseen for AMS-02. After 3 years of data taking, AMS will identify 10^8 D, 10^8 ^{3}He and 10^5 ^{10}Be. In particular the large number of Beryllium nuclei will reveal the structure of the ^{10}Be/^{9}Be ratio up to 10 GeV/n (figure 2.18 right).

AMS-02 will improve the knowledge about CRs origin, acceleration and propagation mechanism, reducing the astrophysical uncertainties on the diffusion models. The consequent availability of more realistic predictions about secondary anti-proton and positron spectra would allow to better understand the AMS-02 accurate measurements on these rare CR components and will help to reveal the possible presence of structures coming from the Dark Matter component of the Universe (WIMP annihilation).

Chapter 3

Beam Test Experimental Setup

The AMS tracker basic element is a double-sided $72 \times 41 \times 0.3$ mm^3 silicon microstrip sensor operating in a regime of inverse polarization at full depletion. A variable number of sensors, from 7 to 15, are grouped along the non-bending direction to form a single electrical unit, the *ladder*, readout by low noise, high dynamic range charge sensitive amplifiers placed on a hybrid board on the ladder end. More than 4000 sensors have been produced and their electrical properties measured in order to choose the 2264 used in the assembly of the 192 flight ladders. Electrical test and gain calibration with radioactive ^{90}Sr source were performed at each major step in the ladder assembly to guarantee that no major change in the ladder properties was introduced due to uncorrect handling. At the same time, several ladder prototypes and flight units were tested on beam-lines of electrons, protons, ions and γ in order to study the ladder response to the different cosmic radiation components. In the October 2003 beam test, six flight spare ladders were tested on a ion beam of average energy 158 GeV/n, together with four time-of-flight scintillator counters and a Cherenkov prototype (mini-RICH). A total of $\sim$ 20 millions events were acquired.

In this chapter a general overview on the working principles of silicon sensors will be given and structural details of the AMS-02 Si sensors will be discussed. The Ladder structure and its operating conditions will be then reviewed. Finally, the experimental setup and the beam characteristics during the 2003 beam-test will be described.

3.1 Silicon Detectors

The most basic silicon sensor is a rectifying *pn* junction. The ionization produced by particles of charge eZ in the depletion region is drifted by the electric field toward the electrodes resulting a measurable induced signal proportional to $\mathrm{d}E/\mathrm{d}x \propto Z^2$. Reverse bias increases the sensitive depth, extending the depletion region to whole volume, increasing charge collection efficiency.

Strip detectors, resulting from an electrode separation into narrow strips each one read out by a separate electronic circuit, measure also the position of the particle traversing the detector. The pitch of the strip implantation can be of the order of tenth of microns, for a spatial resolution of the order of few µs. The electrode segmentation on both sides provides the measurement of the two coordinate from the same ionization.

The AMS-02 double-sided Silicon detector is designed to perform a simultaneous measurement of the x (non-bending) and y (bending) coordinate with precisions of the order of 30 µm and 10 µm for singly charged particles, and the absolute charge identification in a wide dynamic range (up to an energy deposition of few GeVs).

3.1.1 The *pn* Junction

Quantum mechanical electron waves diffraction in the periodic crystal lattice potential results in a structure of allowed and forbidden energy bands between the energy of the ground state and the free electron energy (the energy required for an electron to escape entirely from the material). The Fermi-Dirac statistics determines which of the quantum states in the energy bands are filled and which are empty. Near absolute zero temperature lower energy bands are filled up to the last valence band. With increasing temperature the thermal energy produces pairs of electron/holes in the material. Excited electrons can jump to the empty levels of the conduction band, becoming free to drift under the effect of an external electric field.

The density of free electrons (n), and holes (p) depends both on temperature (T) and on the characteristic energy gap E_{gap} between valence and conduction band. The mass action law establishes that the number of intrinsic carriers n_{i}, defined as $n_{\mathrm{i}}^2 = pn$, is a constant:

$$n_{\mathrm{i}} = AT^{3/2} e^{-\frac{E_{\mathrm{g}}}{2k_{\mathrm{B}}T}}$$

where A depends only from material properties and k_{B} is the Boltzmann constant. At the thermal equilibrium, the charge neutrality of the crystal implies $p = n = n_{\mathrm{i}}$. For pure Silicon the energy gap is $E_{\mathrm{gap}} = 1.19$ eV and the density of intrinsic carriers n_{i} at room temperature is $1.45 \cdot 10^{10}$ cm^{-3}.

Doping silicon with pentavalent or trivalent elements enhances the concentration of one type of free carrier. Pentavalent impurities *donors*, or

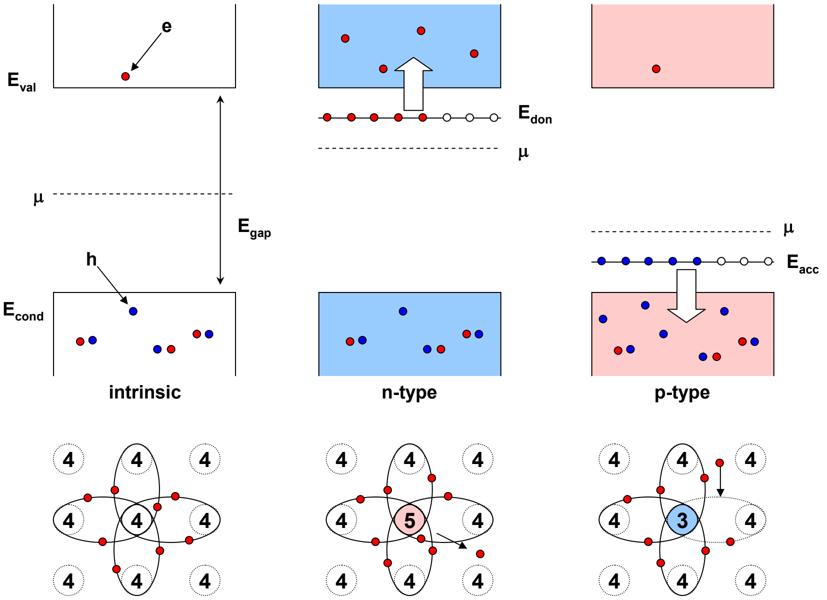

Figure 3.1: The energy bands and crystalline structure for intrinsic and extrinsic, i.e. doped, semiconductors are presented in the figure. From left to right: (a) in the intrinsic semiconductor a thermally exited electron can jump from the valence band to the conduction band, leaving an hole in the regular crystal structure; (b) introduction of donors, pentavalent elements, provide an extra energy level very close to the conduction band. At room temperature almost all the poorly bounded donor electrons in the extra level are in the conduction band; (c) Electrons are trapped and released by the crystal trivalent defects, resulting a hole-based conduction. The acceptor holes extra level is close to the valence band and at room temperature almost all holes are able to move freely (in the valence band).

n-type, in the Silicon crystal lattice introduce electrons poorly bounded in the periodic potential and placed on an extra energy level in the energy gap close to the conduction band ($\Delta E_{\mathrm{d}} \sim 0.01$ eV). Similarly trivalent impurities, *acceptors* or *p-type*, introduce additional holes resident, at temperatures near absolute zero, in an extra energy gap near the valence band (figure 3.1).

Typical doping density for Silicon detectors are of the order of $N \sim 10^{12}$ cm^{-3}, and in the case of heavily doped semiconductors $N^{+} \sim 10^{20}$ cm^{-3}. At room temperature the electrons in the shallow energetic levels in p-doped semiconductors are all in the conduction band. Similarly at room temperature holes in acceptors doped semiconductors are in the valence band. Considering the intrinsic carriers density negligible with respect to

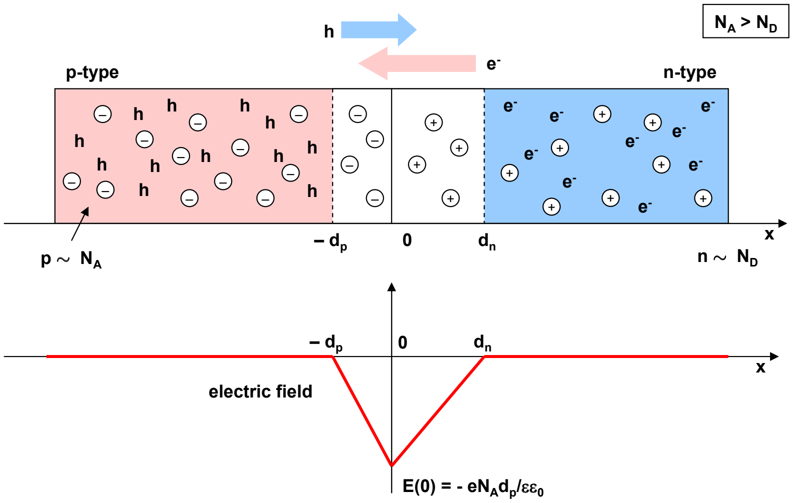

Figure 3.2: The *pn* junction. The recombination of majority carriers ends when and equilibrium between diffusion and the opposite drift, caused by the space region electric field (in the lower plot), is reached. Following the charge conservation $N_\mathrm{A} d_p = N_\mathrm{D} d_n$ and considering a p^+n junction, where $N_\mathrm{A} \gg N_\mathrm{D}$, the depletion depth is $d = d_n + d_p \approx d_n$.

the donor/acceptor densities and applying the mass active law results for n-type and p-type semiconductors:

$$n \simeq N_\mathrm{D} \qquad \rightarrow \qquad p \simeq n_i^2/N_\mathrm{D}$$

$$p \simeq N_\mathrm{A} \qquad \rightarrow \qquad n \simeq n_i^2/N_\mathrm{A}$$

where N_D and N_A are the donor and acceptor impurity density.

When p-type and n-type doped semiconductors are joined along a surface, the thin region surrounding the contact surface constitutes a *pn junction*. As sketched in figure 3.2, the junction region is characterized by a carrier depleted region created by diffusion and recombination of majority carriers around the junction. In this region the lack of carriers reveals the donors (positive) and acceptors (negative) sites, resulting a space charge region with an inverse electric field. The diffusion stops when a balance between the diffusion current, caused by the carrier inhomogeneity, and the drift current, caused by the electric field $E(x)$, is established:

$$\mu_e n(x) E(x) = -D_e \frac{\mathrm{d}n}{\mathrm{d}x}$$

$$\mu_h p(x) E(x) = D_h \frac{\mathrm{d}p}{\mathrm{d}x}$$

where μ_e, μ_h are the electron and hole mobility and D_e, D_h the diffusion coefficient. In Silicon electron mobility is approximately 3 times the holes one: $\mu_e = 1350\ \mathrm{cm}^2(\mathrm{Vs})^{-1}$ and $\mu_h = 480\ \mathrm{cm}^2(\mathrm{Vs})^{-1}$. Diffusion coefficients are related to mobilities by the Einstein-Nernst relations $\mu_e = eD_e/k_\mathrm{B}T$, and $\mu_h = eD_h/k_\mathrm{B}T$. Resolving the two equations with respect to the electric field $E(x)$ and integrating in the space charge region, the built-in potential results:

$$\phi_{\text{buit-in}} = \frac{k_\mathrm{B}T}{e} \log \frac{N_\mathrm{D} N_\mathrm{A}}{n_\mathrm{i}^2}$$

At room temperature in typical doping condition $\phi_{\text{buit-in}} \sim 100$ mV. While the depth of the depletion region can be calculated using the Poisson law:

$$-\nabla^2 \phi(x) = \frac{\rho(x)}{\epsilon\epsilon_0}$$

where $\epsilon\epsilon_0$ is the dielectric constant of the material ($\epsilon_{\mathrm{Si}} = 12$) and $\rho(x)$ is the charge density. Assuming an ideal step junction, the spatial charge density can be written as (figure 3.2):

$$\rho(x) = \begin{cases} 0 & x \geq d_n \\ eN_\mathrm{D} & 0 \leq x < d_n \\ -eN_\mathrm{A} & -d_p \leq x < 0 \\ 0 & x < -d_p \end{cases}$$

Following the neutrality condition: $N_\mathrm{D} d_n = N_\mathrm{A} d_p$, the depletion region will penetrate into depth in the side where the lower impurity density is present. In a p^+n junction, where $N_\mathrm{A} \gg N_\mathrm{D}$, the depletion region width will be described as:

$$d = d_n + d_p \approx d_n = \sqrt{2\epsilon\epsilon_0 \rho_n \mu_e \phi_{\text{built-in}}}$$

where $\rho_n = (eN_A\mu_e)^{-1}$ is the resistivity of the n-side material. For Silicon $\rho_n = 2.3 \times 10^4 \Omega\mathrm{cm}$ and the built-in depletion region depth is of the order of ~ 100 nm.

Applying a reverse bias V_0 on the junction, the number of intrinsic carriers is modified, and electrons and holes are forced to recombine resulting in an increase of the depletion region. Full-depletion is obtained when there is the complete recombination of all the carriers in one of the two sides of the junction (the one with the lower doping level). Reversing the previous expression:

$$V_{\text{full-dep}} \simeq \frac{L^2}{2\epsilon\epsilon_0 \mu_e \rho_n}$$

For a high resistivity ($\rho \sim 7k\Omega$cm) Silicon bulk of $L = 300$ µm at room temperature the full-depletion bias voltage is of the order of ~ 100 V. In the full-depletion mode the junction acts as a capacitor with $C = \epsilon\epsilon_0 S/L$ where S and L are the area of the junction interface and the junction depth.

While the majority carriers are stopped by the reverse bias potential, the thermally generated minority carriers (electrons on p-side, or holes in n-side) are diffused by the density gradient and drifted by the electric field over the junction. Their concentration decreases exponentially from the junction resulting in a leakage charged particles current density at the edges of the depletion region of [80]:

$$J^{\text{gen}} = J_e^{\text{gen}} + J_h^{\text{gen}} = n_{\text{i}}^2 \frac{L_h L_e}{N_{\text{D}} N_{\text{A}} \tau_n \tau_h}$$

where τ_n and τ_h are the carriers diffusion times, and $L_e = D_e \tau_e$ and $L_h = D_h \tau_h$ are the carriers diffusion lengths. In the case of the p^+n junction the minority holes current is greater than the electron one giving a $J \approx N_{\text{A}} L_h / \tau_h$. Integrating and multiplying for the carrier charge a leakage current of the order of 1 µA is obtained. The leakage current is strongly related with temperature while is nearly independent from the reverse bias applied.

When the junction reverse bias mode is too high a breakdown of the dielectric medium can occur, i.e. a strong current appears in the direction of the external electric field. The breakdown can be caused by several instances:

> Heat instability: heat produced by residual currents increments the electron/hole thermal pairs. This corresponds to a increment of minority carriers current and of the heat dissipated in conduction. This cycle results the junction breakdown.
>
> Tunneling effect: a tunneling current may appear in silicon if the field is around 10^6 V/cm. This situation is possible when both the p and n sides are highly doped. The tunneling breakdown voltage decreases when the temperature increases.
>
> Avalanche multiplication: electron-hole pair of thermal origin accelerated by the electric field acquire an energy high enough to ionize crystal atoms, and to origin an ionization avalanche. The breakdown voltage due to avalanche multiplication increases with temperatures.

3.1.2 Silicon Detectors

A ionizing particle passing through a Silicon bulk generates electron-holes pairs. Considering the typical value of 3.6 eV ofthe energy needed to generate a e/h pair in Silicon and the energy loss of a minimum ionizing particle

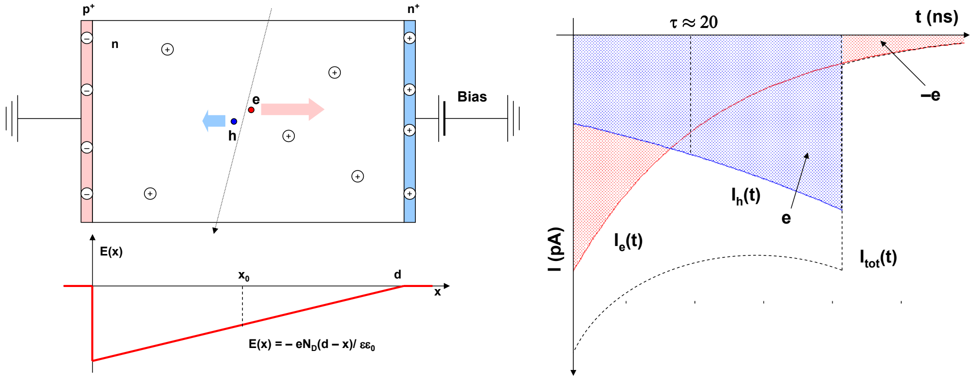

Figure 3.3: Left: operating principle of a reverse-biased silicon sensor as a particle detector. e/h pairs generated by the ionizing particle are drifted to n^+/p^+ layers by the electric field. The full depletion ensures that the active region extends through the whole sensor thickness. Right: Time evolution of the hole (I_h, blue) and the electron (I_e) components of the current (I_{tot},dashed)

in 300 µm of Si, an average of $\sim 2.2 \times 10^4$ pairs are obtained. In the *pn* depletion region, e/h migrate towards opposite sides of the junction being separated in the reverse electric field. The increment of the reverse voltage increases the depletion zone, enlarging the sensitive volume, and provides a more efficient charge collection due the increased electric field. The simplest Silicon detector (sketched in figure 3.3) is composed by an n-doped silicon bulk with p^+ and n^+ implantations on opposite surfaces, where the n^+ layer allows an ohmic contact with the conductor material and prevents the depletion zone from reaching the contact with the conductor electrodes. The detector is used in regime of full-depletion in order to have the maximum sensitive area and collection efficiency.

Electrons and holes produced by radiation in the depletion region migrate to the n^+ and p^+ side respectively, drifted by the electric field. The resulting electrical pulse on the electrodes arises from induction caused by the movement of charges rather than the charge collection itself. Approximating the p^+nn^+ junction as a p^+n junction at full-depletion the electric field results (figure 3.3):

$$E(x) = -\frac{eN_{\mathrm{D}}}{\epsilon\epsilon_0}(d_n - x)$$

defining as τ the time scale of propagation:

$$\tau = \rho_n \epsilon\epsilon_0 = \frac{\epsilon\epsilon_0}{eN_D\mu_e} \approx 20ns$$

the resulting drift equations for the electrons and holes are

$$v_e = \frac{d_n - x}{\tau} \qquad v_h = -\frac{\mu_h}{\mu_e}\frac{d_n - x}{\tau}$$

Resolving equations and calculating currents for a single electrode as $I = I_e + I_h$ (the behavior is presented in figure 3.3):

$$I_e = -\frac{e}{\tau}\frac{d - x_0}{d}e^{-\frac{t}{\tau}} \qquad I_h = -\frac{e}{\tau}\frac{\mu_h}{\mu_e}\frac{d - x_0}{d}e^{\frac{\mu_h}{\mu_e}\frac{t}{\tau}}$$

Different rise times result for electrons and holes. To calculate the expected pulse shape due to an incident radiation is necessary to integrate the ionization density along the particle trajectory taking into account the detailed electric field configuration, which can be highly distorted by the presence of large e/h generation levels.

Single-sided Si microstrip detectors are realized segmenting into strips the p^+ implantation over the n-doped silicon bulk, as sketched in figure 3.4 (upper plot). A thin insulator silicon oxide (SiO_2) layer is deposited on the bulk surface between p^+ strip. The e/h free carriers, generated by an ionizing particle, migrate along the electric field lines between the nearest p^+ strip and the n^+ layer.

For a digitally readout sensor, i.e. where the only readout information is the strip number where the highest signal is registered, the expected spatial resolution can be estimated as:

$$\sigma^2 = \frac{1}{p}\int_{-\frac{p}{2}}^{\frac{p}{2}} x^2 \mathrm{d}x = \frac{p^2}{12}$$

where p is the sensor readout pitch.

In many applications not all the p^+ strips are connected to the readout circuitry in order to minimize the number of acquisition channels. Typical readout schemes are based on alternating connections every two/four strips: charge collected on intermediate strips is capacitively transmitted to the neighbor readout strip through the strip-to-strip capacitance [81]. In an analog readout scheme, where also the intensity pulse high in different strips is recorder, excellent spatial resolutions ($\ll p/\sqrt{12}$) can be achieved evaluating the impact point of the ionizing particle by means of a center of gravity method.

In double-sided microstrip detectors also the n^+ layer is segmented in strips, in the orthogonal direction with respect to the p^+ strips layout (bottom of figure 3.4). However, a slight complication is inherent in this approach. The SiO_2 insulator contains positive charges able to attract some negative

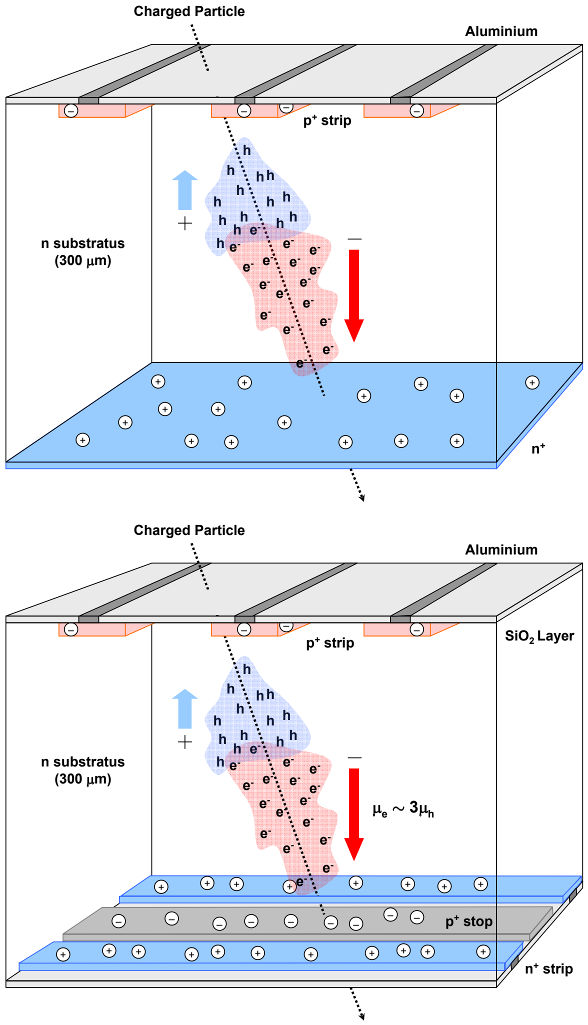

Figure 3.4: Single-sided (upper) and double-sided (lower) implantation schematic layout for Si microstrip detectors.

carriers, reducing the n^+ inter-strip resistance. One solution is to insert between each n^+ strip a p^+ strip, called *p-stop*, which will ensure proper strip insulation [81].

3.1.3 The AMS-02 Double-Sided Sensor

The AMS-02 Silicon sensor is a double-sided microstrip device of dimensions 72×41 mm^2. On the two surfaces of a high-resistivity n-doped Silicon substrate of 300 μm, p^+ and n^+ strips are implanted along orthogonal directions.

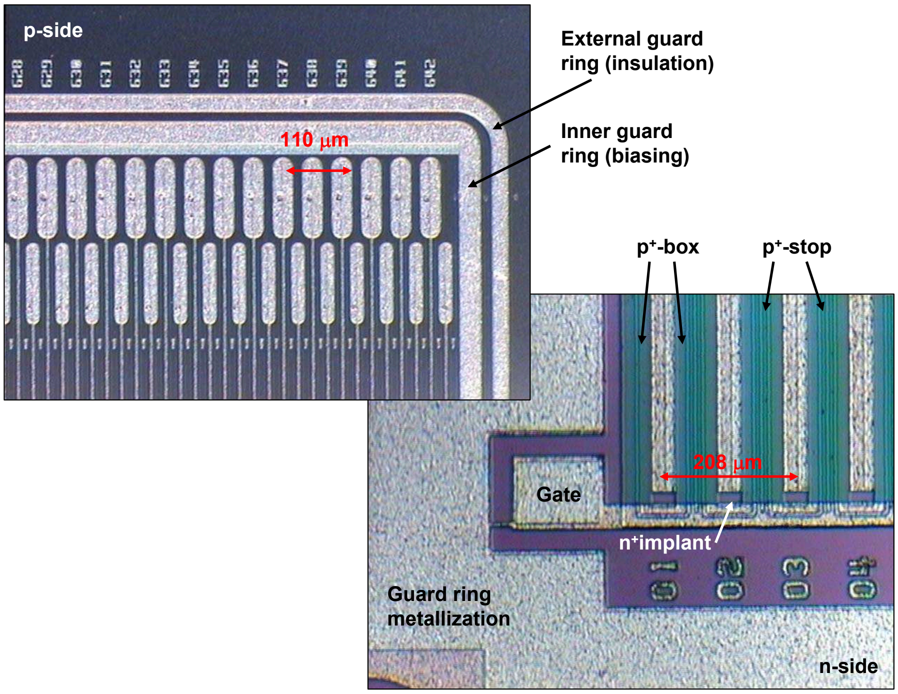

Figure 3.5: Details of the implantation pattern on the AMS-02 Silicon sensor.

Within the AMS reference system, the p^+ strips of the junction side run along the x direction to provide measurement of the bending coordinate (y), with an implantation (readout) pitch of 27.5 (110) μm. The n^+ strips of the ohmic side have a coarser implantation (readout) pitch of 104 (208) μm (the implantation structure is shown in figure 3.5). Two concentric p^+ implantations, the *guard-rings*, embed the microstrip structures on the junction sensor side. The innermost guard-ring is used for biasing purposes while the outermost one is left floating for insulation. Inter-strip insulation on the ohmic side is obtained surrounding each n$^+$ strip by rectangular p$^+$ implantations *p-boxes*, interleaved with *p-stops*.

Sensor are reverse-biased via the *punch-through* technique: a positive voltage is applied on the n-side guard ring (80 V is the operating voltage) while the p-side inner guard ring is kept to ground. Due to the close proximity of the guard-ring to the p$^+$ strips, guard-ring depletion extends to the strips region by thermoionic injection of free-carriers from the strips toward the guard-ring. As a result, the strips will be slightly forward biased with respect to the guard-ring (typically 3-4 V in AMS-02 biasing scheme) and reverse biased with respect to the n-bulk. All the strips are kept to the same operating potential, though not directly connected to the power-supply. A similar *surface-through* mechanism insures the n^+ strip biasing on the ohmic side.

On both sensor sides, microstrips are AC coupled to the readout electronics via a 700 pF capacitor in order to cut the steady component of the inverse junction current (leakage current).

In the AMS-02 acquisition scheme, only one every fourth (second) implanted strips are effectively readout on the p(n) sensor sides: this results in 640 (192) readout channels on the p(n)-side sensors. The charge sharing of the released ionization between different strips due to inter-strip capacitive coupling is exploited in order to achieve a 10 (30) µm resolution in determining the impact point of singly charged ionizing particle.

In figure 3.6 (top) the equivalent electric scheme for the shared collection of the charge signal is presented. The signal Q relative to the passage of a particle in correspondence of not read-out strip is divided on the two nearest readout strips according to the expression:

$$\frac{Q_R}{C_R} = \frac{Q_L}{C_L}$$

where $Q_{R/L}$ and $C_{R/L}$ are respectively the collected charge and the total interstrip capacitance seen on the closest readout strips positioned to the Right/Left of the impact position. The impact position of the incident particle will result from the Center-of-Gravity of the measured charge distribution:

$$C.o.G. = \frac{x_L Q_L + x_R Q_R}{Q_L + Q_R} = x_L + \frac{Q_R}{Q_L + Q_R} Np$$

being p the implantation pitch (27.5 µm) and Np the readout pitch (104 µm).

If the particle crossing is between two strips, the same charge sharing algorithm applies between the two closes strips, and then the signal is capacitively distributed to the closest readout strips.

A more realistic description of the capacitive charge sharing (figure 3.6, bottom) has to take in account not only the direct inter-strip capacitance to the first neighboring strips but also indirect coupling to the second and even third neighbors [82]. More over, the capacitive coupling to the backplane can degrade the charge collection efficiency absorbing part of the signal, for this reason the backplane capacitance is kept as low as possible compared to the inter-strip capacitance. As a matter of fact, even after a careful sensor design optimization, the detector response must to be evaluated, especially in the presence of high charge deposition, by experimental methods.

In figure 3.7 the square root of the average signal amplitude corresponding to different ion species is presented as a function of the particle impact

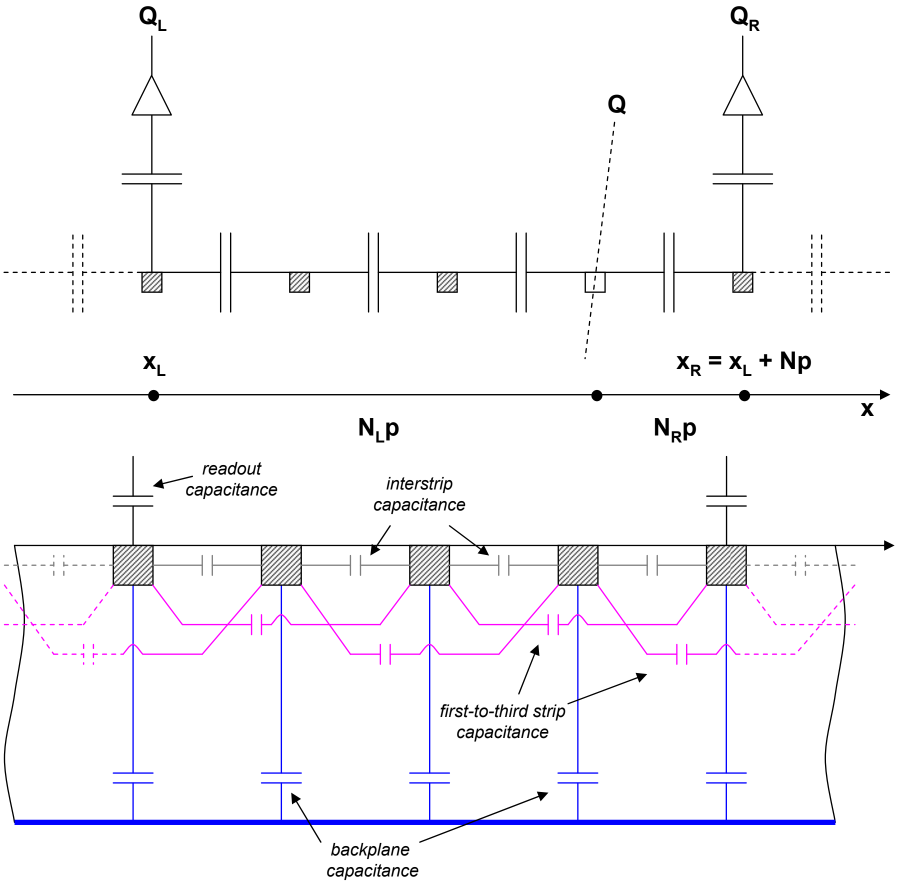

Figure 3.6: Equivalent electric scheme of the p-strips capacitive couplings. In the upper scheme is presented the charge sharing principle of functioning. The second scheme refers to a more accurate capacitive coupling model for Silicon detectors.

position between adjacent readout strips. On the p (left) and n (right) sides different charge collection behaviors are observed as a function of the inter-strip position.

3.2 The Ladder

An exploded view of the AMS-02 ladder is presented in figure 3.8, the detailed description follows.

The ladder is composed of an array of a variable number of sensors, 7 to 15, glued to a Upilex kapton cable and supported by a light structure made

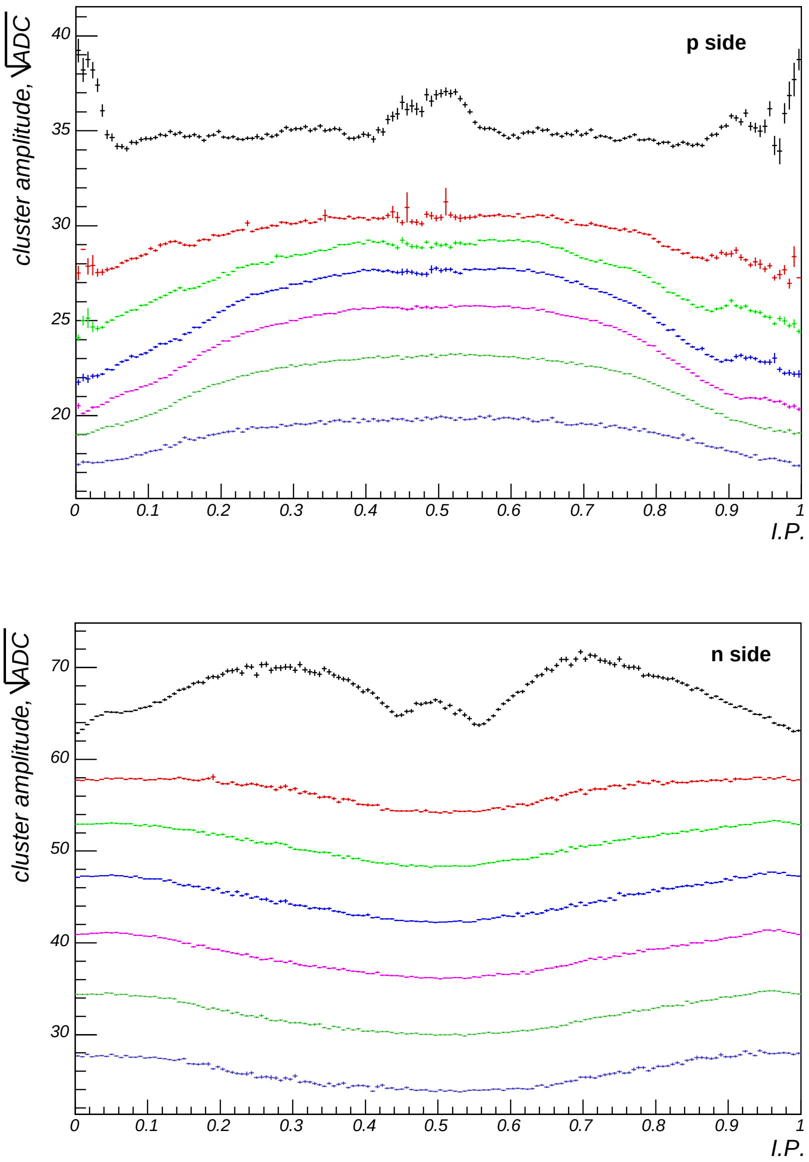

Figure 3.7: The average amplitude ($\sqrt{ADC}$) function of impact position (IP) of the first ladder for the p (n) sides is presented in the upper (lower) plot. IP is given with respect to the two readout strip position ($\sim$ 1. and $\sim$ 0.) between which the particle is passing. From the bottom are presented the different charges: Beryllium, Boron, Carbon, Nitrogen, Oxygen, Fluorine and Neon.

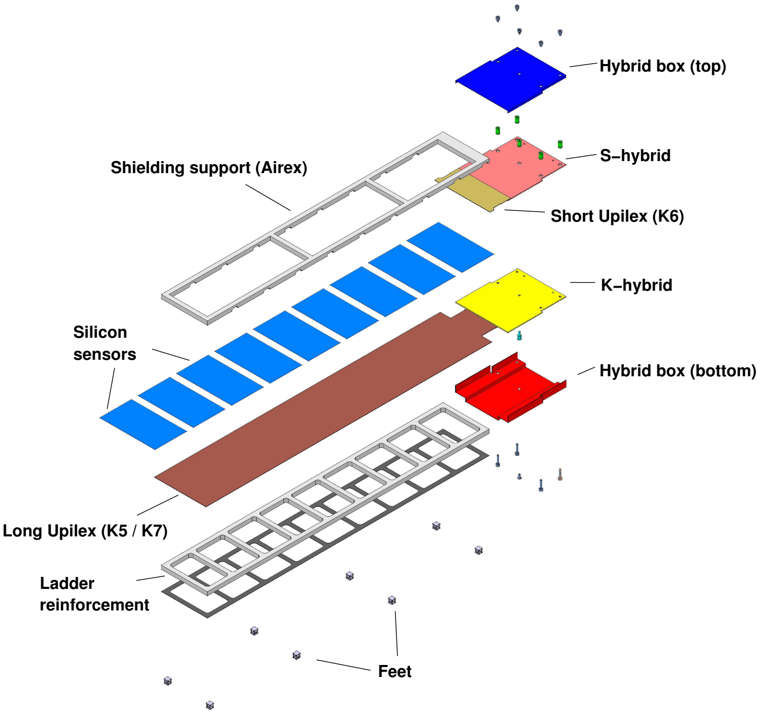

Figure 3.8: Exploded view of an AMS-02 ladder.

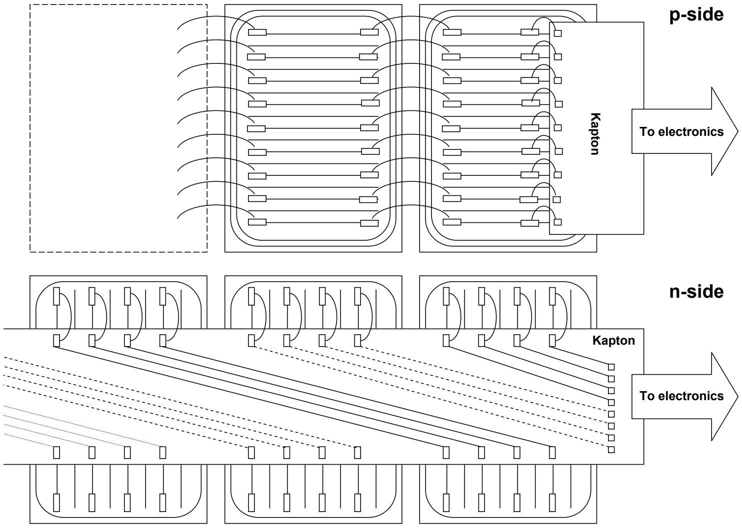

Figure 3.9: Bonding schemes of the p-side (top) and n-side (bottom) sensor channels to the readout front end electronics.

of Carbon skinned Airex. Feet are glued to the ladder reinforcement allowing fixation to the Tracker planes. The Airex reinforcement has been designed to ensure sufficient flexibility to sustain the strong vibrations during the Shuttle flight and to maintain the sensor positions with the required accuracy.

A second Airex foam, the spacer, is glued on top of the p-side in order to separate the Silicon surface from the metalized Upilex foil wrapped around the ladder. The role of this foil is twofold: it acts as an electromagnetic shield and it mechanically protects most of the Silicon surface. As a side-effect this electromagnetic shield also limits the amount of ambient light reaching the silicon surface [83].

Two PCB (hybrids), placed at one end of the ladder, are electrically and mechanically connected to the Si detectors by Upilex cables allowing for an optimized arrangement of the front-end electronics. The hybrid is surrounded by a protecting grounded Aluminium box.

On the p-side the strips are daisy chained with micro-wire bonds into the implantation direction. The short Upilex cable (upper plot of figure 3.9) provides the connection of the sensor with the front-end electronics. On the n-side strips are bonded to the Upilex cable which routes the signals to the readout electronics disposed on the ladder end. The routing scheme of the n-side cable distributes the strip signals of alternating sensors to the same readout channel, i.e. the 192 channels of the even sensors are coupled as for the odd sensors (bottom diagram of figure 3.9). The resulting ambiguity is resolved by a change of the readout pitch in selected regions of the external plane ladders, which introduces a shift of the readout strip scheme with respect to the ladders on the internal planes (the inner tracker). In total, a ladder has 1024 readout channels, 640 for the p-side, 384 for the n-side.

In figure 3.10 a) and b), the two ladder sides are shown before the shielding application. The complete flight ladder module with the hybrid placed vertically respect to the plane of revelation, with the purpose of maximizing the Tracker active area, is presented in figure 3.10 c).

3.2.1 The Ladder Readout Chain

The Tracker Front-End (TFE) electronics provide the coupling between microstrips and the digitization system. A system of 700 pF capacitors provide the AC coupling between strips and the VA readout chip. The VA, version Hdr9A of the original Viking design, is a high dynamic range 64 channels charge-sensitive amplifier, semi-Gaussian shaper circuit, with simultaneous sample-and-hold stage. VA and capacitor chips are located on a standard printed circuit hybrid board which is connected to the ladder by a flexible Upilex cable. The p-side (n-side) hybrid contains 10 (6) VA chips for a total

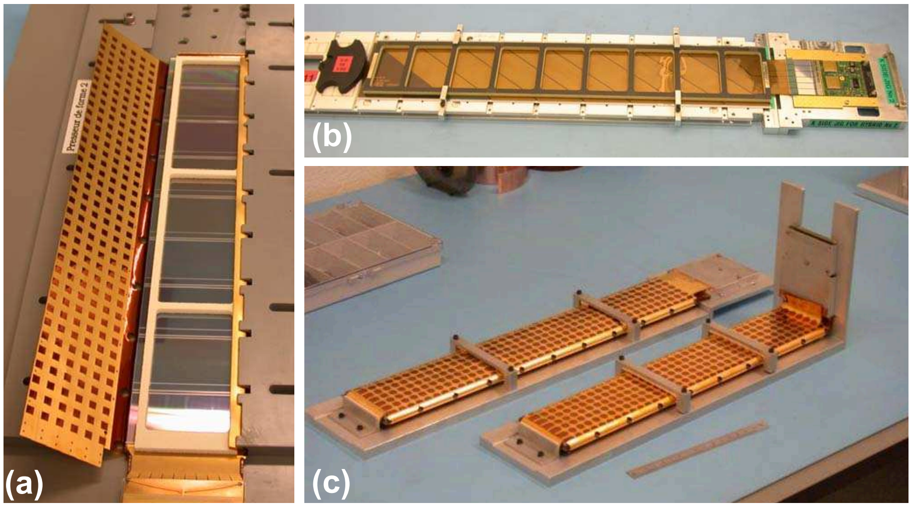

Figure 3.10: Photos of the ladder construction: (a) the p-side before the shielding, the sensor structure is exposed; (b) the ladder n-side, the Upilex foil and the routing scheme is clearly recognizable; (c) the ladder after the shielding phase.

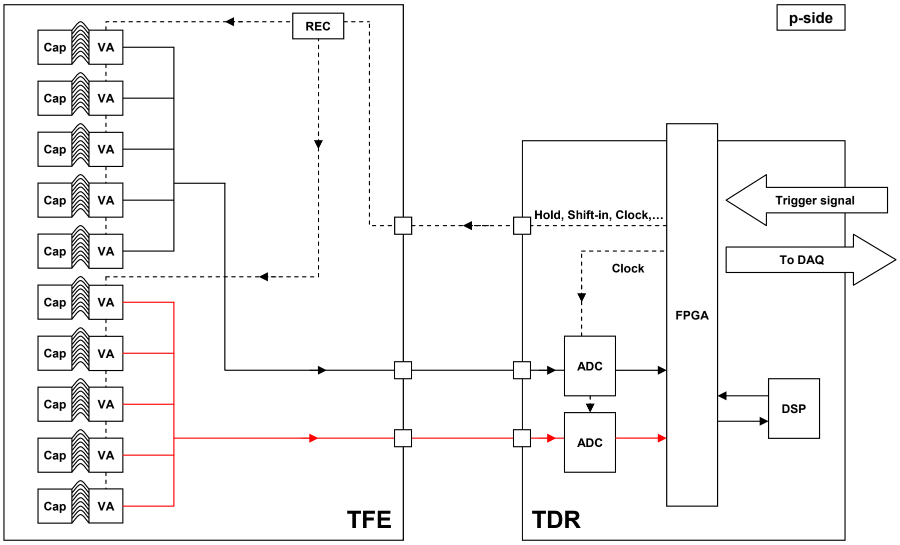

Figure 3.11: Logic diagram of the p-side readout: the hybrid (TFE) couples the Silicon strip detector to the digitization and data processing board (TDR)

of 640 (384) readout channels. The VA operates at low biasing current, with a measured power consumption of 0.7 mW per channel. The latch time, the difference in time between the passage of the particle and the sampling of the signal at the output of the shaper, is of the order of 4 µm. The dynamic range for a single channel is ~ 100 MIPs signal, with a linear response up to ~ 75 MIP [84].

The Tracker Data Reduction board (TDR) houses the electronics which perform both the digitization of the strip signals and the on-line data reduction. The analog signal output from the TFE is amplified by an analog receiver at the input of the TDR. The strips signals are multiplexed on the TFE into three streams and sent, via flat coaxial cables, to analog receivers and to 12 bit analog-to-digital converters. The digitization in the ADC is performed at a clock frequency of 5 MHz, as a compromise between the quality of the signals and the total readout time (of ~ 80 µs).

A Field Programmable Gate Array (FPGA) controls the data flow from the ADC to the memory buffers. A Digital Signal Processor (DSP) is programmed to take the events from the buffers and perform the calibration and the on-line data reduction.

3.2.2 Calibration

The signal readout from a single ladder channel has different components, related to leakage current fluctuations, bias effects and electronic noise in the readout chain.

Denoting with x_k^{ij} the ADC signal amplitude of the i-th channel on the j-th VA preamplifier in the k-th event:

$$x_k^{ij} = p^{ij} + cn_k^j + s_k^{ij} + q_k^{ij}$$

- **pedestal**, p^{ij} is a signal bias characteristics of each readout channel due to constant processes, as the leakage current average fluctuation and the bias proper of the ADC system;

- **common noise**, cn_k^j is a signal bias shared in a single VA, due to the electronics coupling, it is calculated and subtracted event by event on each VA.

- **noise**, s_k^{ij} is an event-by-event signal bias relative to single channel leakage current fluctuations and noise of the readout electronics. It is assumed to follow a gaussian distribution centered at zero and with variance σ^{ij}.

- **signal**, q_k^{ij} is the signal provided by the ionizing particle.

The calibration procedure consists in the determination of pedestals and noise for each readout channel. From the obtained results, flags the *dead* or *noisy* channels are identified and flagged to be excluded in the common noise calculation and in the cluster finding algorithm.

Calibration is performed acquiring data in the absence of ionization, i.e. with $q_k^{ij} = 0$. In the first calibration step, the pedestal is defined as the mean of the measured signal over collected N_{ped} events:

$$p^{ij} = \frac{1}{\text{ped}} \sum_{k=1}^{\text{ped}} x_k^{ij}$$

The signal fluctuations around the pedestal value, i.e. the variance of the collected signal distribution, define the *raw noise*:

$$\sigma_{raw}^{ij} = \sqrt{\frac{1}{\text{ped}} \sum_{k=1}^{\text{ped}} (x_k^{ij} - p^{ij})^2}$$

which is the effective convolution of the single channel fluctuations (σ^{ij}) and the VA chip common noise fluctuation (σ_{cn^j}).

Already at this step, *dead*/*noisy* channels can be identified as those channels having a raw-noise value very small/large with respect to the average σ_{raw} found the chip.

The channel noise is then evaluated as the variance of the signal acquired over N_σ events, subtracted on an event by event basis of the pedestal and the common noise value in that event. The channel noise results as:

$$\sigma^{ij} = \sqrt{\frac{1}{N_\sigma} \sum_{k=1}^{N_\sigma} (x_k^{ij} - p^{ij} - cn_k^j)^2}$$

where cn_k^j is defined on the k-th event as:

$$cn_k^j = \frac{1}{N_{good}} \sum_{i=1}^{N_{good}^j} (x_k^{ij} - p^{ij})$$

where the sum is extended only to those channels $\text{N}_{good}^j \leq 64$ of the VA which are neither *dead* nor *noisy*. The noise receives contributions both from the Silicon sensor dark current fluctuations and the electronic noise of the readout electronics.

The calibration procedure is automatically executed periodically, in order to take in account the temperature differences during the daily thermal cycle,

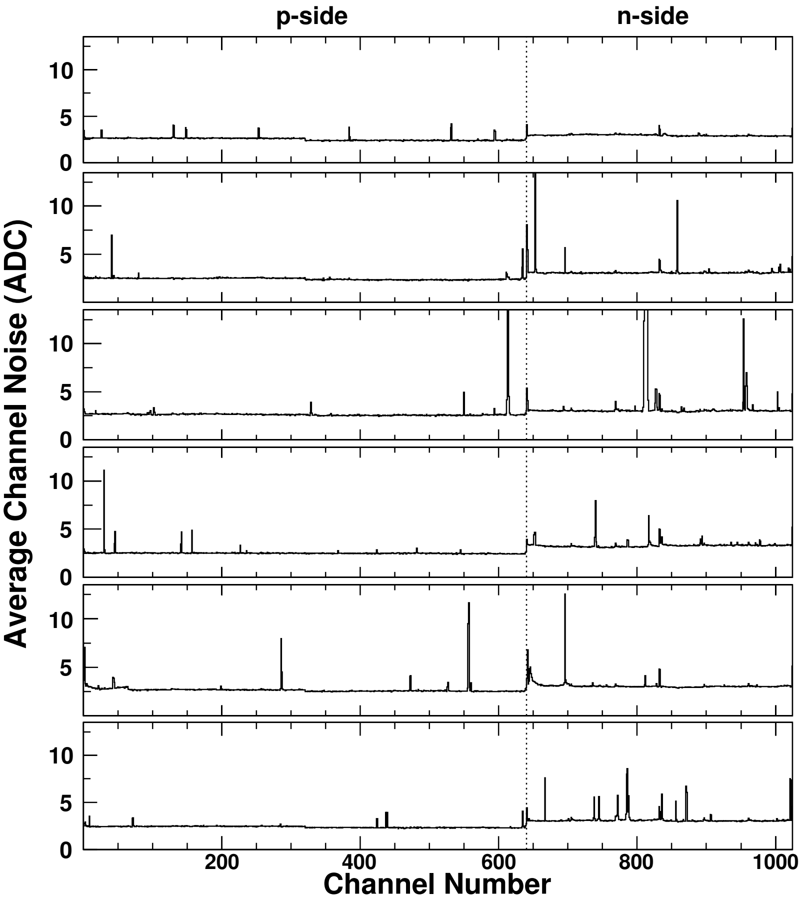

Figure 3.12: The average noise measured in the beam test 2003. The six plots refers to the six ladders under test. Channels from 1–640 refer to the p-side and 641–1024 to the n-side. The measured average noise is of the order of ~ 2 ADC counts with ~ 1 % of dead/noisy channels [1].

by the TDR under the specific command mode. Results, in terms of pedestal, σ_{raw}, σ and status of each strip are saved in local memory for further use in the online data reduction and retrieved externally to the system for off-line data analysis.

3.2.3 Data reduction

The data reduction procedure, executed in compressed readout mode by TDR board, provides a first suppression of channels with no signal associated to a particle. The algorithm has to fulfill several requirements:

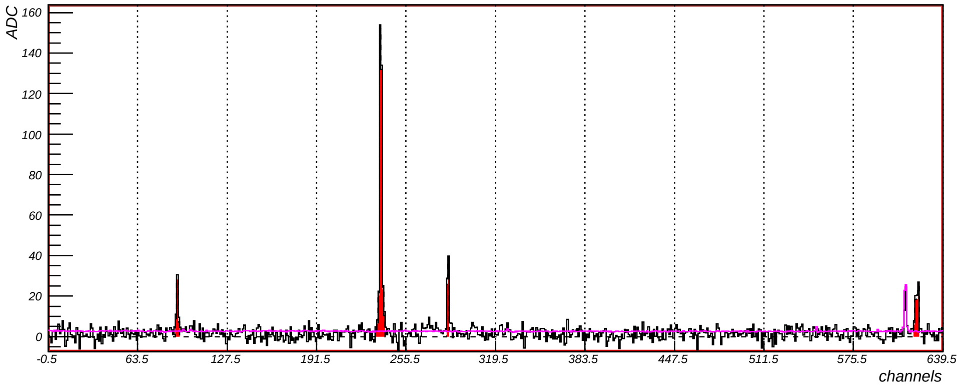

Figure 3.13: Black line: the pedestal and common noise subtracted signal; Purple line: the channel noise σ, note the few noisy channels on the right; Red areas: the signal resulting from the clusterization procedure.

- a conservative approach: loose selection cuts should be applied to avoid any significative efficiency loss;

- a data reduction factor of ~ 1000 in order to keep a manageable data flow for the whole tracker with respect to a downlink for data transfer of 2 Mbit;

- a short execution time in order to follow a mean trigger rate expected to vary from 200 to 2000 Hz, depending on the geomagnetic latitude.

The raw event data, i.e. signals provided by the 192k channels x_k^{ij}, are subtracted by the pedestal value. The computation of the common noise cn_k^j in the single event is provided by a mean between those channels of the VA which are neither dead/noisy nor with a signal/σ ratio exceeding 10. This last condition excludes channels corresponding to a real physics signal that can bias the common noise calculation.

Due the capacitive coupling of the readout strips, a charged particle traversing the sensor induces a signal in few strips near the impact position. As a consequence, the typical signal is distributed over an ensemble of strips, the *cluster*. The signal over noise $SN = S/\sigma$ ratio is then used as a discriminant quantity to look for clusters. A signal-to-noise exceeding a given threshold of SN_{seed} is called *seed* and triggers the constitution of a cluster, which is built associating to the seed the neighboring strips with $SN > SN_{\text{neighbor}}$.

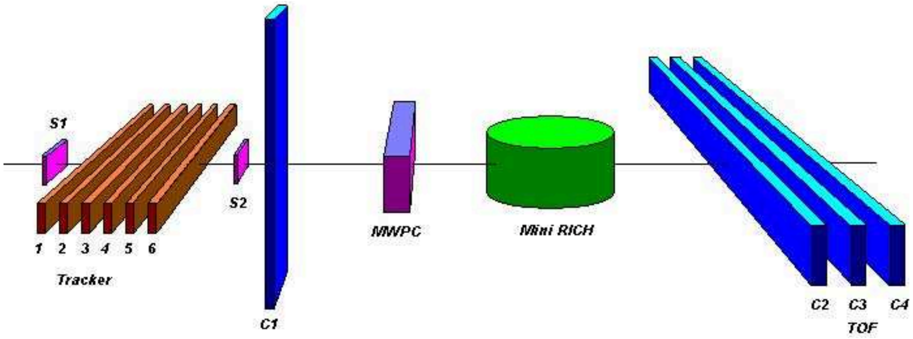

Figure 3.14: Test beam 2003 setup. One scintillator counter, C_1, of the TOF system was placed before the tracker telescope and three other counters, C_2, C_3 and C_4 were placed after the mini-RICH prototype. Scintillator paddles are added in order to provide an external trigger for the synchronous data acquisition of the three independent DAQ systems. Multi-wire proportional chambers before and after RICH prototype are used in order to reconstruct the impact point of the charged particle on the radiator.

In figure 3.13 presents the typical signal after the pedestal and common noise subtraction, the noise associated of each single strip, and the result of the clusterization procedure.

The reduction factor ($\sim$1000) requires a mean number of cluster per event, without bandwidth overcharging, of the order of $\sim$ 20 clusters. As a consequence a very low number of noise generated clusters can be accepted. The seed threshold has to be selected in order to provide an high rejection of the noisy clusters and, on the other side, the highest efficiency in protons cluster collection. From beam test data a reasonably signal-to-noise ratio is of order of 4 provides the required noise rejection and an efficiency of protons detection of 99 % on 6 planes over 8.

3.3 Beam Test

Six flight model ladders, an AMS RICH prototype [85] and four scintillator counters of the AMS TOF system [72] were tested on a ion beam at the CERN SPS H8 beam line in October 2003. The beam test setup is sketched in figure 3.14: one scintillator counter was placed before the tracker telescope, C_1, and three counters, C_2, C_3 and C_4 after the mini-RICH prototype. Two scintillator paddles (S_1,S_2) were providing the external trigger for a synchronous data acquisition of the three independent DAQ systems.

Multi-wire proportional chambers before and after the RICH prototype were used in order to reconstruct the impact point of the charged particle on the RICH radiator.

The secondary ion beam used in the test was produced from the fragmentation of a primary Indium beam (10^7 pps) with momentum of $158 GeV/c/n$ on a Lead target located just after the extraction channel of the SPS. The main characteristic of the fragmented beam is the conservation of the velocity of the incident particle by the fragments, resulting a conservation of the momentum per nucleon and a narrow angular spread. The momentum distribution had a resolution $\delta P/P \leq 1.5\%$ and the angular distribution was of the order of $\sim$ mrad. The intensity of the fragments emerging from the inelastic interaction was of $\sim 10^3 pps$ for a beam section of the order of $2--3$ mm [86].

Downstream of fragmentation target, the secondary products were filtered by a combination of magnetic dipoles transporting particles with the same fixed rigidity.

$$R = B\rho \approx 3.1\,\gamma\,\frac{A}{Z}$$

Given a fixed γ by kinematics a selection on B corresponds to a selection of the A/Z ratio. In the test beam were selected:

- $A/Z = 2$: this beam is composed mainly by Helium nuclei. Other odd nuclei are also present: ^{6}Li, ^{10}B, ^{12}C, ^{14}N, ^{16}O, ^{16}O, ^{28}Si, ..., ^{52}Fe, ... this selection gave a ion composition similar to the CR abundance distribution;
- $A/Z = 9/4$: Beryllium component is enhanced;
- $A/Z = 7/3$: Lithium component is enhanced;

In collisions were also produced protons with energies spreading from low to high energies. This gave the possibility of having low energy ($\sim 10 GeV$) proton beam with the selection $A/Z = 1$ [86].

In figure 3.15 is presented the global statistics resulting from the data taking of 10 days, and the relative statistics for the different A/Z selection ratio. In the whole test a $\sim 10^7$ events were collected with charges $1 \leq Z \leq 30$.

The TDRs were operated in raw mode, i.e. no online data reduction was performed and the digitized output of all channels was recorded. Out-of-spill data were used to perform an online calibration to determine the individual channel pedestal and noise values.

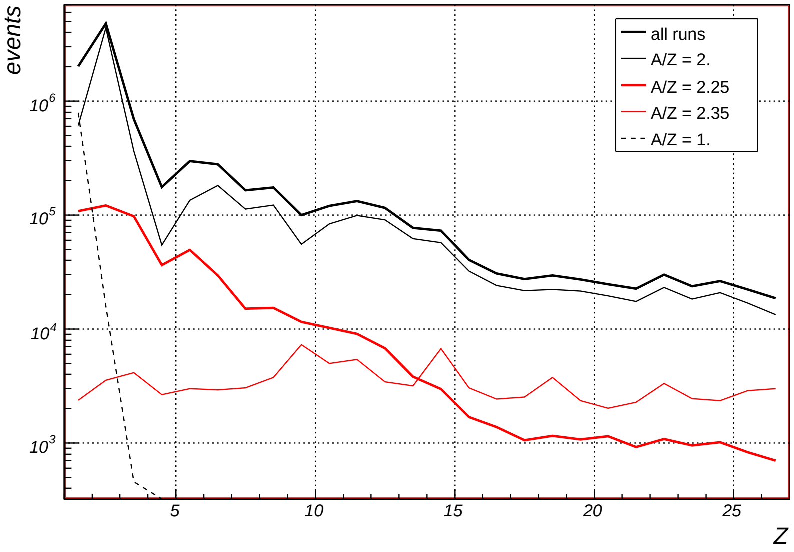

Figure 3.15: The statistic of the acquired data for the tracker telescope. A difference on the relative abundances between chemical species for the A/Z selections is achieved.

The beam test data were readout in *raw mode*, i.e. signals from all channels were recorded, with no online filtering applied. Out of spill events were used in the offline analysis to study the channel response in absence of physical signals. This allowed the evaluation of the algorithms for the computation of pedestals, common noise and strips noise in calibration and in the real events. The average noise levels in the test beam, were $\langle\sigma\rangle = 2.5(3.1)$ ADC counts on p (n) side, with a percentage of $< 1(5)\%$ of bad channels (figure 3.12).

Using a clusterization selection with a choice of $SN_{\text{seed}} \geq 3.7$ (3.8) for the p (n) side and $SN_{\text{neighbor}} \geq 1$ a good noise rejection with an high efficiency is allowed. In the upper plot of figure 3.16 is presented the number of strips depending on the incident particle charge. A saturation effect is recognizable. In the lower plot of figure 3.16 is presented the p-side and n-side cluster signal for the different charges of the ion beam test. A clear correlation is achieved.

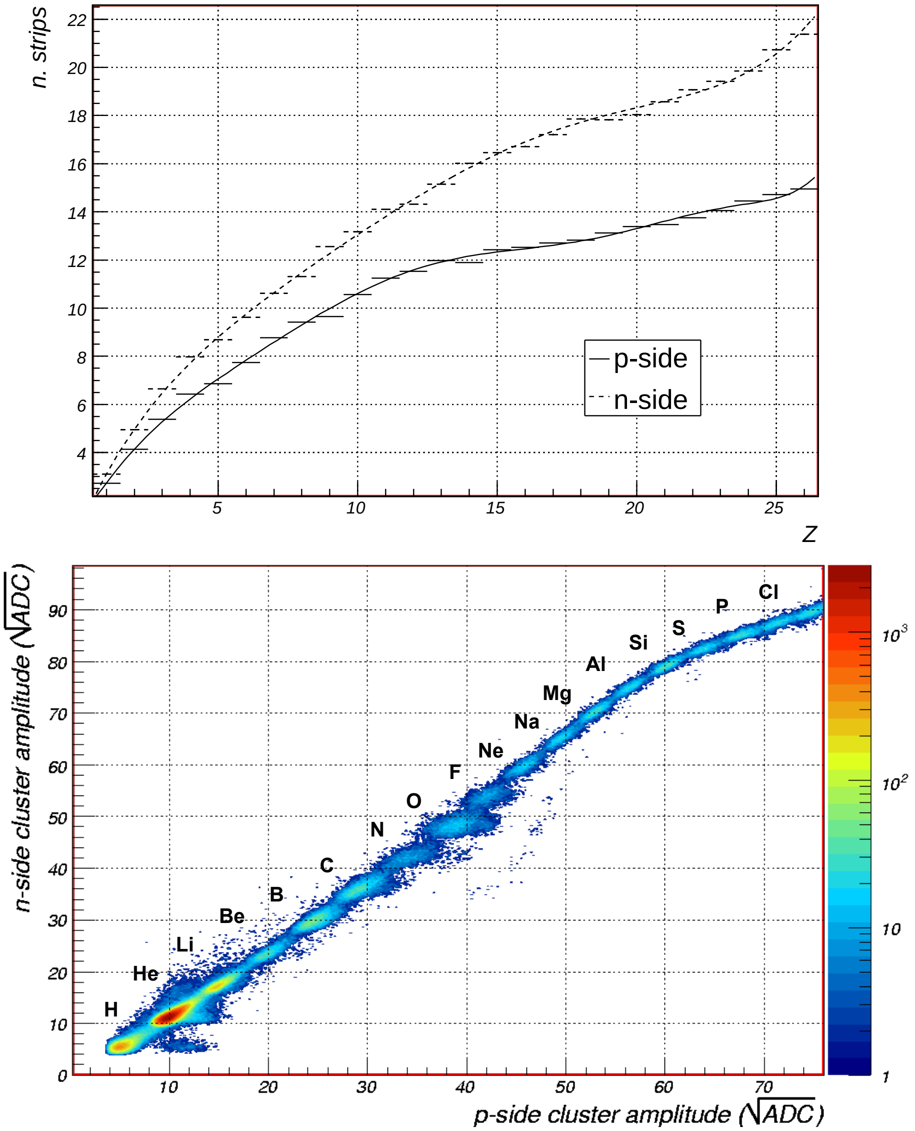

Figure 3.16: In the upper plot the cluster number of strips with respect to the measured particle charge. On the lower plot the charge distinction provided by two sides of the same ladder.

Chapter 4

Charge Reconstruction and Spatial Resolution Studies

Energy spectra measurements of different nuclear species in AMS will rely on the charge (Z) and the rigidity measurements performed by the Silicon Tracker. The large energy deposit of ions in the Silicon detector effectively alters the electric field distribution in the depletion region and it is difficult to render these kind of effects in a detailed simulation of the detector response. The 2003 beam test data have been then analyzed in order to study the detector response in terms of charge measurement and spatial resolution for ions. Results of these studies will be presented in this chapter, starting with a detailed description of the collected signal on both sensor sides for $3 < Z < 10$ ion species. Corrections for non-linear effects in the charge collection, its dependencies on the impact position and ladder-to-ladder gain differences will be then discussed. The charge selection algorithm and the expected tracker performances in the ion species identification will be then presented as well as the measured spatial resolution. Finally, the description of the 3D hit reconstruction by means of charge correlated p/n side signals will close this chapter, setting the basis for the fragmentation studies presented in the next one.

4.1 Cluster Studies

In the next sections the signal characterization, the charge reconstruction algorithm and the spatial resolution calculations for the high charge, i.e. $Z > 2$, generated cluster are presented.

4.1.1 High Charge Sample

For high charge clusters the signal-to-noise (SN) of each strip is much larger than proton/Helium cluster [1]. A choice of the signal-to-noise ratio parameters describing the clusterization procedure $SN_{\text{seed}} \geq 5$ and $SN_{\text{neighbor}} \geq 2$ allows a very good noise rejection with an high efficiency for high charges.

In order to select clusters corresponding to high charge particle crossing the ladder telescope the following criteria are applied:

- the presence of at least one cluster for each ladder/side is required;
- only the cluster with the highest amplitude for each ladder/side is considered (in case of multiple clusters);
- a χ^2 probability > 0.02 is requested for the two linear fit using the six cluster of the p and n side separately.

The initial statistic of $\sim$ 3.5M events for runs with $A/Z = 2.25$ and $A/Z = 2.35$ becomes $\sim$ 2M events when applying the clusterization procedure. Applying also the particle selection criteria $\sim$ 0.6 M high charge events are obtained.

4.1.2 Cluster Amplitude

The cluster *amplitude*, defined as the sum of the cluster strips signals ($\sum_i S_i$), is proportional to the energy loss of the traversing particle. Since the ionization energy loss is $\propto Z^2$, high signal levels and large strip multiplicities are expected in clusters with increasing charge of the incident particle.

Proton and helium signal characteristics have been previously studied [1]. An average of 2.24(2.05) strips and a most probable amplitude of 27.23(35.93) ADC counts have been observed for protons on the p(n) side respectively. Larger cluster widths and amplitudes have been measured on Helium p(n) clusters, with an average of 4.9(4.4) strips and a most probable amplitude of 123.3(167.9) ADC counts.

In figure 4.1 the number of strips in the cluster as a function of the particle Z is presented: a linear dependence of the cluster length on the charge $n_{\text{strips}} \simeq 3.19(1.22) + 0.70(0.89) \cdot Z$ well describes the experimental data on the p(n) side. Cluster amplitudes range from the 311 (677) ADC counts of the Beryllium clusters up to the 1142 (4484) ADC counts for Neon ones.

In spite of the increased cluster length, most of the signal (70(80)%) is shared over the two highest signal strips. Two typical cluster shapes, have been observed (figure 4.2):

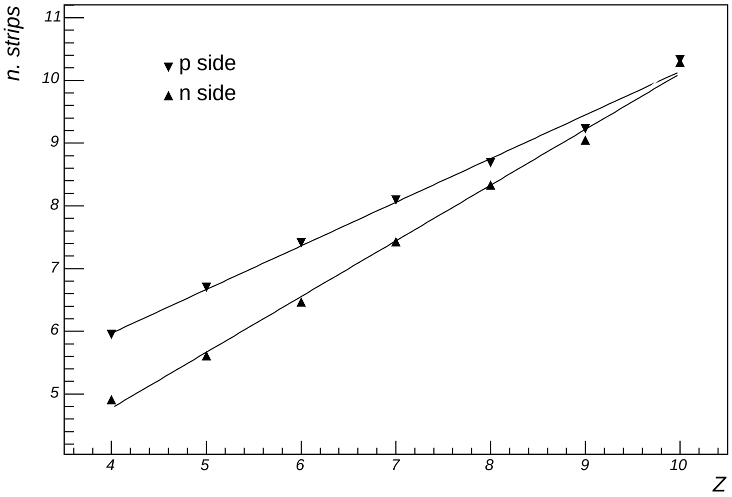

Figure 4.1: Average cluster strip number function of the particle charge Z for the p and n side. A linear fit is superimposed.

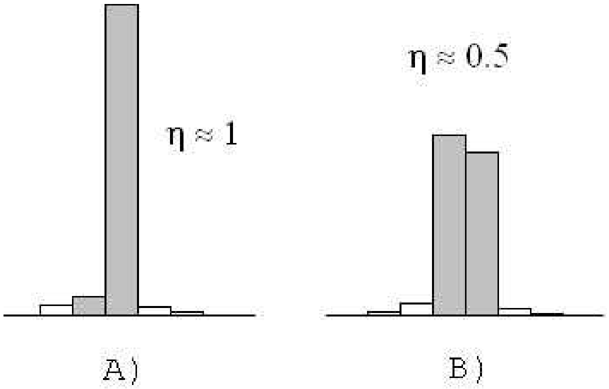

Figure 4.2: Qualitative representation of the most frequent cluster shapes: A) a particle passed very close to the readout strip, most of the cluster amplitude is collected on a single strip, B) the particle passed in between two readout strips, most of the cluster amplitude is shared on two strips.

a) the particle passed very close to a readout strip, most of the cluster amplitude is collected on a single strip, the *seed* of the cluster;

b) the particle passed in between two readout strips, most of the collected charge is shared between the two strips.

Moreover, the value of the cluster amplitude appears to be dependent on the cluster topology. For this reason, a detailed study of amplitude as a function of Impact Position (IP), the crossing point of the particle in the readout gap between the two highest strips, has been performed. The IP has been determined with the extrapolation from a five point linear fit excluding the ladder under study.

Different behaviors of the amplitude with respect to the particle IP have been observed for the two sensor sides and with increasing Z. In figure 3.7) the square root of the average cluster amplitudes for different ion species are reported as a function of the particle impact point. For a given ion species, a relative decrease of $\sim$ 20–30% is found in the collected signal on the p-side as the IP varies from 0.5 (particle passage in the central part of the readout gap, cluster shape B) to 0./1. (particle passing near a readout strip, cluster shape A). As a result of this dependency, a significative overlap of the signals from distinct ion species measured at different IPs is found. For instance, the average signal collected for a Boron particle at IP = 0.5 is indistinguishable from that of a Carbon at IP = 0.1 or Nitrogen at IP = 0.05. Moreover, even at a fixed IP value, large overlaps are seen in the signals from different chemical species (figure 4.15).

For this reason, the detailed study of the signal characteristics and the charge separation capabilities on the p-side have been performed only after a the complete charge reconstruction by means of the n side signal, as will be discussed in section 4.1.5.

Conversely, the n side amplitude has a reduced signal collection in the central region between readout strips (bottom plot of figure 3.7). A strong difference in the amplitude pattern occurs for the Neon ($Z = 10$) charge sample. This is due to the saturation of the n side strips, i.e. for Neon generated cluster the highest strip can saturate the dynamic range (4096 ADC counts) of the VA. For this reason only intermediate charges, from Beryllium to Neon, are considered in the following.

4.1.3 Charge Collection Characteristics: Side n

Due to the strips capacitive coupling, an approximation of the impact point of the particle can be derived from the cluster signal center of gravity (see

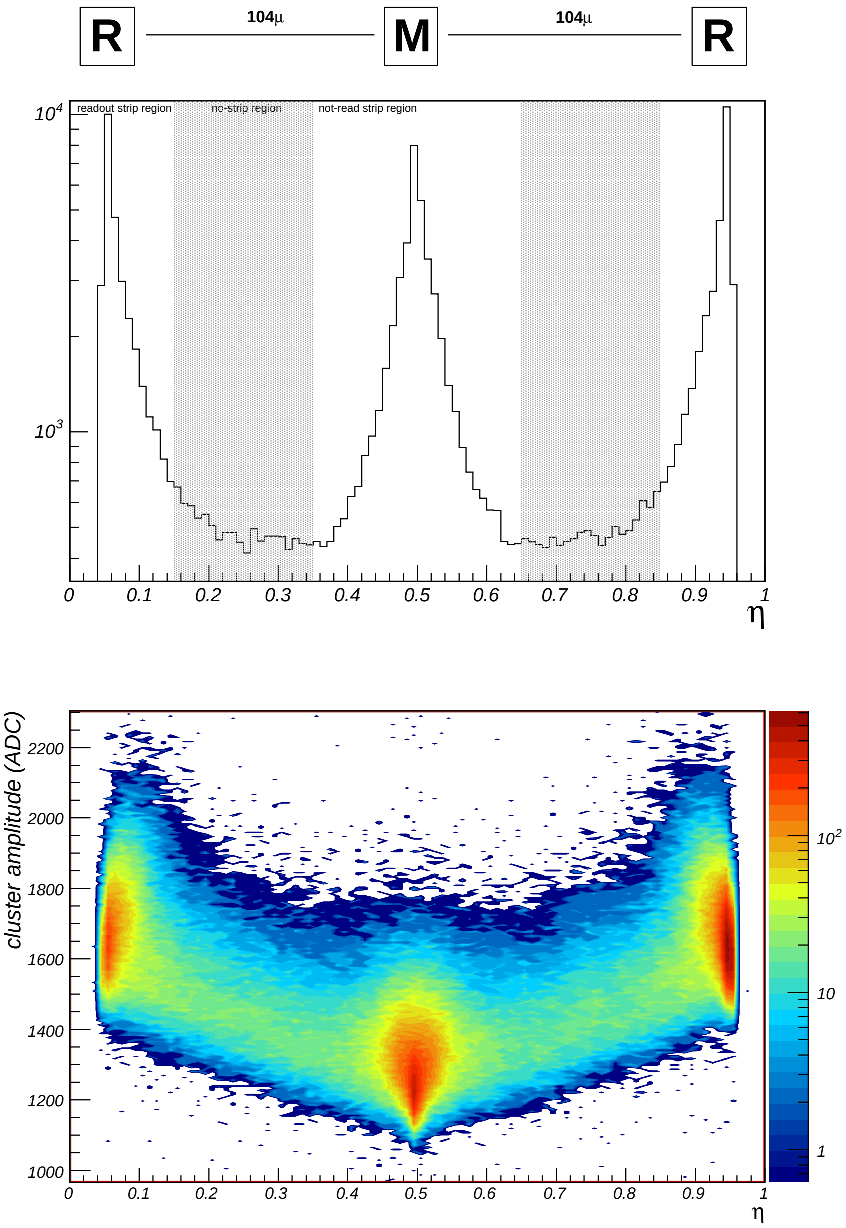

Figure 4.3: In the upper plot, under the strip implantation structure of the n side, the η distribution observed for Carbon ions in a ladder is presented. The different highlighted regions correspond to the three distinct η intervals in which has been separately developed the charge analysis: 1) read out strip region; 2) interstrip region; 3) not-read strip region. In the bottom plot, the cluster amplitude as a function of η is reported. The charge loss and the peaked η structure are here visible at the same time.

section 3.1.3). An estimate of this quantity is given by the η defined as:

$$\eta = \frac{Q_{\mathrm{R}}}{Q_{\mathrm{R}} + Q_{\mathrm{L}}} \qquad \eta \in [0,1]$$

where $Q_{\mathrm{L}}, Q_{\mathrm{R}}$ are the signals of the right (R) and left (L) highest strips in the cluster.

In the upper plot of figure 4.3 the η distribution measured on the n-side for Carbon ions ($Z = 6$) is presented. As a reference, the implantation pattern is reported just above of the η distribution: the correlation between the strip implantation structure and the peaks of the η is evident. Indeed, the n side performs a "quasi-digitized" measurement of position at a pitch of 104µm. A conservative estimate of the n-side spatial resolution is $d_{pitch}/\sqrt{12} \sim 30$µm (as resulted in section 3.1.3).

In the bottom of figure 4.3 cluster amplitude is plotted as function of η: the signal collection loss in the interstrip region and the η peaked distribution are observed here at the same time. The analysis of the signal amplitude in three different η intervals has been performed in order to improve the separation of different ion species. The η intervals have been selected according to the implantation/readout strip pattern:

- $\eta \leq 0.15$ or $\eta > 0.85$: readout strip region;
- $0.15 < \eta \leq 0.35$ or $0.65 < \eta \leq 0.85$: interstrip or no strip region;
- $0.35 < \eta \leq 0.65$: not read strip region.

In figure 4.4 the cluster amplitude distribution in different η intervals is presented for all selected clusters in a ladder. Peaks in the distribution correspond to the different energy losses experienced by the nuclear species present in the beam. It should be noticed, however, that the peak position, *i.e.* the collected signal, is shifted for the same species in different η intervals. In the readout strip region a saturation effect above the Neon charge is clearly present, as already pointed out.

An iterative procedure has been applied to study the characteristics of the signal amplitude for different ion species and η regions.

To obtain a relatively clean sample of events for a given ion species, only events releasing a signal on the sixth telescope ladder, taken as reference, in a restricted window around the energy loss peak for the ion under study were selected. This allowed to study the characteristics of its energy deposit on the other five ladders.

In order to estimate the probability, for a given amplitude, to be associated to the energy deposit of a given nuclear species, a probability density

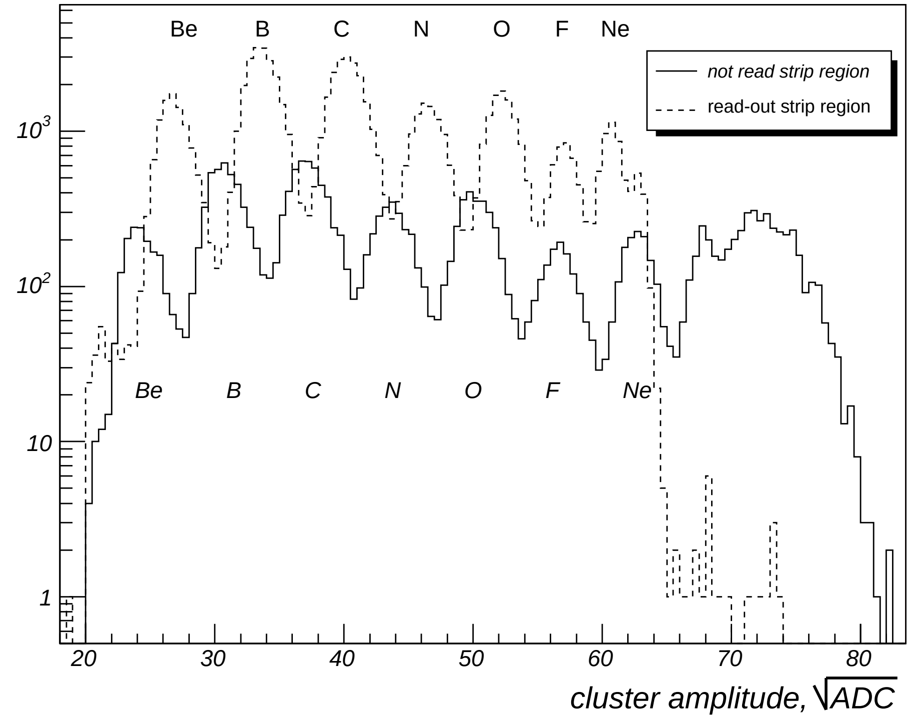

Figure 4.4: The charge amplitude of the n side sixth ladder for two different η region selection. The solid (dashed) line corresponds to the not read strip region (readout strip region), while the different peaks correspond to different ions.

function was constructed. A combined likelihood over five ladders, but the one under study, was then used to refine the event selection and obtain the final distributions of amplitude of all the telescope ladders in different η regions and for the ion species in the beam.

In figure 4.5 the amplitude distribution obtained on a ladder in the three η regions is shown for the Oxygen sample: the superimposed curves represent the fit result with the chosen signal parametrization. The bulk of the charge distribution is well described by a Landau distribution convoluted with a gaussian, as expected from the characteristics of the energy loss distribution of a particle traversing a thin material. An exponential function is empirically added for a better description of the tail. Denoting L the Landau function

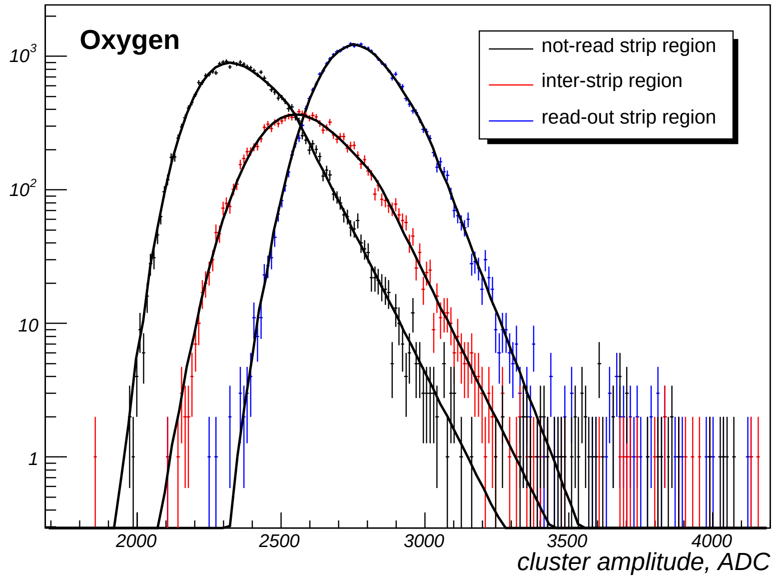

Figure 4.5: Amplitude distribution of the third ladder for an Oxygen likelihood selected sample. The different colors correspond to different η regions. The Gauss-Landau convoluted fit is superimposed.

and G the standard gaussian distribution:

$$f(x) = \begin{cases} x < x_{sep} & N \int_{-x}^{x} L(\tau; MPV, \epsilon) G\left(\frac{x-\tau}{\sigma}\right) \mathrm{d}\tau \\ x \geq x_{sep} & N_{LG} \cdot N_{rel} e^{-\lambda x} \end{cases}$$

This function is described by several parameters whose meaning is explained in table 4.1.

The same parametrization has been used to describe and fit the cluster amplitude distributions on all ladders, in each η interval and for ion charges from Be up to Ne. From a detailed analysis of the fit results, the following relevant features appeared:

- for a given Z and at a fixed η interval the widths of the Landau distribution (ϵ) and of the gaussian function (σ), as well as the slope parameter (λ) of the exponential tail do not significantly differ from one ladder to other;

- for a given Z and at fixed η interval the only difference between the parametrization of the six ladders seems to be a translation coefficient

parameter	**description**
x_{sep}	ADC value of separation between the Landau-Gauss convoluted distribution and the exponential tail.
N_{LG}	normalization of the Landau-Gauss distribution.
MPV	*most probable value* of the Landau distribution.
ϵ	width of the Landau distribution.
σ	width of the Gaussian distribution.
N_{rel}	relative normalization of the exponential function respect the Landau-Gauss normalization N_{LG}.
λ	slope of the exponential function.

Table 4.1: Description of the amplitude fitting function parameters.

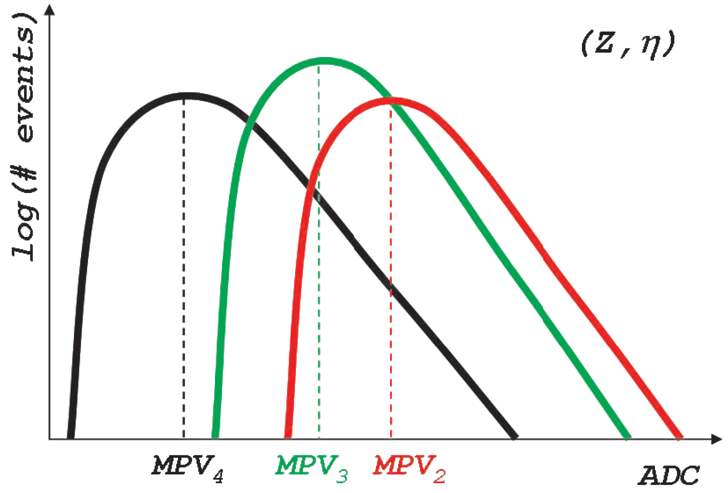

Figure 4.6: A representation of the amplitude distribution of different ladders for the same Z and η region. The signal shape is nearly the same, only the position of MPV is changing from one ladder to the others.

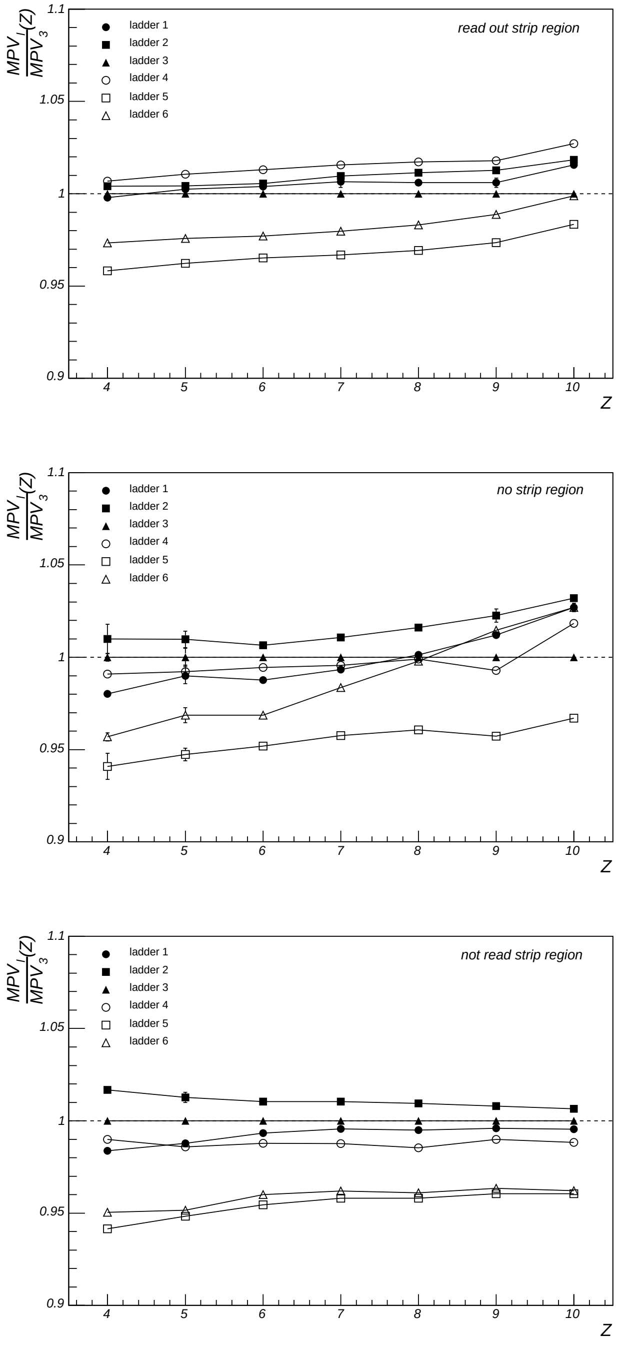

Figure 4.7: The relative translation coefficient $G_l(\eta, Z)$ for the different ladders function of the charge Z for each η region: from the top, a) readout strip region; b) no strip region; c) not read strip region.

of the MPV (figure 4.6). This can be defined, taking third ladder as reference, as:

$$G_l(\eta, Z) = \frac{MPV_l}{MPV_3}(\eta, Z);$$

- The trend of G_l in dependence from Z, for a fixed η, is quite flat (plots of figure 4.7), and its global scale of variation is of the order of percent. Therefore G_l can be reasonably considered independent from Z and η and can be identified as the *relative gain* of the ladder l.

These features allow for the description of the signal amplitude shape in a unique way for all the ladders. This description requires different parameters for all the Z and η possible values ($\epsilon_{Z\eta}$, $\sigma_{Z\eta}$ and $\lambda_{Z\eta}$). The only difference in the amplitude distribution from ladder to ladder is reduced to a gain correction independent from Z and η. Writing as $f(x; MPV, \epsilon, \sigma, \lambda)$ the fitting function the general representation of the signal can be summarized as follow:

$$f(x; MPV_{lZ\eta}, \epsilon_{lZ\eta}, \sigma_{lZ\eta}, \lambda_{lZ\eta}) = f(G_l \cdot x; G_l \cdot MPV_{3Z\eta}, \epsilon_{3Z\eta}, \sigma_{3Z\eta}, \lambda_{3Z\eta})$$

where l, Z and η are the integer indexing the six ladders, the seven charges and the three η regions.

4.1.4 Charge Reconstruction: Side n

The parametrization adopted to describe the signal amplitude for different charges has been used to build probability density functions:

$$P_Z(x; l, \eta) = \frac{f(G_l \cdot x; Z, \eta)}{\displaystyle\int_{-\infty}^{\infty} f(G_l \cdot x; Z, \eta)\mathrm{d}x}$$

a cluster with amplitude x has a probability value $P_Z(x)$ of being generated by a Z ion. The simplest criterion to assign a charge Z to the single cluster is to take the Z^* value for which the $P_{Z^*}(x)$ is maximum. In order to reconstruct the charge of a particle passing through n ladders is useful to define a *likelihood* function, combination of the P_Z of the different ladders:

$$L(Z) = \log \prod_{l=1}^{n} P_Z(x; l, \eta) = \sum_{l=1}^{n} \log P_Z(x; l, \eta)$$

A criterion for choosing the most probable charge of the particle passing through the ladders is to take the charge Z^* for which L is maximum,

$L(Z^*) = L_{\max}$. This *maximum likelihood* (ML) has the advantage of being an approximately unbiased and efficient charge estimation for a large number of events [76], but does not allow to define any parameter to tune the charge selection in order to achieve a given rejection power.

Conversely the *likelihood ratio* (LR) test is less efficient than the maximum likelihood, but can be ruled by a parameter, c, that can be used to control the rejection power. For example for two near charges the LR test can be built as:

$$\mathcal{L}(Z) = \frac{L(Z)}{L(Z) + L(Z-1)} > c \qquad c > 0.5$$

if $\mathcal{L}(Z) > c^*$, with $c^* > 0.5$, the Z charge is assigned to the particle. For $c^* < 0.5$, a biased charge evaluation towards $Z-1$ charges would be obtained. The LR test would reduce to the ML with $c^* = 0.5$ condition.

To discriminate charges in a sample where charges from Beryllium up to Neon are present, a global test has been conceived, based on a sequence of LR tests applied in turn on near charge pairs. Dividing the test in N_Z steps (number of charges under study), for each step, from the highest to the lowest charge, two condition are requested:

$$\begin{cases} \mathcal{L}(Z) > c_1 & c_1 > 0.5 \\ \mathcal{L}(Z+1) < c_2 & c_2 < 0.5 \end{cases}$$

the first condition is meant to separate Z from $Z-1$ charges, the second one is used to reject $Z+1$ charge.

To tune the c_1 and c_2 cuts, as well as to estimate the corresponding efficiency and rejection power, the likelihood function and likelihood ratios for different charges were studied on nearly pure Z samples.

These samples were selected by means of the energy deposits on the sixth ladder. In figure 4.8 the charge spectrum reconstructed on the sixth ladder is shown: the superimposed curves are the functions used to describe the signal distribution for different Z charges, their normalization is obtained by a combined fit to the spectrum. To obtain a nearly pure sample of events with a given Z, events with an energy deposit close to the corresponding amplitude peak were selected.

The sample purity, *i.e.* the relative contribution of different ion species to the events selected in a given energy range $[x_0, x_1]$ selected on the sixth ladder, was evaluated by means of the distribution function integral:

$$A_{\text{sample}}(Z) = \frac{\displaystyle\sum_{\eta} \int_{x_0}^{x_1} f(G_6 \cdot x; Z, \mu) \mathrm{d}x}{\displaystyle\sum_{\eta, Z} \int_{x_0}^{x_1} f(G_6 \cdot x; Z, \mu) \mathrm{d}x}$$

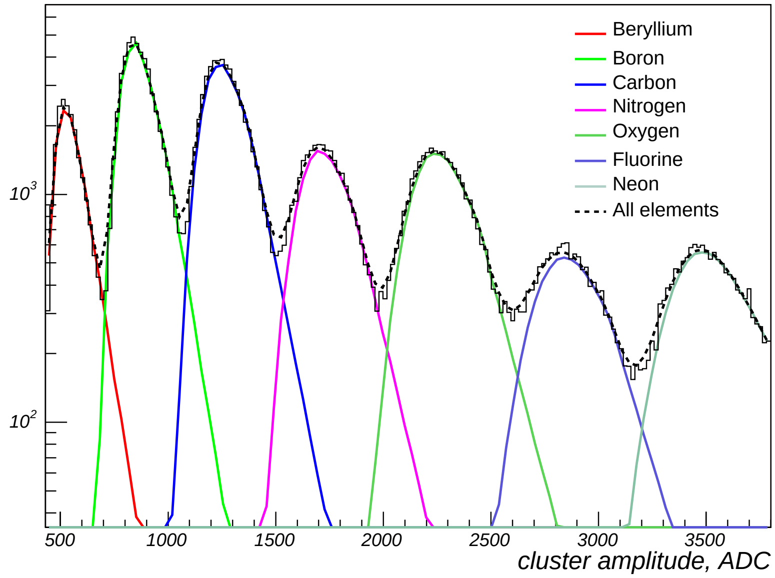

Figure 4.8: Sixth ladder charge spectrum for the not-read strip region. The amplitude distributions for the charges under analysis are superimposed in different colors. The sum of the different charge contribution to the spectrum is represented by the dashed line.

%	$A(Z-2)$	$A(Z-1)$	$A(Z)$	$A(Z+1)$
Be	—	—	100. ± 1.5	0.
B	—	0.85 ± 0.04	99.1 ± 1.0	0.
C	0.	1.22 ± 0.04	98.8 ± 1.0	0.020 ± 0.005
N	0.	2.3 ± 0.1	97.7 ± 1.4	0.022 ± 0.007
O	0.	1.46 ± 0.07	98.5 ± 1.3	0.023 ± 0.006
F	0.	2.9 ± 0.2	97. ± 2.	0.02 ± 0.01
Ne	0.02 ± 0.01	2.1 ± 0.1	98. ± 2.	—

Table 4.2: Abundances in percent of the chemical elements for the samples selected with the sixth ladder energy range criterion. The relevance of the $Z-1$ component is of the order of percent. The quoted zeroes are negligible abundances, while lines are the not computable abundances with the our definition.

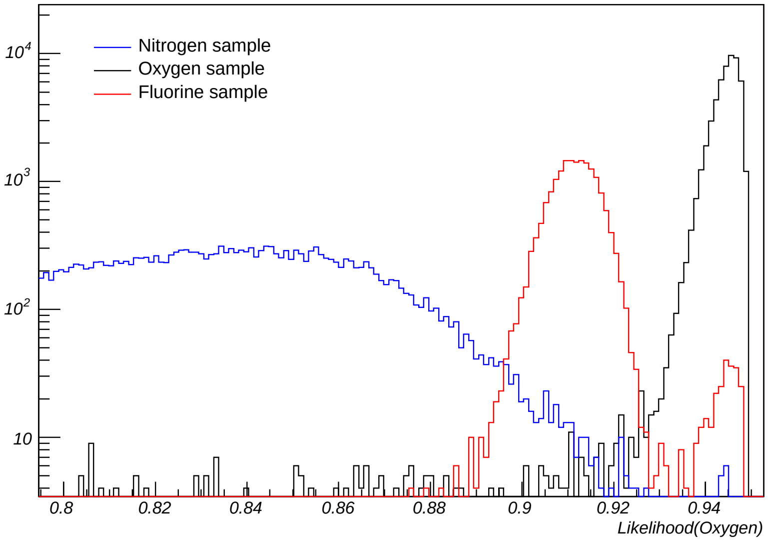

Figure 4.9: Is presented the Oxygen likelihood $L(Z = 8)$ for Nitrogen, Oxygen and Fluorine relatively pure samples selected with the sixth ladder amplitude ranges criterion.

this quantity indicates the number of expected events for a Z ion in the selected energy range. In table 4.2 the estimated compositions of the different samples are shown. For each ion species, the $A(Z)$ column represents the percentage of events whose charge has been correctly assigned. The other columns represent the percentage of contamination to the selected samples from $Z-2$, $Z-1$ and $Z+1$ ions. Purities of $97 \div 100\%$ are reached with this sample selection, the largest source of contamination for a given Z sample comes from $Z - 1$ charges.

Likelihood distributions $L(Z)$ for the different charges have been studied on these event samples. In figure 4.9 the Oxygen likelihood is presented when applied on different charge samples: Oxygen (Z), Fluorine $(Z+1)$ and Nitrogen $(Z - 1)$. As expected, the Oxygen likelihood is peaked towards large values in the corresponding charge sample, however a small peak is observed underneath the main Oxygen peak also when applying the Oxygen likelihood to the Fluorine sample. The size of this peak is compatible with the contamination of Oxygen events in the Fluorine sample ($\approx 3\%$ from table 4.2).

In figure 4.10, the LR test distributions relative to the Oxygen selection,

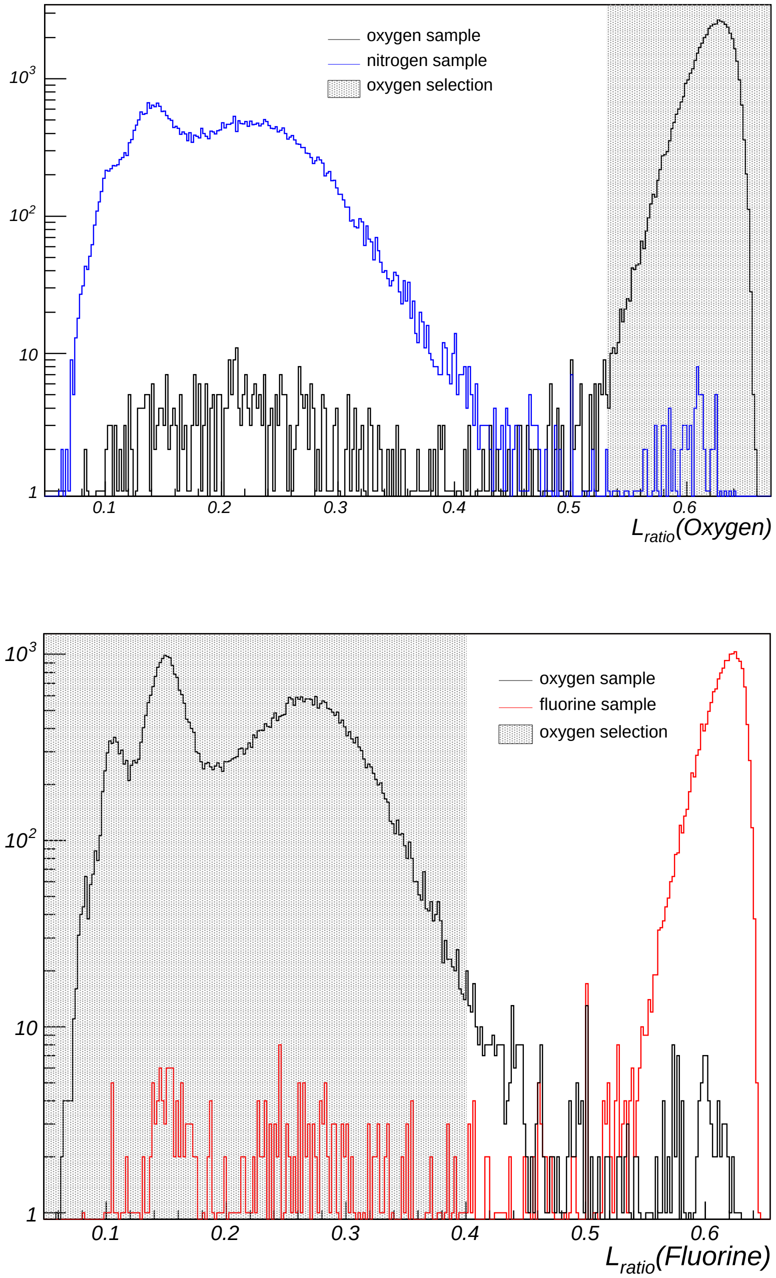

Figure 4.10: In the upper plot is presented Oxygen likelihood $\mathfrak{L}(Z)$ for Oxygen and Nitrogen samples, with a selection threshold of $c_1 > 0.53$. In the lower plot is presented Fluorine likelihood $\mathfrak{L}(Z+1)$ for Oxygen and Fluorine samples, with a selection threshold of $c_2 < 0.40$. The filled regions correspond to events reconstructed as Oxygen by the LR test.

$\mathcal{L}(Z = 8)$ and $\mathcal{L}(Z = 9)$, are presented for events belonging to the Oxygen, Nitrogen and Fluorine sample. In the uppermost plot, the $\mathcal{L}(Z = 8)$ function is applied to the Nitrogen and Oxygen samples. The shadowed area corresponds to the region where events are selected as Oxygen with a cut of $c_1 > 0.53$. The inefficiency of this selection is defined as the fraction of events in the Oxygen sample rejected with this cut. The contamination from Nitrogen events is defined as the fraction of events in the Nitrogen sample that is accepted with this cut. In the lowermost plot, the $\mathcal{L}(Z = 9)$ function is applied to Oxygen and Fluorine samples. The shadowed area corresponds to region where the events are selected as Oxygen with a cut of $c_2 < 0.40$. The inefficiency of this selection is defined as the fraction of events in the Oxygen sample rejected with this cut. The contamination from Fluorine events is defined as the fraction of events in the Fluorine sample accepted with this cut. The overall selection inefficiency can be obtained as the sum of the inefficiencies in the two tests.

In figure 4.11 the inefficiency and contamination of the $\mathcal{L}(Z = 9) < c_2$ is presented on the left as a function of the c_2 value. On the right, the inefficiency and contamination of the $\mathcal{L}(Z = 8) > c_1$ test is presented as a function of c_2.

In both tests, the inefficiency and contamination values obtained represent an upper limit to the real ones: the Oxygen, Nitrogen and Fluorine samples are not 100% pure (table 4.2) and part of the rejected events in the Oxygen sample could have well been Nitrogen or Fluorine, conversely part of the accepted events in the Nitrogen and Fluorine samples could have been really Oxygen events.

In table 4.3 the inefficiency and contamination values obtained for different charges are presented: for all ions values of $c_1 = 0.53$ and $c_2 = 0.40$ have been used.

High purity samples of different ions selected with the LR method on five ladders were used to estimate the charge selection efficiency on the single ladder with the likelihood method. In table 4.4 results are presented for the third ladder. In the table, each row corresponds to the particle charge assigned to the event with the LR method applied on 5 ladders. Each column refers to the charge value assigned with the maximum likelihood on the third ladder. A ~ 5 % inefficiency in selection at the single ladder level is found for all considered charges. As expected, for a given Z, the contamination level is higher from $Z - 1$ (3–4%) than from $Z + 1$ (~ 1%) charges.

%	Inefficiency	Contamination by $Z-1$	Contamination by $Z+1$
Be*	2.2 ± 0.1	—	0.76 ± 0.03
B*	1.39 ± 0.05	1.24 ± 0.05	1.02 ± 0.03
C*	1.70 ± 0.06	0.23 ± 0.02	1.52 ± 0.06
N*	2.3 ± 0.1	0.13 ± 0.01	0.88 ± 0.04
O*	1.81 ± 0.08	0.10 ± 0.02	1.7 ± 0.1
F*	3.2 ± 0.2	0.07 ± 0.01	1.27 ± 0.08
Ne*	1.67 ± 0.09	0.14 ± 0.03	—

Table 4.3: Inefficiency and contamination in % for the LR test with a choice of $c_1 = 0.53$ and $c_2 = 0.40$ for the different samples selected with the sixth ladder.

	Be	B	C	N	O	F
Be*	**0.952**	0.043	0.004	0.001		
B*	0.010	**0.962**	0.027	0.001		
C*		0.010	**0.962**	0.027	0.001	
N*			0.011	**0.959**	0.028	0.002
O*				0.015	**0.954**	0.029
F*					0.014	**0.945**

Table 4.4: Comparison of the single ladder charge selection result (columns) with the 5-ladder likelihood ratio ion selection (rows). Each row corresponds to the sample of a given ion species ($*$) selected by means of the 5-ladder likelihood ratio (Z_{LR}). For a given row, each cell reports the fraction of events identified by the single ladder as the ion species specified in the corresponding column (Z_{ML}). The values on the matrix diagonal correspond to the probability of correct charge identification with a single ladder (Z_{ML}), assuming that the Z_{LR} is a completely pure sample.

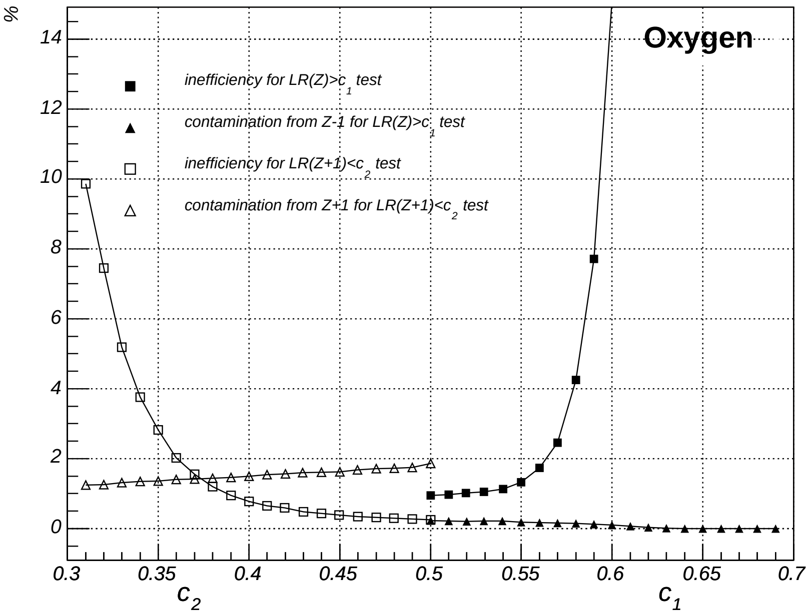

Figure 4.11: Inefficiency and contamination function of c_1 and c_2 threshold for the two condition of the LR test for an Oxygen sample. a) on the right Oxygen inefficiency and Nitrogen contamination for the $\mathcal{L}(Z) > c_1$ test function of $c_1 \geq 0.5$; b) on the left Oxygen inefficiency and Fluorine contamination for the $\mathcal{L}(Z+1) < c_2$ test function of $c_2 \leq 0.5$.

4.1.5 Charge Selection and Reconstruction: Side p

As already pointed out in section 4.1.2, charge collection on the p side exhibits a quite different features for $3 < Z < 11$ ions with respect to the n side. In particular the following behaviors are observed:

- cluster amplitudes for different ions are largely overlapping (upper plot of figure 3.7);
- the cluster amplitudes do not exhibit the expected linear dependence on the energy deposit ($\propto Z^2$) [77];
- the η distribution is squeezed in a restricted range of the interstrip region (dashed line of upper plot of figure 4.13) and does not reflect the implantation pattern of the p side strips;

- a charge dependent effect worsens the spatial resolution (dashed line of figure 4.14).

Under the hypothesis that all these distinct features are based on a common ground, we worked out a simple model to partially correct for these effects.

We made the hypothesis that a charge collection loss happens at the single strip level, the entity of the loss being related to the absolute charge value. In the ideal case, when a particle passes near a readout strip (A of figure 4.2) we would expect that the readout strip collects most of the released charge and the η value for that cluster would be close to 0(1). In presence of an anomalous charge loss, the readout strip - being the one with the highest signal amplitude - would be the most affected. This would not only decrease the total cluster amplitude but also reduce the "weight" of the readout strip in the η calculation, leading to a shift of the reconstructed η towards the center of the interstrip region. The η deformation will then result in a wrong assignment of the particle position.

Therefore, we have studied the charge collection at the single strip level. The signal collected on the highest strip in p clusters was analyzed as a function of the energy deposit in the ladder, estimated from the cluster amplitude reconstructed on the n side. Due to the dependence of the cluster amplitude on the particle impact point, i.e. on η, we restricted our study only to p(n) clusters within restricted η intervals close to the center (edge) of the interstrip region.

In figure 4.12 the average signal on the p seed strip is shown as a function of the average amplitude of the n side associated cluster. Signals from all ladders are contributing to this graph, the lack of uniformity in the signal amplitudes from different ladders being taken into account by means of relative gain corrections. The p signal dependence on the n cluster amplitude is clearly non-linear, and can be described with polynomial curve (superimposed as a dashed line). From the fitted behavior, two different correction functions f_{SC}, "hard" and "soft", have been built to scale the strip signal on the p side in order to restore a linear dependence (superimposed as solid and dotted lines).

For a given ladder l with a relative gain is G_l, the corrected strip signal is therefore defined as:

$$ADC_{corr,l} = G_l \cdot ADC^*_{corr} = f_{SC}(ADC^*) = f_{SC}\left(\frac{ADC_l}{G_l}\right)$$

where ADC^* is the gain corrected signal. It should be noted, that at charges higher than Neon, the saturation effect on the n side signal amplitude partially spoils the correction validity.

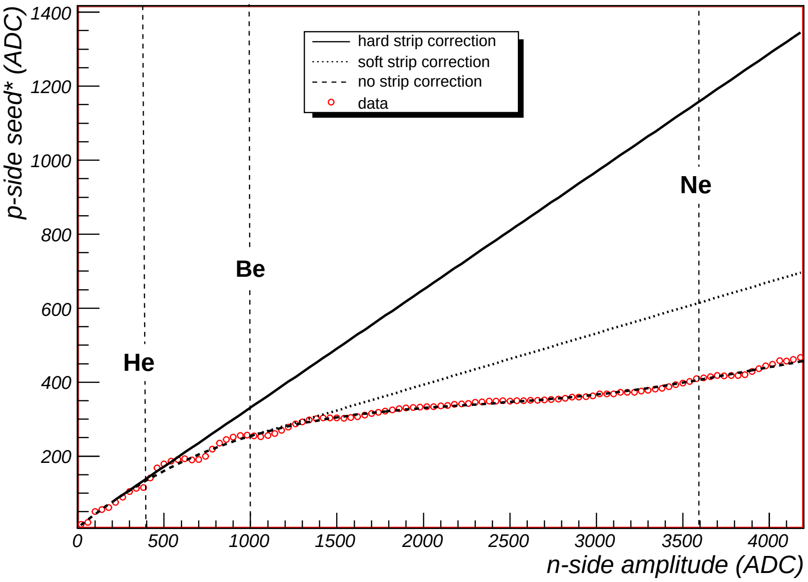

Figure 4.12: The signal collected on the highest strip (seed) in p clusters function of the energy deposit in the ladder, estimated from the cluster amplitude reconstructed on the n side. To reduce the signal dependence from position only signal in a restricted η interval are taken in account. Using relative gain corrections signals from all ladders are contributing to this graph. The behavior of data (red circles) is described by a polynomial curve (dashed line). Two linear correction, one "soft" (pointed line) and one "hard" (solid line), are superimposed.

The f_{SC} charge correction derived from the seed strip behavior has been then applied to all strips of the p side clusters.

In figure 4.13 (top) the effect of the strip correction on the η distribution is presented. A clear improvement is already visible with the "soft" correction. With the "hard" correction the peaks corresponding to the p side implantation structure are restored where expected. The overlapping between cluster amplitudes for different charges is largely reduced as well, as can be seen in figure 4.15 and in the bottom plot of figure 4.13 (respect to the upper plot of figure 3.7 in which no strip correction is applied).

A direct consequence of the corrected η distribution is an improvement of the spatial resolution. The single point resolution was evaluated for each ladder from the distribution of the residuals between the position measurement,

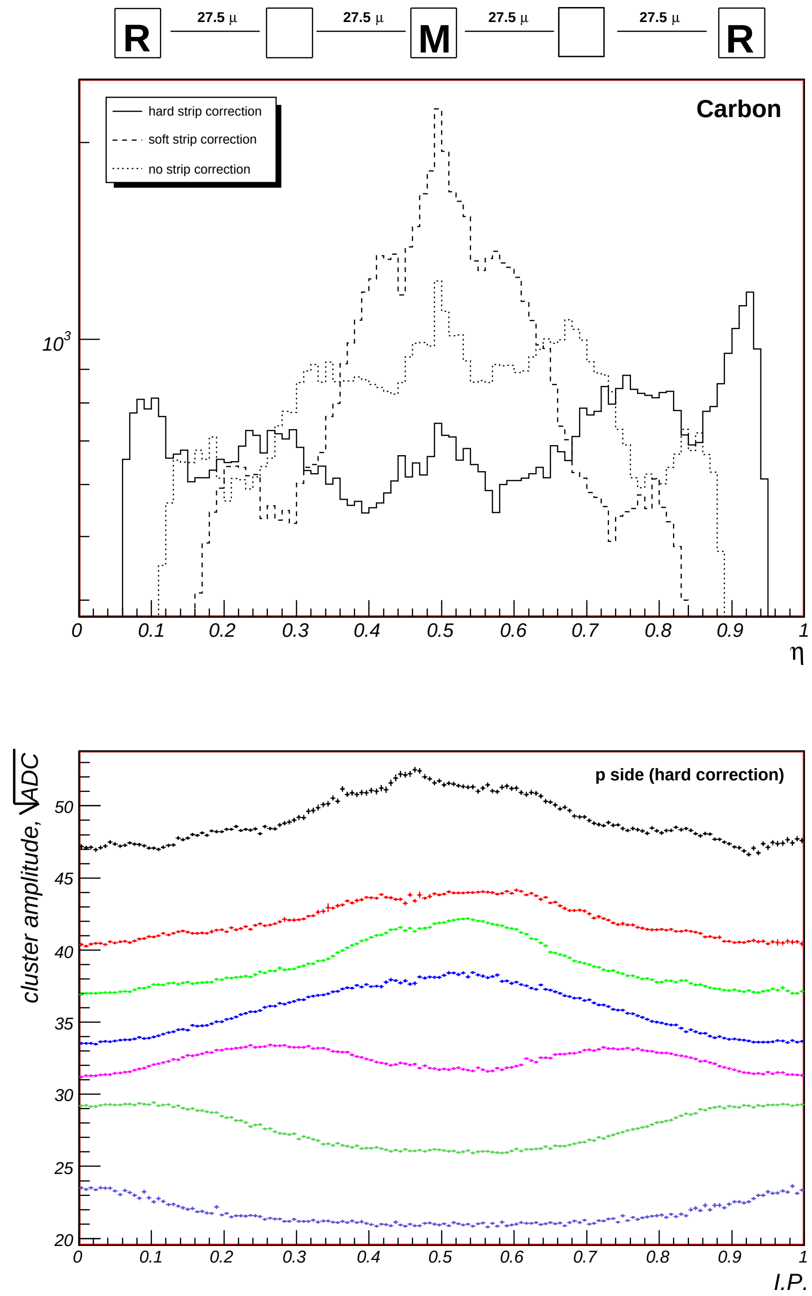

Figure 4.13: In the upper plot Carbon sample η distribution of the p side for the sixth ladder without strip correction (dashed line), with the soft strip correction (dotted line) and with the hard correction (solid line). On the top is presented the p side implantation structure. In the bottom plot the first ladder average cluster amplitude ($\sqrt{ADC}$) function of impact position (IP) for the hard correction is presented. From the bottom are presented the different charges: Be, B, C, N, O, F and Ne.

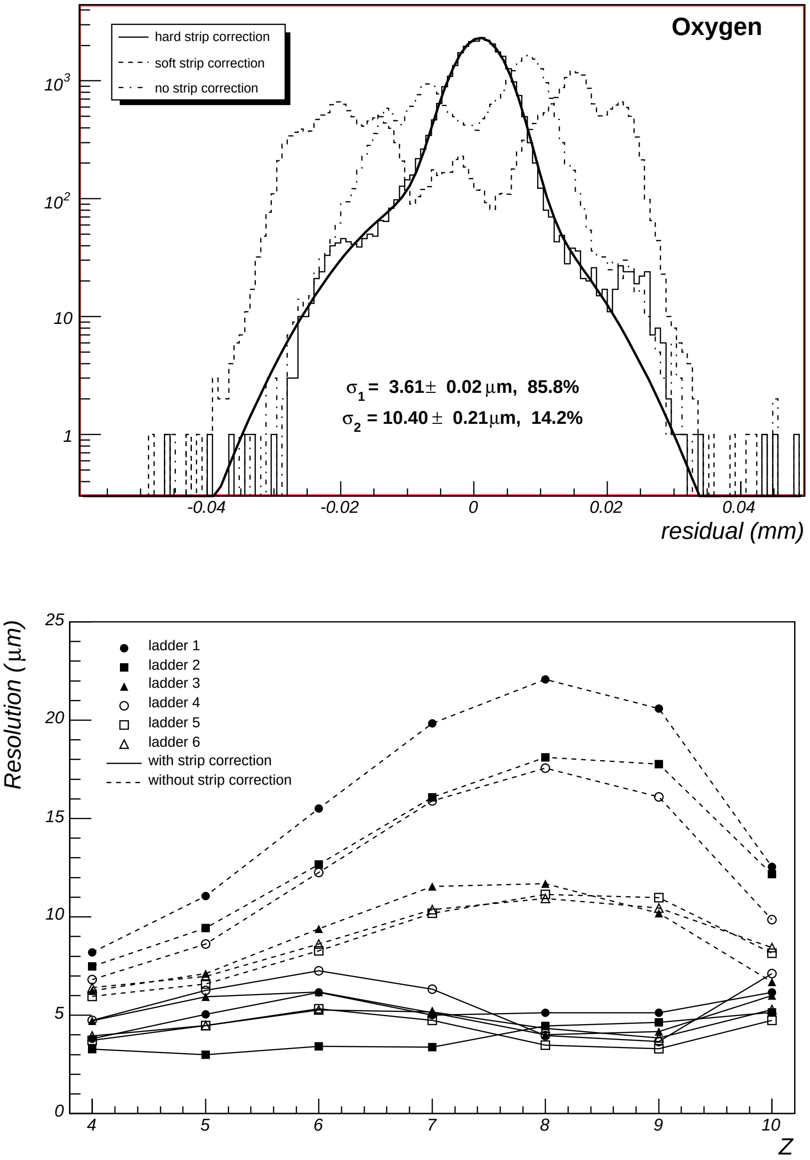

Figure 4.14: In the upper plot the residual resolution of the second ladder for Oxygen ions is presented. The dashed line corresponds to the residual distribution without correction, the dotted line to the soft corrected distribution and the solid line to the hard corrected distribution. The narrow distribution has the same double gaussian behavior of the residuals for Hydrogen and Helium [1]. In the bottom plot are presented the RMS (dashed line) of the not corrected distribution, and the spatial resolution of the hard corrected residual distributions (solid line), function of Z for all the ladders. A global resolution of ∼ 5µm is been achieved.

given by η, and the predicted impact position of the particle as evaluated from a fit to a straight line, using the position measurements of the remaining five ladder. Since the residual is defined as $\Delta x_{\text{residual}} = x_{\text{measured}} - x_{\text{fit}}$ the intrinsic resolution of the measurement, assuming Gaussian errors, can be defined as:

$$\sigma^2_{\text{intrinsic}} = \sigma^2_{\text{gaussian}} - \sigma^2_{\text{fit}}$$

where σ_{fit} can be estimated analytically from the straight line fit. In figure 4.14 is presented the residual distribution ($\Delta x_{\text{residual}}$) for uncorrected events and with corrections. The uncorrected distribution is clearly non-gaussian (dot-dashed line) and suffers of peaked structures. Soft correction partially improves the distribution width (dashed line). After the hard correction (solid line) the distribution can be described by the sum of two gaussian functions,with ~ 80 % of the data being accounted by the narrower one. The wider Gaussian reflects the cases in which, due to a noise fluctuation, the wrong strip has been associated to the seed in the cluster. σ_{gaussian} is evaluated as the weighted mean of the σs of the two gaussian functions.

In bottom plot of figure 4.14 the RMS of the original residual distribution and the spatial resolution ($\sigma_{\text{intrinsic}}$) obtained after corrections are presented for the different ladders as a function of Z. A twofold improvement is observed: the overall resolution is improved and presents only a weak dependence on Z for all ladders.

The applied corrections contribute to improve also the charge determination on the p side. The same procedure adopted to study the charge discrimination on the n side has been applied to build a likelihood test on the p side. We have selected high purity samples of events for different ion species by means of the n side likelihood ratio on all the six ladders. The cluster amplitudes on the p side for different ion species have been analyzed and described with a Landau convoluted with gaussian function (figure 4.15) in different η regions. Relative gains among ladders and their stability as a function of Z have been studied. In figure 4.16 the gain parameters, defined with respect to the fifth ladder, are shown in different η regions as a function of charge. As for the n side, the gain values are stable allowing for a unique description of the amplitude distribution for all the ladders.

The probability distribution has been defined for p side clusters and in table 4.5 the efficiency and contamination obtained with the maximum likelihood method on the single ladder are presented. As in table 4.4, each row represents the *true* value of the Z, which comes from the likelihood ratio test on the n side. Each column, corresponds to the Z assignment which maximizes the likelihood on the p-ladder. Similar efficiencies are obtained with respect to the single ladder test on n-side, but for $Z = 7, 8$.

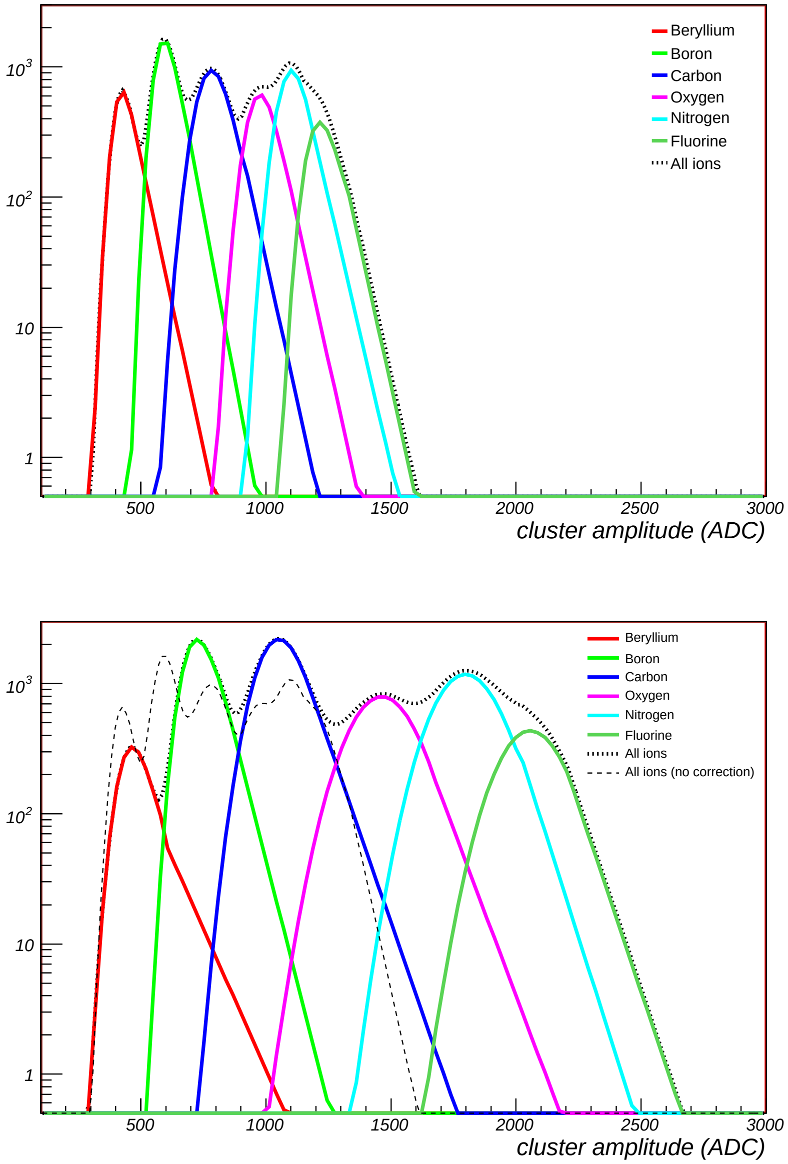

Figure 4.15: The p side cluster amplitude (for η in the central region) of the fifth ladder for the charges under study. The uncorrected amplitude is presented in the upper plot. While, on the bottom, is presented the cluster amplitude after the hard strip correction on the same ADC scale.

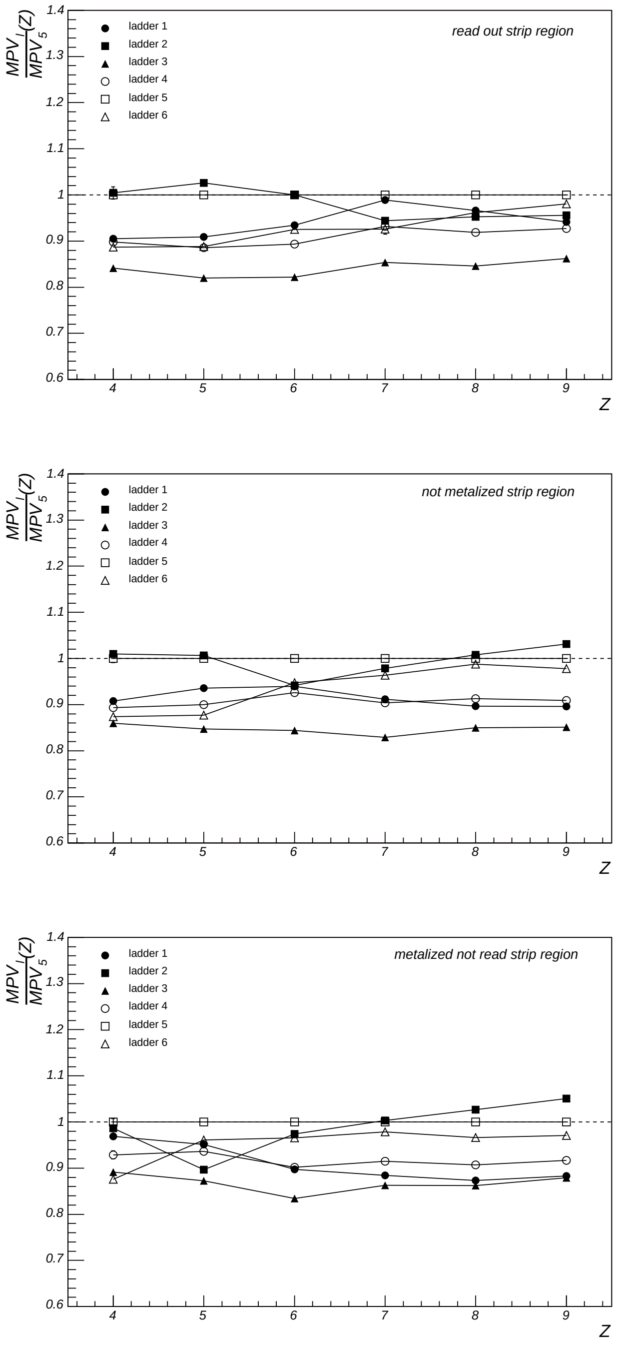

Figure 4.16: The relative translation coefficient $G_l(\eta, Z)$ for the different ladders function of the charge Z for the three η region: from the top, a) readout strip region; b) not metalized strip region; c) metalized and not read strip region.

	Be	B	C	N	O	F
Be*	**0.973**	0.024	0.003			
B*	0.007	**0.949**	0.042	0.001		
C*		0.021	**0.975**	0.003	0.001	
N*			0.159	**0.832**	0.007	0.002
O*			0.002	0.112	**0.880**	0.006
F*					0.085	**0.915**

Table 4.5: Each row corresponds to a charge sample selected by the n side ladders likelihood ratio criterion. Each column is the charge evaluated with the p side ladders maximum likelihood criterion. The shown numbers are the probability of reconstructing a Z_{ML} charge, determined with p side clusters, given the "real" charge Z_{LR} determined by n side ladders. As an example nitrogen is rightly reconstructed at $\sim 88\%$.

4.1.6 The Tracker Charge Separation Power

Using high purity charge samples, selected with the 5 ladder likelihood ratio test, an identification efficiency of $\sim$ 95 % at the single plane level was estimated (table 4.4). Conversely, due to the low purity selection based on a single ladder, only upper limits on inefficiencies and contaminations (of the order of %) could be determined for the charge identification with the combined 5 ladder measurement.

A toy Monte Carlo was developed in order to evaluate the charge identification capabilities of the full tracker, i.e. by means of the combined measurement of eight planes.

For a given chemical element, a high purity charge data sample was selected by means of the 5-planes LR. The cluster with the maximum amplitude on the remaining ladder is associated to the ion track and was used to model the simulated signal on a tracker plane. The cluster amplitude distribution as function of η obtained for different Z was taken as a reference for signal generation (figure 4.17). A three-dimensional hit-or-miss technique has been used in order to generate signals for a variable number of planes.

A statistics of $\sim 10^7$ five planes events was generated for each ion species and tested with the LR method applied to data. In figure 4.18 is shown the Carbon likelihood ratio for the simulated Carbon and Boron samples. A reconstruction efficiency of 99.6 % with contamination from $Z-1$ charges of the order of 10^{-4} (table 4.6) is obtained. Considering the relative abundances of charge samples selected with the sixth ladder criterion and using the achieved efficiency, the obtained inefficiency and contamination are in very good agreement with the measured ones. However the contaminations

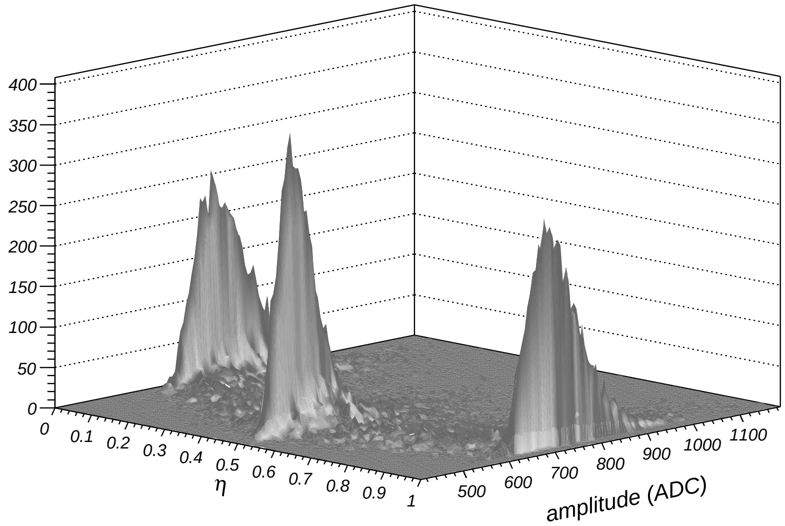

Figure 4.17: Cluster amplitude function of η for a Carbon sample selected with 5 planes charge likelihood test. This is used for the construction of a high purity Carbon simulated sample.

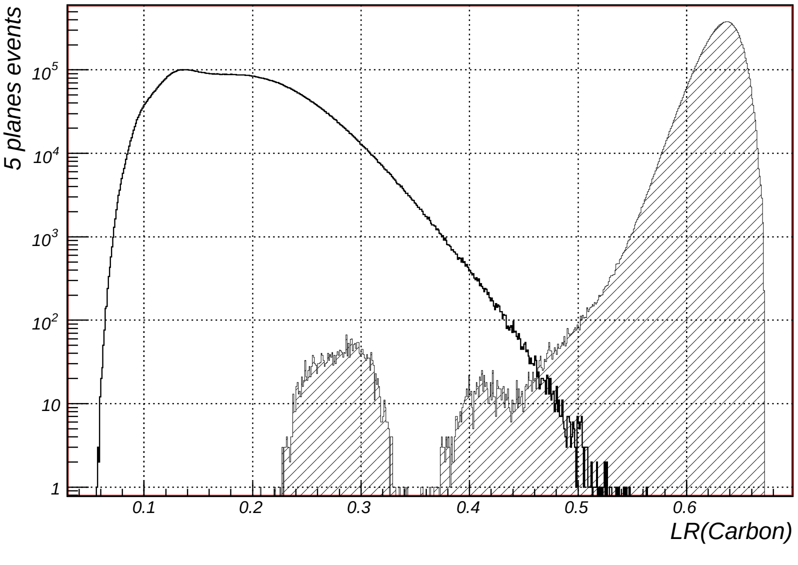

Figure 4.18: Carbon likelihood ratio for 10^7 particles of Carbon and Boron measured by five planes. A separation up to 10^{-4} is achieved.

sample (5 planes)	ϵ_{Z-1} (%)	ϵ_Z (%)	ϵ_{Z+1} (%)
Beryllium	0.0229 ± 0.0005	98.801 ± 0.001	0.00012 ± 0.00003
Boron	0.0052 ± 0.0002	99.886 ± 0.001	0.00006 ± 0.00002
Carbon	0.0189 ± 0.0004	99.791 ± 0.001	0.00006 ± 0.00002
Nitrogen	0.0363 ± 0.0006	99.654 ± 0.002	0.00013 ± 0.00004
Oxygen	0.0147 ± 0.0004	99.566 ± 0.002	0.00005 ± 0.00002
Fluorine	0.0155 ± 0.0004	99.403 ± 0.002	0.00013 ± 0.00004
sample (8 planes)	**ϵ_{Z-1} (%)**	**ϵ_Z (%)**	**ϵ_{Z+1} (%)**
Beryllium	0.0259 ± 0.0004	99.9221 ± 0.0007	0.
Boron	0.0070 ± 0.0002	99.9741 ± 0.0004	0.
Carbon	0.0302 ± 0.0005	99.9437 ± 0.0006	0.
Nitrogen	0.0493 ± 0.0006	99.9055 ± 0.0008	0.
Oxygen	0.0200 ± 0.0004	99.9310 ± 0.0007	0.
Fluorine	0.0147 ± 0.0003	99.9067 ± 0.0008	0.

Table 4.6: In the upper (lower) table are presented the efficiency ϵ_Z of reconstruction and the inefficiency of a wrong reconstruction ϵ_{Z-1}, ϵ_{Z+1} for a 5 (8) planes likelihood ratio tested on a 10^7 events Monte Carlo generated sample on 5 (8) planes. The contamination obtained in the two tables are of the same order ($\sim 10^{-4}$) indicating a probable non-purity of the distribution generating the simulated statistics.

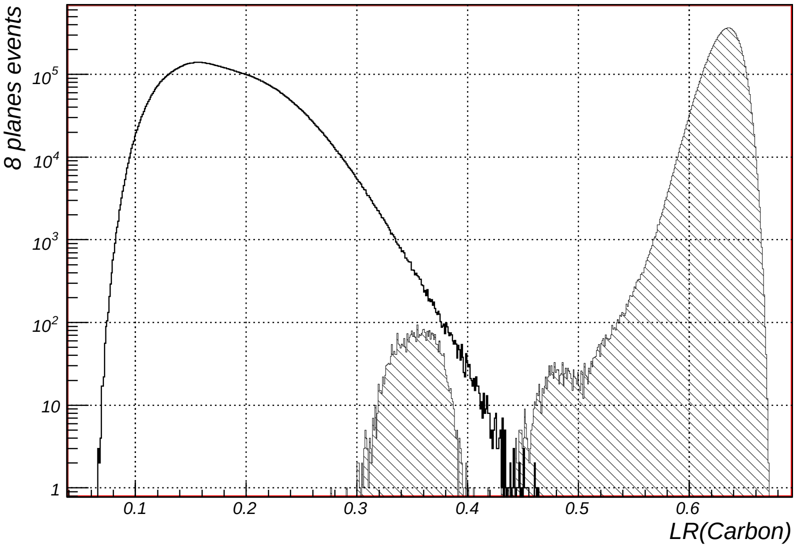

Figure 4.19: Carbon likelihood ratio for 10^7 particles of Carbon and Boron measured by eight planes. A separation up to 10^{-4} is achieved.

in table 4.6 are upper limits of the real contaminations due to the presence of non-purities of the 5-planes selected generation sample.

The projection for the full discrimination power of the AMS-02 Tracker can be obtained simulating 8 planes. The eight planes Carbon likelihood ratio for 10^7 particles of Carbon and Boron is presented in figure 4.19. The obtained contamination are of the same order 10^{-4} of the 5 planes evaluation (table 4.6), indicating probable impurities of the distribution generating the simulated statistics. Considering the contaminating distribution peak under the Boron sample in figure 4.19 as a the original sample non-purity a rejection of 10^{-7}, i.e. a total rejection, can be quoted for the discrimination between chemical species.

4.2 Hit studies

The drift of electrons/holes pairs produced by ionization in the sensor depleted region induces signal on the p^+ and n^+ side strips resulting in correlated amplitudes for the corresponding p/n clusters. Then, a signal-based p/n pairs association allow the construction of *hits*, i.e. 3D points with an unique charge evaluation.

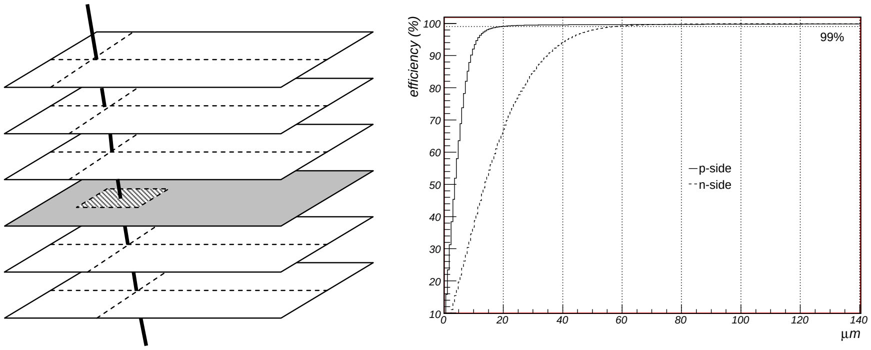

Figure 4.20: On the left a schematic view of the geometric selection procedure. A track of 5 points, with a good χ^2 linear fit and a good 5 planes charge likelihood, defines the particle direction and charge. On the last ladder a geometric cut around the track selects the p/n cluster pair associated to the incident particle. On the right is presented the efficiency of the geometric cut. For an efficiency of 99 % spatial cuts of 60 (20) µm around the track for the x (y) coordinate results.

In the next sections the construction and testing of an amplitude-based an p/n clusters association algorithm is developed.

4.2.1 p/n Clusters Charge Correlation

As a first step in defining 3D hits, the p/n signal correlation characteristics were studied. For a given ladder, p/n cluster pairs were selected on the basis of their proximity to the particle incident position as evaluated from the track defined on the remaining planes (figure 4.20 left). Requirements imposed in this selection were:

- track definition:
    - track was built out of the maximum amplitude clusters on the p/n side on 5 planes, excluding the one under analysis;
    - a tight cut ($L > 0.80$) on the n-side amplitude charge likelihood of the five planes was requested in order to assign the event charge with the likelihood ratio test;
    - a 5 hit track, defined as χ^2 probabilities in the two projection greater than a 0.02 ($P_{\chi^2} > 0.02$) were used to estimate the impact point on the ladder under study;

- p/n clusters selection:
  - only clusters reconstructed within 20 (60) µm from the predicted track incident position were considered in the p(n) sides. This request was loose enough to get a selection efficiency of 99 % on both sides (figure 4.20, right);
  - only clusters with a charge Z, as estimated by the maximum likelihood, similar ($|\Delta Z| \leq 2$) to the event charge were considered.

In order to compare the p and n clusters signals on an unique amplitude scale different corrections were applied to the raw signals.

A *gain normalization* was first applied in order to get an uniform response from different ladders (figure 4.7 and 4.16).

Then, an *equalization for the charge collection* dependence on η was applied. The equalization has been realized correcting the MPV of the cluster amplitudes in the middle and central η regions to the MPV measured in the readout region. The ratios of the MPVs in the central/middle η intervals to the reference MPV are presented as a function of Z in figure 4.21. A linear dependence of the equalization factors on the signal amplitude was found in the n-side, corresponding to an effective decreasing of the collection efficiency in the central/middle η regions. A non-linear behavior is observed on the p-side, corresponding to the non linearities in the CNO p-side signal discussed beforehand. The superimposed polynomial effective fits were used for the equalization.

Finally, a *side normalization* of the n-side MPV scale with respect to the p-side MPV values was imposed. The effective fit used to evaluate this correction is presented in figure 4.22.

Considering S_p and S_n as the normalized amplitudes for p and n sides clusters the correlation parameter C_{pn} is defined as:

$$C_{pn} = \frac{S_p - S_n}{S_p + S_n} \qquad C_{pn} \in [-1, 1]$$

The dependence of this parameter upon the particle charge is presented in figure 4.23 where an effective double gaussian fit is superimposed. While the gaussian distributions means μ_1 and μ_2 are nearly $\mu_1 = \mu_2 \sim 0$, the $\sigma_1(Z)$ and $\sigma_2(Z)$ depend from Z and are of the order of 10^{-2}–10^{-1}.

Based on the effective fit of the correlation distributions an association probability for a given p/n pair is defined. For a given p/n combination, the hit charge Z_n is assumed from the maximum likelihood estimate on the n cluster. Then association probability P_{pn} for a correlation C_{pn} and $\sigma_1(Z_n)$,

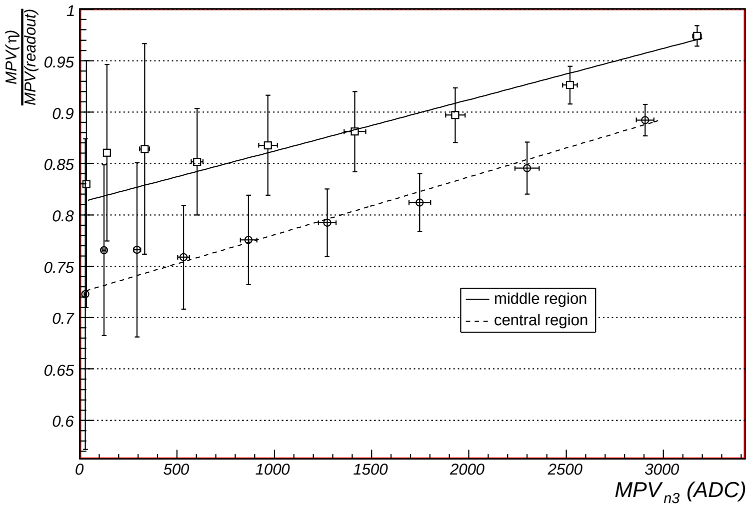

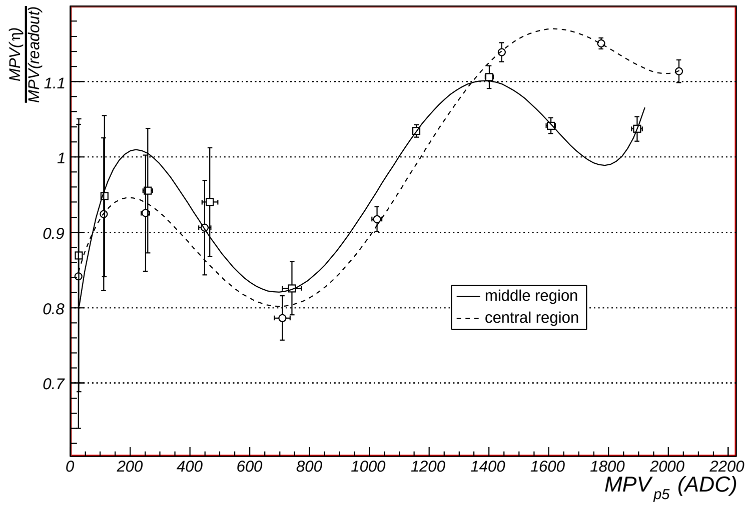

Figure 4.21: The MPV amplitude for two different η region (middle and central) with respect to the MPV of the readout region for the reference n (upper plot) and p (lower plot) sides. While the charge collection on the n-side has a linear variation the p-side has a strong non linear effect in the CNO amplitude range. Effective polynomial fits are superimposed.

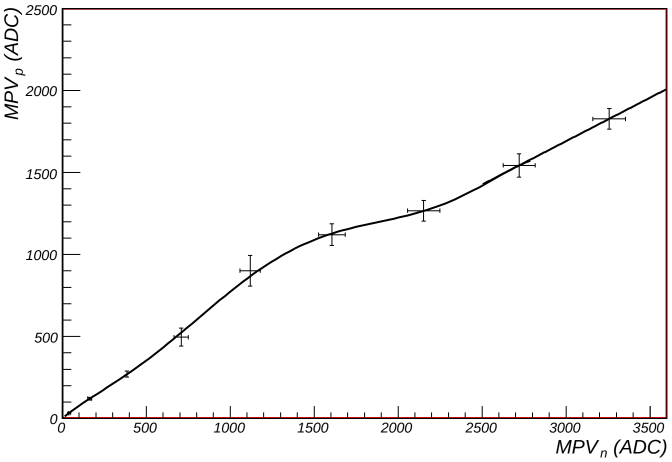

Figure 4.22: The MPV p-side readout amplitude with respect to the corresponding MPV n-side readout amplitude. An effective polynomial fit is superimposed.

$\sigma_2(Z_n)$ is then defined as:

$$P_{pn} = \frac{1}{A_1 + A_2}\left(\frac{A_1}{\sqrt{2\pi}\sigma_1}\exp -\frac{C_{pn}^2}{2\sigma_1^2} + \frac{A_2}{\sqrt{2\pi}\sigma_2}\exp -\frac{C_{pn}^2}{2\sigma_2^2}\right)$$

In figure 4.24 the association probability distribution is presented in $Z = 6$ events for two distinct p/n cluster pair samples. Dashed red line refers to all the possible p/n cluster pairs combinations. Black solid line refers to the subsample where p/n cluster pairs were geometrically selected by their proximity to the fitted 5-point track. The bulk of the wrong 3D hit assignments are observed at probabilities < 0.032 with a sharp peak ~ 0.

4.2.2 Hit Reconstruction Algorithm and Efficiency

For a given number of N$_p$/N$_n$ clusters reconstructed on the p/n side of a ladder, $N_p \times N_n$ pairings can be attempted to build a 3D hit. In the upper plot of figure 4.25 the p cluster amplitudes versus the n cluster amplitudes of the N$_p$×N$_n$ possible p-n combinations is presented. Correct combinations (N$_H$ = min(N$_p$,N$_n$)) will correspond to the entries along the bisector.

An iterative procedure, based on the charge association probability, was developed to discriminate the true 3D hits from the combinatorial background:

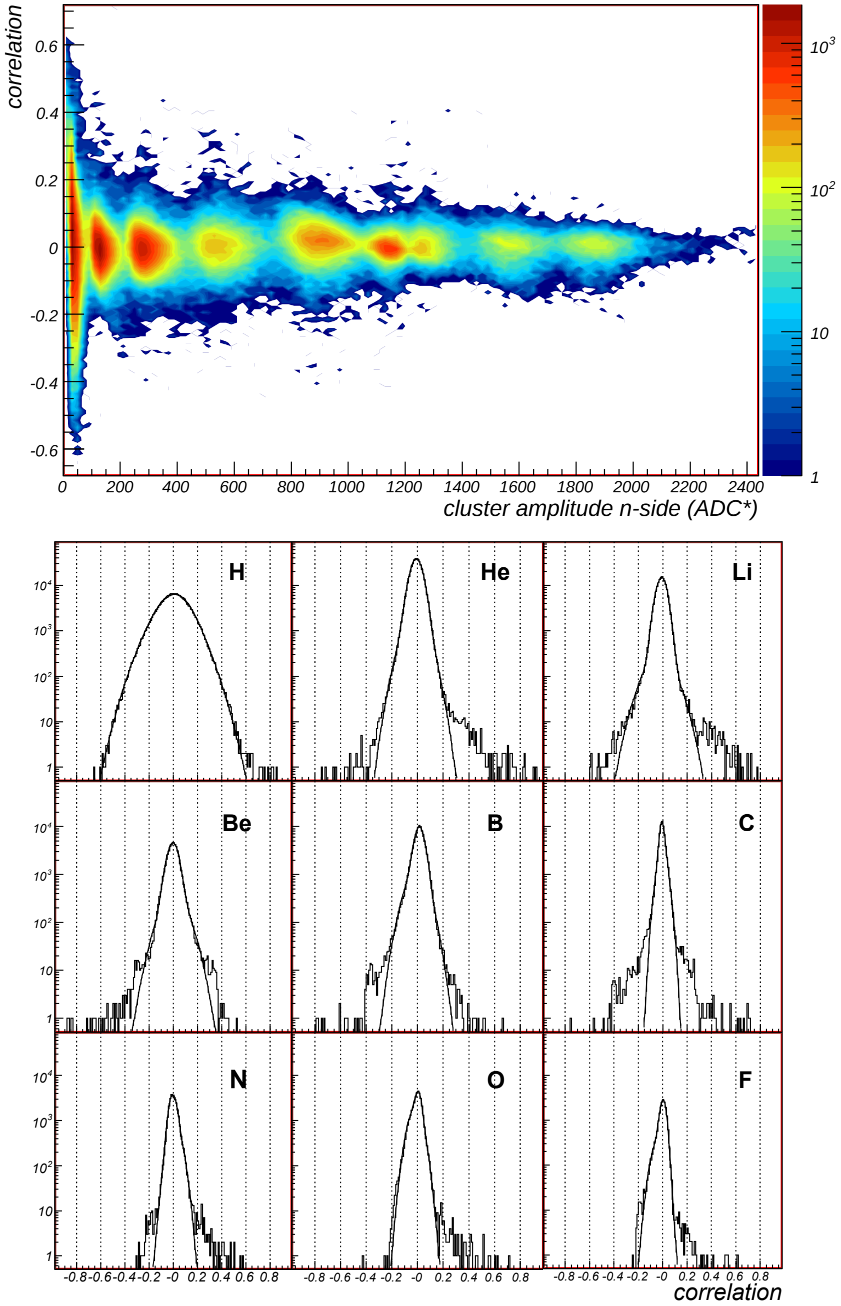

Figure 4.23: In the upper plot the correlation distributions for the geometric selected cluster couples of all ladders with respect to n-side cluster amplitude. In the lower figure the projected correlation distributions for charges selected with the n-side maximum likelihood method. Double gaussian fit are superimposed in order to give an effective description of the correlation behavior.

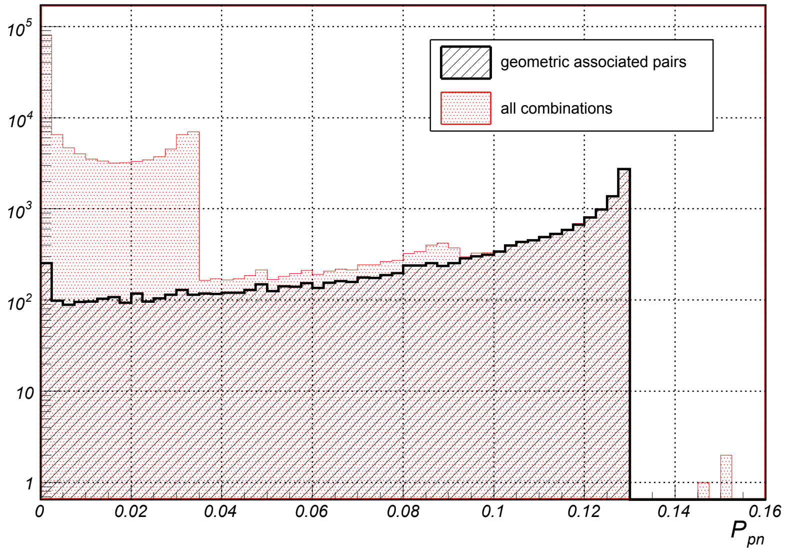

Figure 4.24: The probability of association of $Z = 6$ tracks for geometric selected pairs and for a sample of cluster couples without selection (all combinations, correlated and uncorrelated, are present).

1. charge association probabilities are calculated for all the $N_p \times N_n$ p/n pairs and sorted in decreasing value;
2. the most probable pair is "freezed" as a hit, deleting from the list all the combinations involving either of the p/n selected clusters;
3. previous step is repeated, freezing the following most probable hit and so on until all combination have been exhausted.

The maximum number of hits produced with this algorithm is just N_H, the corresponding p-side versus n-side cluster amplitudes are presented in the lower plot of figure 4.25.

The overall hit reconstruction efficiency will depend both on the single cluster reconstruction efficiency and on the association algorithm. In fact, the wrong association of a spurious noise cluster on one ladder side with a signal cluster on the opposite side will create a fake hit, possibly leaving an "orphan" good cluster.

In figure 4.26, solid lines, the overall hit reconstruction inefficiency as a function of Z is presented for the central ladders (3,4) of the beam telescope. The inefficiency is quoted as the fraction of events where no hit of the correct

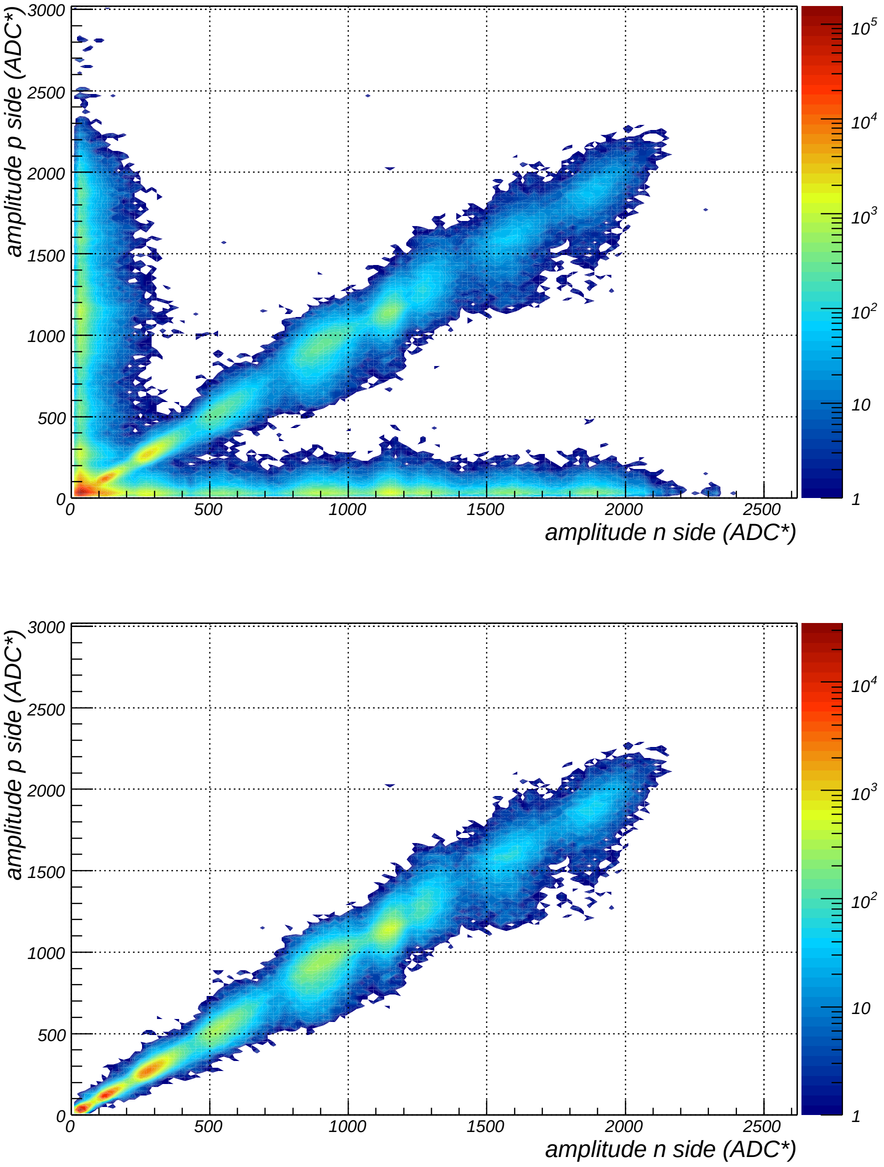

Figure 4.25: Couples of p-side and n-side cluster normalized amplitudes for: (a) all the possible p/n couples combinations on a plane ($N_p \times N_n$), (b) the couples selected with the hit reconstruction algorithm ($min(N_p, N_n)$).

charge was found on the ladder under test in a 20(60)µm window on the p(n) side around the predicted track impact position. The higher inefficiency

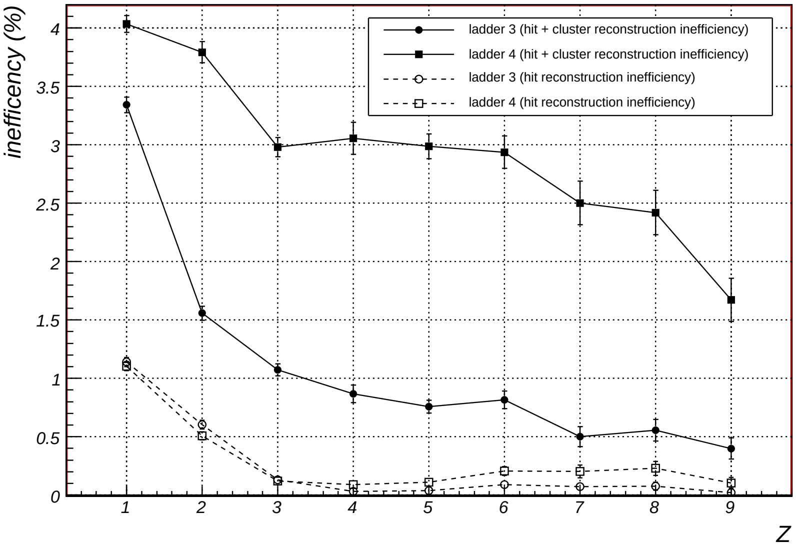

Figure 4.26: Hit reconstruction inefficiency as a function of Z.

observed on the 4-th ladder is due to the presence of a dead strip in the beam illuminated region.

In order to disentangle the association algorithm contribution from the overall hit reconstruction inefficiency, an event sample where clusters could be independently associated on the p/n side to the extrapolated track was selected. This selection effectively removed events where no hit could be reconstructed due to detector inefficiencies or an incorrect prediction of the track impact point. The hit reconstruction algorithm inefficiency is then quoted as the fraction of events in this selected sample where no 3D hit was reconstructed close to the track. In figure 4.26, dashed lines, the hit reconstruction algorithm inefficiency as a function of Z. The two ladder response is now similar, and a typical value of ~ 0.1 % is found slightly dependent from the specific Z.

Chapter 5

Fragmentation studies

A detailed description of nuclear interactions in the active and passive AMS detector material is fundamental to design an efficient trigger for GCRN and to have an estimation of the detector acceptance in the measurement of the differential nuclear fluxes. Furthermore, nuclear interactions can also affect the track reconstruction and spoil the sensitivity to nuclear anti-matter searches.

The ion beam test data give the opportunity to study the ion interactions with the AMS-02 tracker elements (ladders). In this chapter we first focus on the selection of the fragmentation events observed in the beam test data. We then introduce the FLUKA simulation code, which has been used to reproduce the test beam setup and to study the typical topologies of the inelastic collisions in the Silicon Tracker.

The substantial agreement between simulated and experimental data is then presented, suggesting the possibility to implement a ion-focused FLUKA-based Monte Carlo simulation for the AMS-02 instrument.

5.1 Fragmentation in Real Data

Ion beam test events, after the charge identification and hit reconstruction steps described in chapter 3, have been used to study the nuclear fragmentation probability in the ladders at intermediate charges, being the collected statistics with $Z > 10$ too low.

Nuclear fragmentation is expected to concern just a small fraction, O(‰), of the events: in order to perform such a study the pre-selection of a clean event sample is mandatory in order to reject events where nuclear interactions occurred before the telescope, either in air or in the materials placed on the beam line (figure 3.14), as well as to discard beam events with multiple ion

sample	events	selected
Lithium	424733	17366
Beryllium	115155	5125
Boron	251528	10746
Carbon	240097	13447
Nitrogen	123460	7067
Oxygen	141239	7227
Fluorine	56746	3254

Table 5.1: Sample pre-selection statistics for the different ion species. First column reports the number of selected events requiring an isolated ion track in the *upstream* telescope (noisy, high backscattering and double tracks events are rejected). The selected number of *non-straight* events, resulting from the further requirements applied on the track reconstruction in the full telescope, is presented in the second column.

fragments impinging on the Si telescope.

The first two ladders are then used as an *upstream* telescope to define the incident ion direction and charge for the fragmentation analysis applied on the remaining *downstream* 4-ladder telescope.

The selection criteria applied in the upstream telescope are:

a. in each ladder one and only one hit with $Z \geq 3$ must be reconstructed. The p/n charge association probability for the hit should exceed a minimum threshold $P_{pn} > 10^{-4}$;

b. a consistent charge assignment, within a $\Delta Z \leq 2$ interval, is required on the two selected hits;

c. the ion track as reconstructed in the upstream telescope should be consistent with the average beam direction within its divergence ($\sim$ 0.5 mrad);

d. the presence of a maximum number of five hits with $Z = 1, 2$ is allowed in either of the two ladders;

e. one and only one cluster of charge greater than one on each side/ladder;

The first three conditions identify the presence of a single ion track, while the condition *d* specifically cuts noisy events, large back-scattering events and those events interacting before the second ladder.

The reconstructed clusters in a tricky double-track event is presented in figure 5.1. Tracks are well separated in the p side coordinates, whereas their

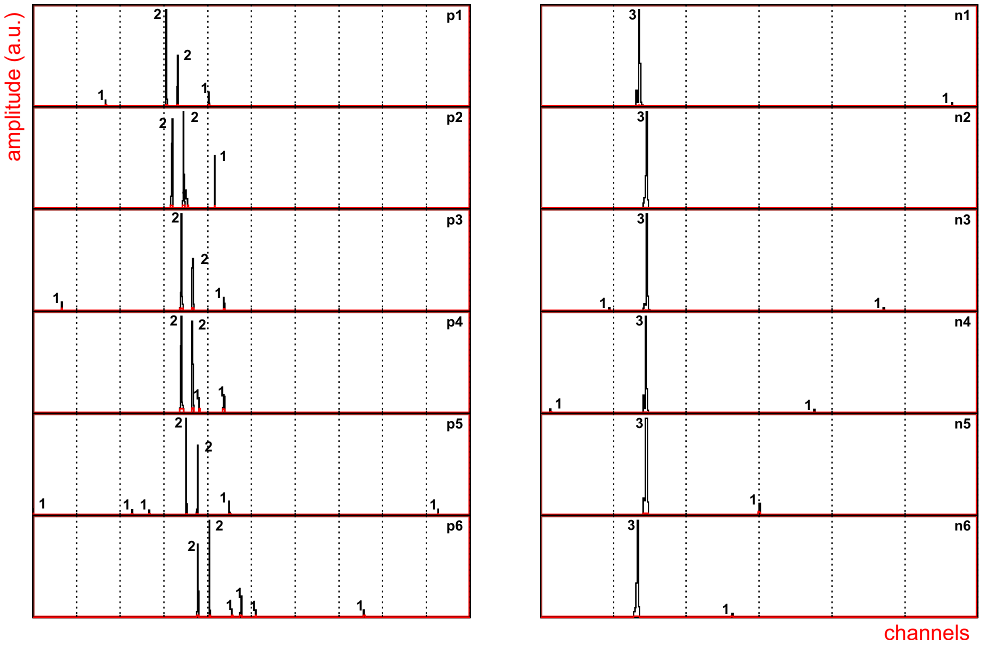

Figure 5.1: A typical double track event. From the top the six ladders single channel signal are presented respectively on the left for the p-side projection and on the right for the n-side. The two different tracks, shown on the p-side, are reconstructed as a whole track. Such events represents a background for the inelastic events selection.

high collimation in the orthogonal projection does not allow their separation in the orthogonal n side coordinates. Such events represent $\sim$ 5–10 % of the sample surviving a)–d) selection criteria and are efficiently rejected by the last cut (e).

The resulting sample consists of events with a single particle of charge Z entering the telescope with a well defined direction. For charges from Lithium to Fluorine the typical number of events selected in each Z sample is O(10^5) (first column in table 5.1).

A first, conservative, estimate of the fragmented events fraction in the preselected sample is obtained tagging the *clean* non-interacting particles in the full telescope. Such particles are defined as straight tracks crossing the whole Silicon telescope, reconstructed with a good 3D linear fit χ^2 as presented in the upper plot of figure 5.2. The associated charge is the one assigned by the likelihood ratio test (figure 5.2) and with a likelihood $L > 0.80$. Tracks with a minimum of 5 hits are considered in such a sample to account for hits reconstruction inefficiencies in a single ladder. An example of inelastic event,

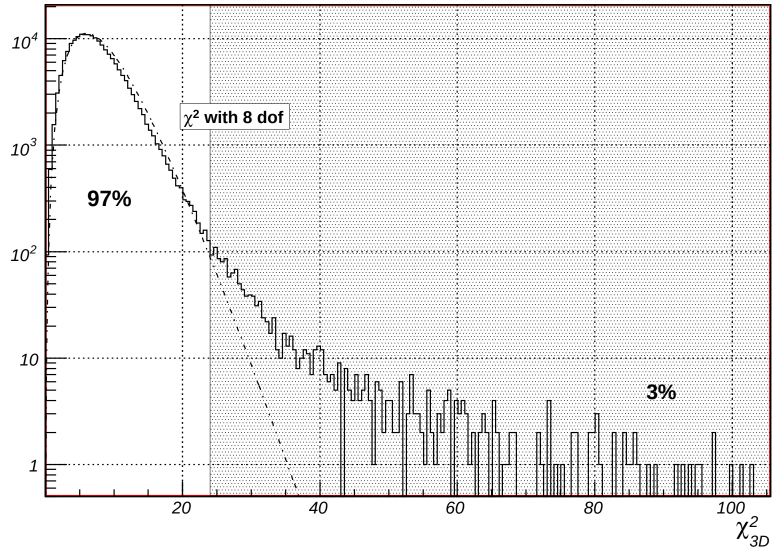

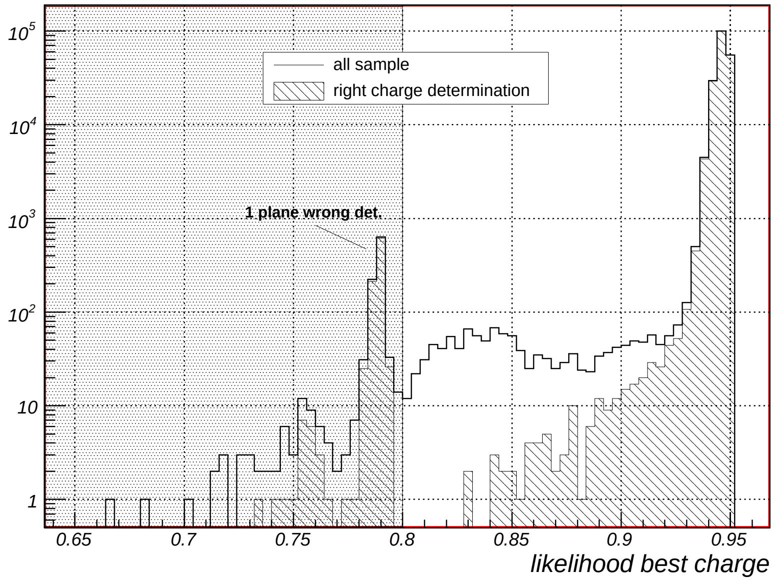

Figure 5.2: Top: The χ^2 distribution for the 3D 6 or 5 point linear fit for the Carbon sample (solid line). The expected 8 degrees of freedom χ^2 distribution is also superimposed (dashed line). Shadowed area defines the region of the *non-straight* tracks which are retained in the pre-selection. Bottom: The likelihood ratio estimates the best charge for the 6/5 point reconstruction. The corresponding likelihood distribution (solid line) with the request of a charge equal to the charge evaluated with the first two ladders (filled area) are presented. A cut is imposed up to likelihood values greater than 0.80.

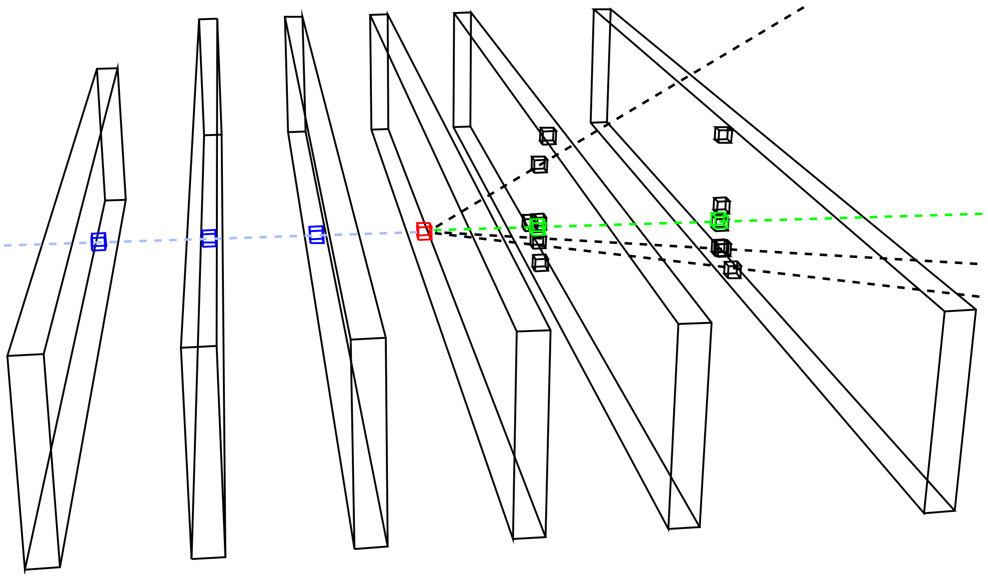

Figure 5.3: An example of a measured inelastic interaction in Silicon. A Beryllium nucleus (blue) interacts with Silicon producing a Lithium (green) and several $|Z| = 1$ (black) charge products. The hit corresponding to the inelastic vertex has a very large signal (red). Dashed lines are superimposed in order to exemplify the event topology.

where the fragmentation occurred in correspondence of the fourth ladder, is presented in figure 5.3.

The preliminary fragmented event fraction is then defined as the ratio between the number of *non-straight* events (in table 5.1, second column) and the number of preselected events in the upstream telescope.

The resulting fragmented events fraction is presented in figure 5.4 as a function of Z with respect to the simulated inelastic fraction. For all charge values, the measured values lie systematically above the expected ones. This discrepancy is a direct consequence of the conservative selection, i.e. of the quite tight cuts used to define a clean straight track in the rejected sample. Inefficiencies in the hit reconstruction and selection cuts can comfortably account for the over-estimated fragmentation at this pre-selection stage.

The more refined analysis of fragmented events, based on a preliminary MC study of possible tagging variables, will be detailed in section 5.3.

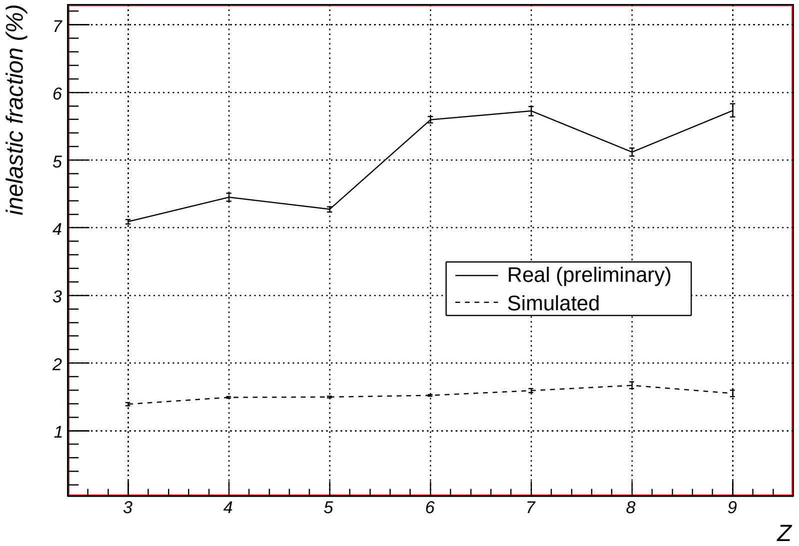

Figure 5.4: The fragmentation fraction after pre-selection. The real data fragmentation fraction is obtained by subtraction of straight tracks events from the upward telescope sample. The simulated fragmentation fraction is obtained requiring only events with inelastic vertices situated between the second and the sixth ladder with respect to the non-interacted sample on the first two ladders.

5.2 Monte Carlo Simulation

A detailed simulation of the inelastic events in the Silicon telescope has been used to analyze the typical topologies of fragmented events and to find out tagging variable useful in the beam test data analysis.

The beam test Monte Carlo simulation has been developed using the FLUKA code framework. In the following sections a brief description of the FLUKA physics models, of the simulated geometry setup and of the inelastic event reconstruction in terms of topology and tagging variables is given.

5.2.1 FLUKA Simulation

FLUKA is an interaction and transport Monte Carlo code developed to describe radiation/particle interactions with matter for a wide range of applications (cosmic rays, extensive air showers, radiation problems in space, etc).

The FLUKA physics interaction frame is described preferentially by microscopic first-principles models. In particular the charged hadrons transport in matter is performed by means of a detailed implementation of the multiple Coulomb scattering (Moliere theory) and of the ionization losses. The nucleus–nucleus inelastic interactions are accurately described by a set of specific models applied properly in order to follow the different steps of the interaction process. They are:

- Kinetic energy per nucleon < 5 GeV/n
  - **RQMD** (Relativistic Quantum Molecular Dynamics): describes the nuclei collisions as the semi-classical propagation of nucleons bound in a potential hole with target bounded nucleons. The nuclei fragmentation results from the nucleons scattering, no hadronization process is present.
  - **Pre-equilibrium phase**: based on a excitons model;
  - **Evaporation / Break-up / Photon emission**: residual nuclei disexcitation models.
- Kinetic energy per nucleon ≥ 5 GeV/n
  - **Glauber/Gribov theory**: describes the nucleus–nucleus interaction as the sum of all the single nucleon–nucleon interaction combination;
  - **DPM** (Dual Parton Model): describes the nucleon–nucleon interactions in terms of partons (quark, diquark) in case of *soft* collisions;
  - **Perturbative QCD** (Quantum Chromo-Dynamics): the three quarks nucleon structure model is used in case of *hard* collisions;
  - Both DPM and QCD describe the hadronization phase of the resulting quark chains (nucleons, K, Σ, $\ldots$);
  - **INC** (Intra-Nuclear Cascade): model for the particles, produced by hadronization, propagation in the residual nuclei;
  - **Pre-equilibrium phase**: based on a excitons model;
  - **Evaporation / Break-up / Photon emission**: residual nuclei disexcitation models.

The FLUKA code has been developed in the FORTRAN language and a C++ dedicated interface with the ROOT [87] framework was developed in

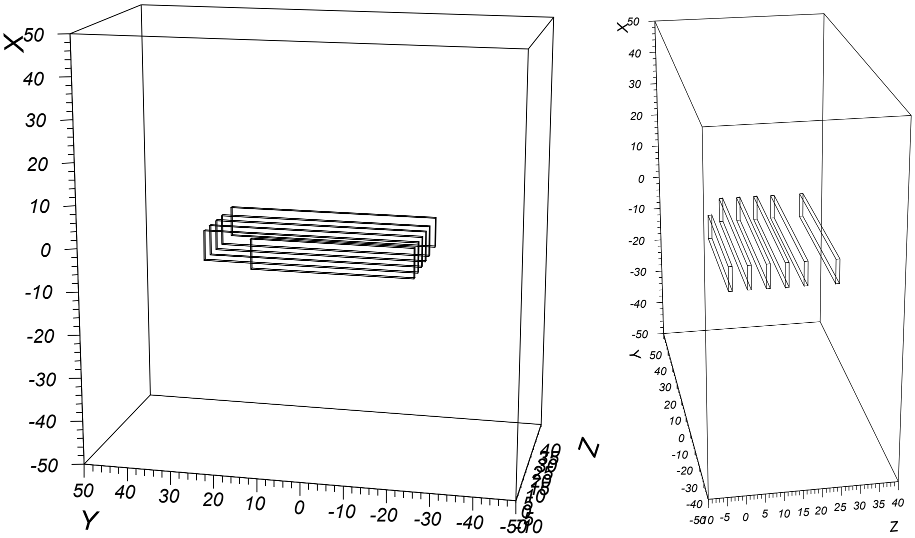

Figure 5.5: The beam test geometry setup. A detailed description of the ladder, in terms of sensor, kapton layer, Carbon skin and Airex reinforcement and spacer is implemented. Projectiles with charges up to Iron and kinetic energies of 158 GeV/n are simulated.

the context of the presented analysis. A unique homogeneous event display has also been developed within the ROOT framework for a 2D/3D graphical representation of the simulated and beam test events.

A detailed description of the physics models [88] implemented in FLUKA and the overall FLUKA framework [89] can be found in the referenced articles.

5.2.2 Implementation of the Test Beam geometry

The test beam setup has been reproduced in terms of the FLUKA geometry as sketched in figure 5.5. The FLUKA setup consists of six ladders positioned at the same relative distances as in the experimental layout.
Each simulated ladder is built from the same number of sensors as in the beam test configuration and it is described as the sum of different materials:

- a 300 µm Silicon bulk, covering the ladder active area;
- a 5 µm Kapton foil;
- two supporting $\sim$ 0.5 cm Airex structures, shaped and positioned as in AMS-02;

Physical process	**Threshold**
Δ-rays production	> 50 keV
e^+, e^- and γ transport	> 50 keV
Multiple Scattering	minimum allowed from Moliere theory
Hadron transport	> 50 keV
Heavy recoils transportation	activated
Heavy ions interactions (DPM-JET, RQMD-2.4)	activated
Detailed evaporation model	activated

Table 5.2: FLUKA customized settings for the principal physical processes.

- the Carbon fiber skin of ~ 10 µm which covers the lower Airex support.

The simulated beam is orthogonal to the ladders, approximately positioned as in the test beam setup. Ion projectiles of 158 GeV/c/n momentum where simulated for a global statistics of 10^6–10^7 events.

Particular attention has been put in setting up FLUKA physics parameters to simulate accurately Δ-rays production, multiple scattering, energy deposition in Silicon, inelastic nuclear interaction and nuclear interaction products propagation, energy deposition and multiple scattering (table 5.2).

5.2.3 Inelastic Events Topology

Peripheral relativistic-energy heavy-ion collision, resulting in fragments with mass close to those of projectile and target can be described basically by the abrasion model [90] (sketched in figure 5.6). When the relative velocity of the reaction partners is considerably larger than the nucleons Fermi velocity ($K_{\text{Fermi}} \sim 30MeV/n$), the nucleon-nucleon collisions are restricted to the overlap zone indicated by the impact parameter. The parts of the nucleus outside the overlap zone, called *spectators* preserve their kinetic energy, while in the interacting region a production of hadronic secondaries is observed. The nature and the abundances of the produced secondaries depends on the energy regime of the collision which again corresponds in FLUKA to a different choice of the interaction model (DPM or QCD).

As an example, figure 5.7 presents the energies of the products of a simulated 158 GeV/n Carbon projectile impinging on a Silicon target at rest in the laboratory frame. In such peripheral collisions the produced particles can be phenomenologically described as:

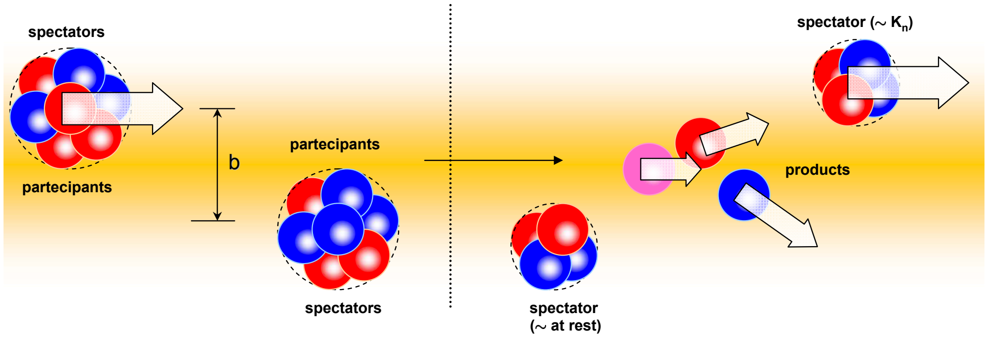

Figure 5.6: A schematic view of the nucleus–nucleus inelastic collision at high energies. Only the low impact parameter nuclei regions are involved in the fragmentation. Residual non-interacting nucleons are spectators and tend to conserve the original kinetic energy.

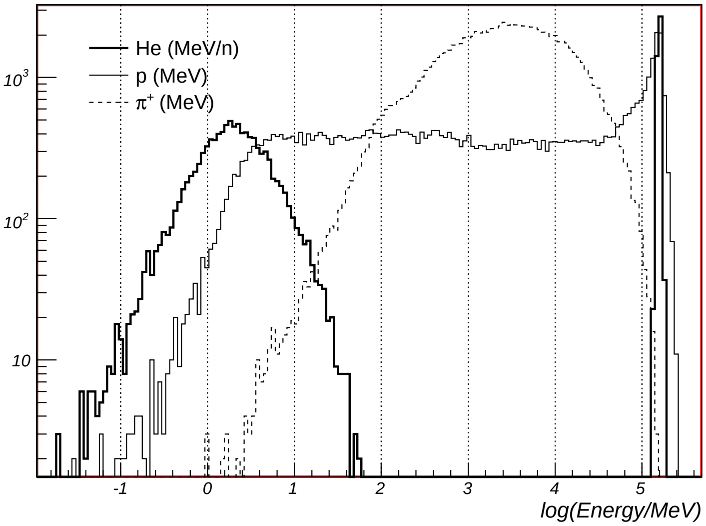

Figure 5.7: Simulated inelastic collision products energetic distribution for Carbon projectiles fragmenting on Silicon. Residual α nuclei are spectators of the interaction (produced at low energy from Silicon fragmentation, or at high energy by Carbon fragmentation), while intermediate energies pions are produced in the interacting region. Protons are both produced in the interacting and non-interacting region.

- **nuclear fragments nearly at rest (target spectators)**: the fragments of the target Silicon nucleus which have not taken part directly to the interaction (protons, α and nuclei with Z up to 14) have a low momentum transmitted, up ~ 100 MeV/n and have a very high probability of being stopped in a 300 µm Silicon sensor. As a consequence almost all of their kinetic energy is deposited by ionization in the Silicon sensor, producing a single cluster with a signal much more larger than a MIP $O(100 \cdot Z^2)$ keV. The observation, along the particle trajectory, of a cluster with a signal much more larger than what expected from the projectile charge, is then a clear signature of the interaction point.

- **nuclear fragments nearly at projectile energy (projectile spectators)**: the projectile spectators (protons, α and nuclei with Z up to the projectile charge) have nearly the kinetic energy per nucleon they had before the collision. They nearly preserve the direction of the projectile, with a very small angle spreading.

- **inelastic collision particle products**: the nuclear inelastic interaction provides a large production of neutral and unitary charge particles as protons, neutrons, pions (π^0, $\pi^\pm$) and many other unstable particles (K's, Σ's, ...). There is also a large production of photons due to the disexcitation process of the residual nuclei. The particles produced have a wide angular distribution reaching also the back-scattering region. The energetic distribution spans between the projectile and target initial energies.

At different values of the impact parameter b, the multiplicity and the nature of fragments produced in the nucleus–nucleus interaction change. As a result, quite different event topologies are expected ranging from very few secondaries, with one having nearly the mass of their parent (large b values), to high multiplicity events in more central collisions.

5.2.4 Hit Digitization

Primary particles are generated along the experimental beam direction, i.e. orthogonally to the telescope, 10 cm before the first ladder. FLUKA provides the transport, the interactions either in air or in the ladder material, the decay channels, both for the primaries and the produced secondaries particles.

The output of the simulation includes a complete description of the Monte Carlo event and a list of Monte Carlo hits. The MC event is described by the

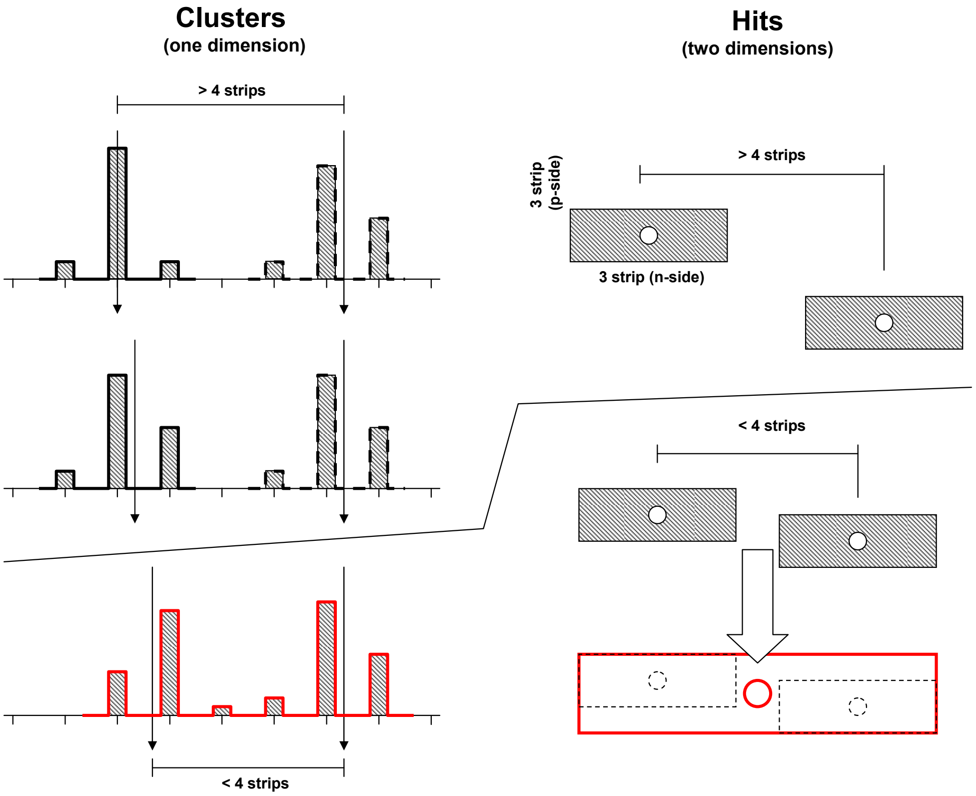

Figure 5.8: Left: two cluster closer than one strip are reconstructed as a whole unique cluster. Right: the hit digitization process groups hits with separation less than 1 strip simulating the clusterization effect.

list of the produced *particles* and the list their interaction *vertices*. For each vertex it is possible to know the nature and the position of the interaction as well as a list of the produced secondaries. The MC *hit* list contains the incident particles passage point trough the ladder together with the computed energy deposition in the Silicon.

A first selection of the MC hits excludes those located on non active parts of the Silicon detectors, the remaining set must be processed in order to pass from a point-like information to a digitized hit comparable to the real data.

The effective capability of the Si detectors to distinguish the energy deposit from two near particles interacting with Silicon within < 1 mm is the main effect to be accounted for. Two clusters which are not separated by an under threshold strip are reconstructed as a whole cluster which extends over the two regions (on the left of figure 5.8). This case is frequent in the fragmentation events where a bunch of collimated charged particles (mostly

p, $\pi^{\pm}$) exits from the interaction point.
The hit digitization is implemented as:

- a digitized hit is built for each MC point-like hit. To each hit is associated a rectangular *merging* region whose dimensions are fixed as a multiple of the strip readout pitch in the two sides, $208 \cdot n_x \times 110 \cdot n_y$ μm^2. For charges up to $Z = 3$ the number of strips used to define the merging regions is $n_x = n_y = 3$, whereas for higher charge values the cluster multiplicities presented in figure 4.1 have been used.
- when two digitized hits are overlapping within 208 (110) µm (1 strip pitch) in x (y) coordinate, they are joined into a single digitized hit;
- the energy deposition of the new hit is the sum of the energy depositions;
- the new coordinates are the weighted mean of the two hits ones, using as weights the energy depositions;
- the merging area associated to the new hit is the whole rectangular area extending over two hits (figure 5.8 on the right);

The n-side sensor periodic bonding scheme is also taken in account in order to correctly simulate the n-side ambiguity in the coordinate assignment.

No detailed description of the cluster charge amplitude distribution in terms of corrections arising from non-linearities in the charge collection (η dependence) or from electronics dependent effects (saturation, noise) has been implemented in the digitization.

5.3 Data/MC Comparison

The pre-selection cuts applied on the experimental data can be reproduced on the Monte Carlo sample imposing conditions on the inelastic vertex coordinates and on the produced number of secondaries. In figure 5.9 the fraction of events selected with at least one inelastic vertex after the upstream telescope are presented (black line).

The events with a large backscattering interaction after the second ladder may produce several hits in the upstream telescope and would be eliminated from the real data sample. To remove these events from the MC sample a maximum of 5 hits with charge $Z \leq 2$ is admitted on any of the two ladders of the upstream telescope. The resulting fraction of fragmentation events

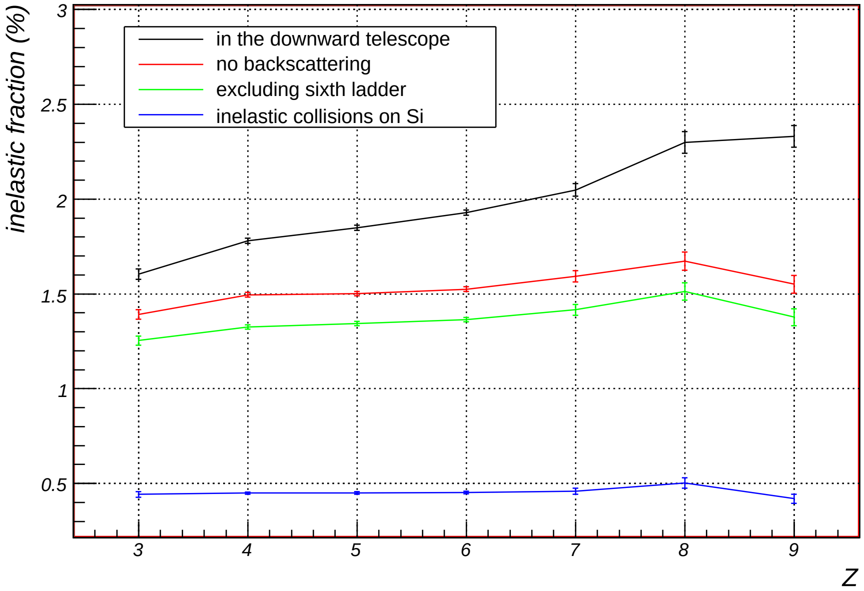

Figure 5.9: Inelastic fraction for the simulated sample, from the top: inelastic events in the downstream telescope, i.e. the 4 last ladders; without high backscattering events (red); in the downward telescope excluding the sixth ladder (green); with the constraint of inelastic events generated in collision within the Silicon detector medium (blue).

passing this cut is shown in figure 5.9 (red line). This is the same curve used as simulation reference in figure 5.4.

In this analysis the sixth ladder will be used to study the features of the fragmentation events, as a consequence only the interactions occurred before the sixth ladder must be taken in account. The inelastic fraction corresponding to fragmentation events either in the ~ 28 cm of air or in one of the three ladder before the sixth is presented in figure 5.9 (green line).

Since AMS-02 will be operated in vacuum the fraction of events with an inelastic interaction in Silicon sensors is the relevant quantity to assess the entity of nuclear fragmentation in the AMS-02 Tracker. The blue line in figure 5.9 represents the fraction of events with a fragmentation on one of the three ladders under examination. These events represent a fraction of $\sim 5 \cdot 10^{-3}$ of the initial sample, corresponding to a reduction factor of ~ 10 with respect the pre-selected real data sample for fragmentation analysis.

In real data tagging variables need to be defined to refine the fragmen-

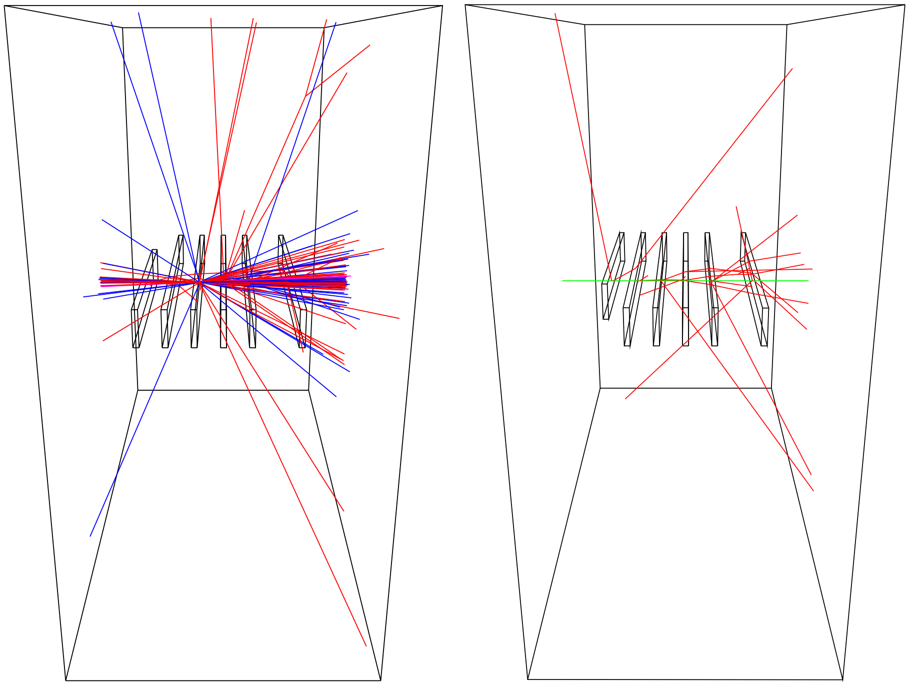

Figure 5.10: Left: A typical high backscattering event. In blue are presented the nuclear interaction products (protons, neutrons and pions), while in red electromagnetic sector particles (photons, electrons and positrons). Events with this topology are hardly reconstructable. Right: A Δ-rays (red lines) rich event. This event can be easily confused with low multiplicity inelastic events.

tation event selection discarding: (a) inelastic interactions in air and (b) non-fragmented events wrongly included in the fragmented sample as a consequence of a poor track reconstruction.

Inelastic collisions in ladders are characterized by target fragments emitted with a small kinetic energy. These fragments are completely absorbed within the Silicon detector. The absorption generates a large signal in the sensor strips that can be used as a signature of this kind of event with respect to the inelastic collision in air.

Inelastic events in air and in Silicon are characterized by the number of secondary produced in the collision. The number of produced particles depends on the impact parameter b, with smaller b values corresponding to higher secondary multiplicities. Not-fragmented ions are expected to be accompanied by a low multiplicity of secondaries, just due to Δ-rays production (proportional to Z^2) and possibly well separated by high multiplicity frag-

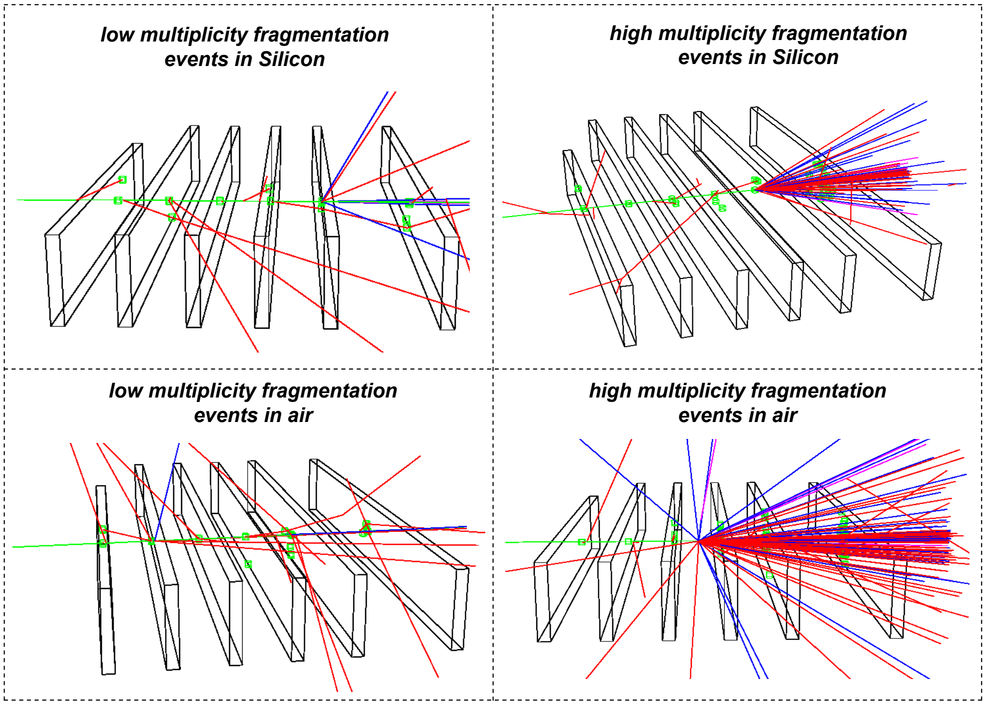

Figure 5.11: Several inelastic event topologies. The shown events are extracted from the Monte Carlo sample.

mentation events. Inelastic events interacting in air with low secondary production are prone to be experimentally confused with a normal ion track accompanied by an abundant Δ-rays production (a Δ-rich event is sketched in figure 5.10, right) due to the similar energy deposition of relativistic electrons and high energy inelastic collision products (mostly protons and charged pions). Multiplicity can be estimated in real data from the number of $Z = 1$ hits generated in the ladders after the interaction vertex.

These two properties, vertex position and number of secondaries, delineate different inelastic events topologies described as follows:

a. inelastic events interacting in Silicon with an high product multiplicity;

b. inelastic events interacting in Silicon with a low product multiplicity;

c. inelastic events interacting in air with a high product multiplicity;

d. inelastic events interacting in air with a low product multiplicity;

In figure 5.11 the four delineated inelastic categories are exemplified with several MC simulated events. In real data event distinction is expected to be complicated by the contamination of Δ-rays rich events contributing preferentially to d. category.

5.3.1 Fragmentation Events Tagging

The inelastic events description involves the vertex position and the number of secondaries produced. These characteristics can be estimated in the real data fragmentation sample using the following experimentally accessible variables:

- **maximum amplitude**: an inelastic interaction occurring in the sensor bulk medium causes a very large energy deposit due to residual recoil Silicon fragments. The corresponding hit is the one with the largest signal in the event. The study of the signal of the maximum amplitude hit can then allows for the identification of interaction vertices in Silicon;

- **crowding**: an evaluation of the charged products out from the interaction vertices can be obtained counting the number of hits of unitary charge on the last ladder of the telescope. This number is subtracted by the number of hits of unitary charge present on the second ladder in order to obtain a parameter independent from the number of secondary tracks accompanying the principal event. This parameter is called *crowding*.

These two variables have been tested on the Monte Carlo data in order to validate their usefulness in the description of the inelastic event topologies.

As expected the crowding parameter can distinguish between the non-interacted events from the inelastic sample using the information in the MC event list (upper plot of figure 5.12). The spread of the non-fragmented distribution is due to the Δ-rays multiplicity while the long tail of the fragmented distribution is due to the high multiplicity inelastic events.

The number of charged secondaries produced in the inelastic interaction and not immediately absorbed in material, can be a good definition of the multiplicity of an interacted event. This parameter is nearly proportional to crowding (as presented in figure 5.13) and a cut of about ~ 5 corresponds to a multiplicity threshold of ~ 8 charged particles. Events above this threshold are considered as characterized by *high multiplicity*. Events below the threshold are defined as *low multiplicity* and represent ~ 15 % of the fragmented sample. With this definition the high multiplicity sample is expected to have a contamination ~ 1 % from the non-fragmented sample.

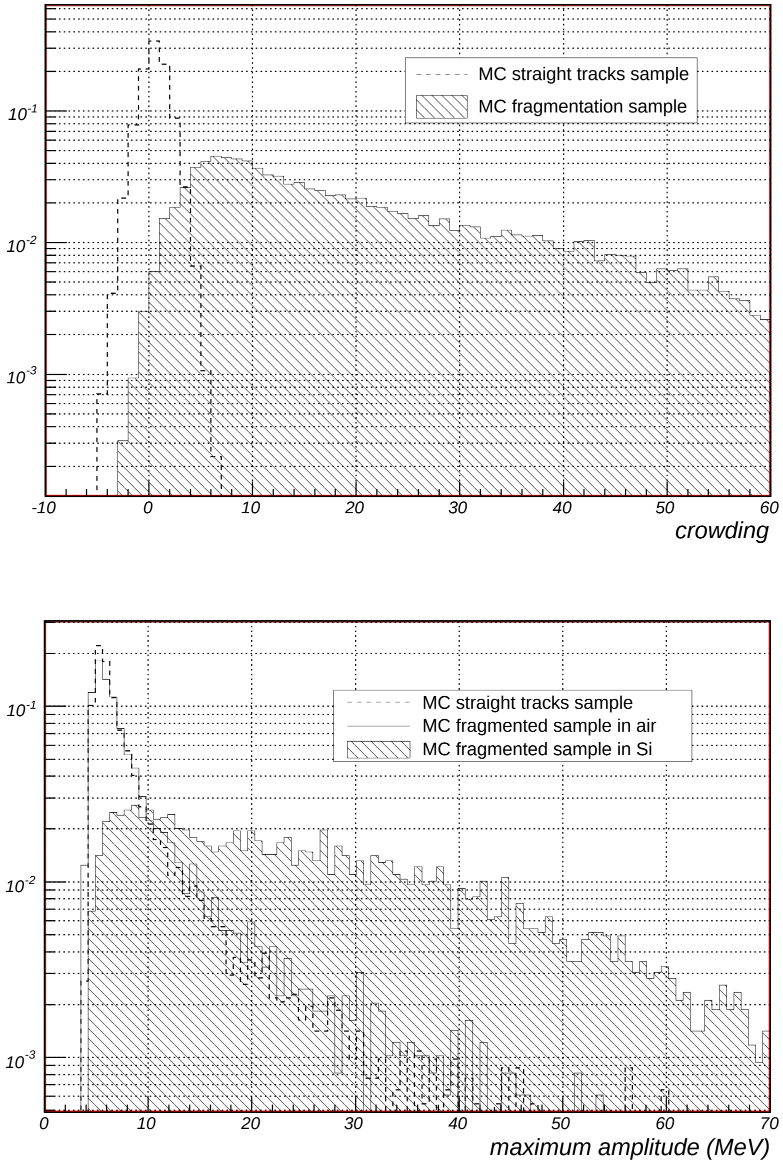

Figure 5.12: Upper: crowding normalized distribution for not interacted events (dashed line) with respect to the fragmented events (filled area). Lower: the normalized maximum amplitude distribution for not interacted events (dashed line) compared with distributions for inelastic collision happened in air (solid line) or in Silicon (filled area).

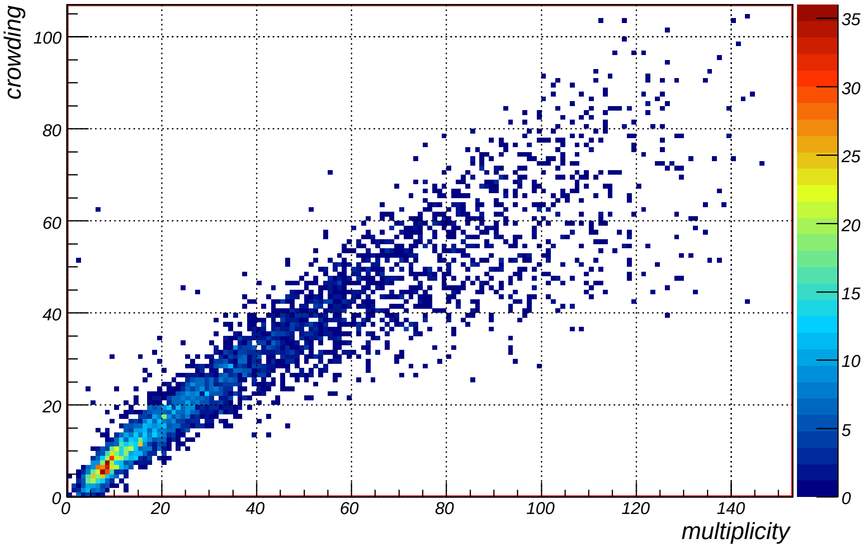

Figure 5.13: Particle multiplicity is proportional to crowding.

Two samples containing primaries inelastic collisions in air and inelastic collisions in the ladders were constructed using the MC information about the inelastic vertex location. The lower plot of figure 5.12 shows the maximum amplitude for events fragmented in air, in Silicon or not fragmented. The distributions for not fragmented and fragmented in air samples are quite similar and well separated from the bulk of events interacted in Silicon with a cut at $\sim$ 15 MeV.

Four MC data samples, corresponding to the inelastic topology categories delineated in section 5.3 and sketched in figure 5.11, have been selected using the proposed definition of low and high multiplicity and information about the vertex location. These samples will be compared in the next section with real data samples obtained applying the amplitude and crowding cuts.

5.3.2 Data Tagging

The chosen tagging variables, i.e. maximum amplitude and crowding, must be applied to the data sample in order to distinguish the fragmentation categories. In figure 5.14 the tagging variables distributions as observed in a Carbon sample are shown. Distributions are presented both for the sample of not fragmented, i.e. straight track, events (dashed line) and for the preselected fragmentation events (solid line). The filled area plot corresponds

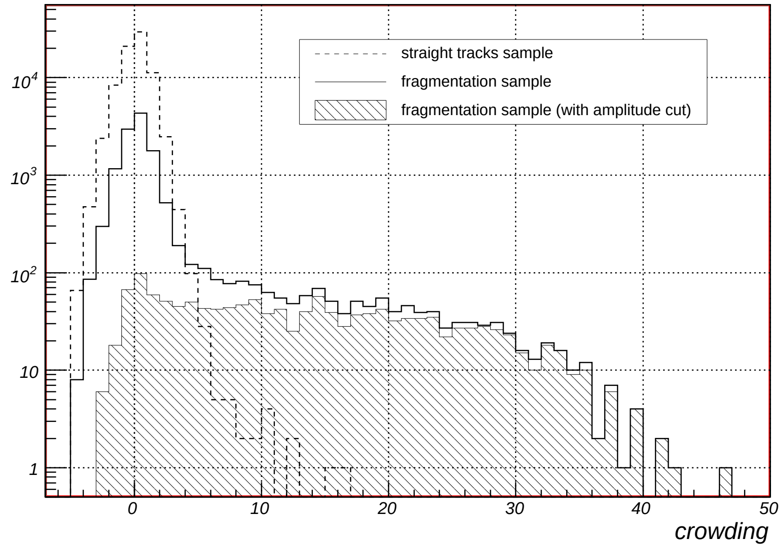

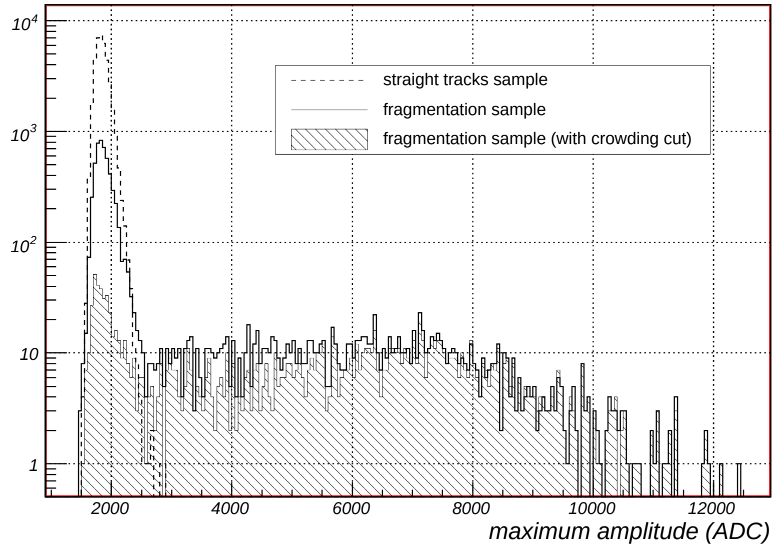

Figure 5.14: Top: the crowding parameter for the fragmented (solid line) and straight tracks (dashed line) samples. The crowding distribution for events fragmented in Silicon, selected with a cut on the maximum amplitude parameter, is superimposed (filled area). Bottom: real data sample maximum amplitude for a fragmented (solid line) and straight tracks (dashed line). The filled area corresponds to the maximum amplitude distribution for the fragmented sample when a cut selecting high multiplicity events (crowding > 5) is applied.

to a cut of the fragmented sample on the complementary tagging variable.

In the upper plot of 5.14 the crowding parameter is presented. The dashed line corresponds to the non-fragmented event sample: the crowding is clearly peaked around 0, with a dispersion reflecting the production of secondary Δ-rays. The solid line described the crowding distribution in the pre-selected fragmented sample: it results well separated from the non-fragmented peak at values of crowding > 5, where only a $\sim 0.1\%$ of the not fragmented tracks are observed. The solid line corresponds to the fragmented sample well separated at high crowding from the straight tracks distribution. At low crowding values a peak corresponding to the not fragmented distribution is found, however this is consistent with the expected Δ-rays rich events contamination. Applying a cut on the maximum amplitude (> 2500 ADC for Carbon), corresponding to the request of events interacting in the ladders, the peak is dramatically reduced, leaving still a small residual contamination.

Maximum amplitude distribution is presented in figure 5.14, lower plot. The dashed line corresponds to the not fragmented sample. Solid line, corresponding to fragmentation events, is well separated above 2500 ADC (different thresholds have been imposed for different charges between $3 \leq Z \leq 9$). As studied in MC (figure 5.12) the peak at low amplitudes should be populated by inelastic events with vertex in air and not fragmented events.

The filled area corresponds to high multiplicity events, selected on the basis of the crowding. The fraction of events at high amplitude, i.e. truly interacting in the Silicon, is basically unchanged, whereas a significant reduction of the sample at low amplitude values is obtained. Genuine inelastic events in air and a background of badly reconstructed tracks compose the surviving sample at low amplitude values: in absence of further tagging variables is not possible to disentangle the two contributions, results will be then presented exclusively in terms of fragmentation fractions in Silicon.

The amplitude cut is quite effective in reducing the instrumental background contribution in the Silicon fragmentation sample: the actual value of the cut is evaluated for each species on the basis of the amplitude distribution observed in the straight track sample and fixed requiring a rejection $\geq$ 99% of the straight-track sample events.

The inelastic fraction relative to an interaction with any of the three ladders and separately for each one is compared to the corresponding simulated inelastic fraction in Silicon in the uppermost plot of figure 5.15. The slight excess observed in the data with respect to the Monte Carlo estimates can be related to the remaining contamination due to Δ-rays, ion interactions in air or instrumental background.

A further splitting of the selected sample in low and high multiplicity events on the basis of the crowding parameter has been performed. Results

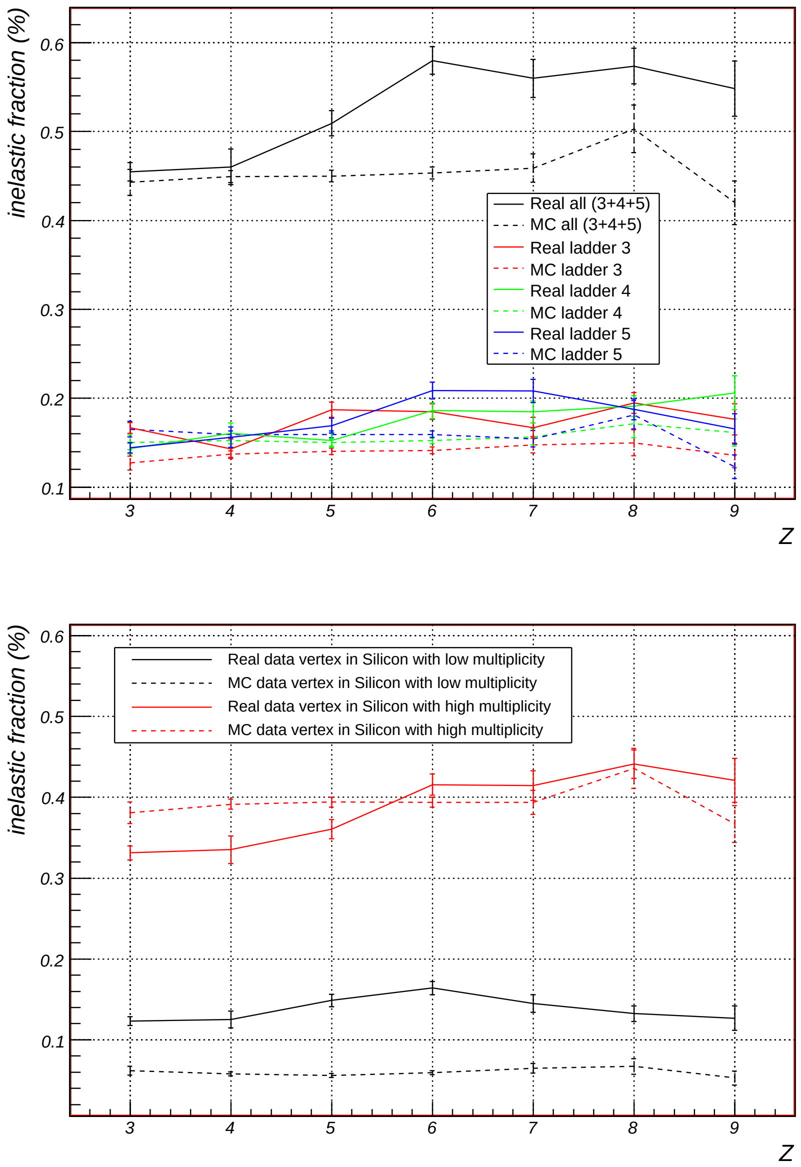

Figure 5.15: Lower: Inelastic fraction of events with inelastic vertex in Silicon, counted in the three separated ladders (red, green, blue) under analysis and as the sum of the three (black line). The real data (solid lines) are compared with the Monte Carlo simulated sample (dashed lines). Upper: The inelastic fraction for the events interacted in Silicon in case of (black) low multiplicity and (red) high multiplicity.

are presented in the lower plot of figure 5.15. A clear excess is observed in the low multiplicity data, which are more sensitive to background contaminations, with respect to the simulation, whereas the fragmentation fraction measured in the high multiplicity events is well in agreement with the simulation, fully validating the FLUKA prediction.

Conclusion

A detailed study of the AMS-02 Silicon tracker response to ultra-relativistic ions has been performed in this thesis, based on the analysis of 10^7 collected beam test events with charges $1 < Z < 30$.

An accurate characterization of the signal released by ion species with $2 < Z < 10$ in the AMS-02 double-sided Silicon sensors has been performed. Signal dependencies on the impact position and the ion charge have been studied in detail on each ladder/side separately and a set of effective corrections have been implemented in order to describe with an unique functional form the sensors response. A likelihood-based charge reconstruction algorithm has been developed and tested obtaining a correct charge reconstruction for examined ion species in the $\sim 95\%$ of the events on a single ladder and in the $\sim 99\%$ of the combined measurements from five ladders. On the basis of the experimental distributions, a combinatorial Monte Carlo has been used to evaluate the charge reconstruction performances with the eight tracker planes. A complete separation has been estimated within generated samples of 10^7 particles, i.e. the expected statistic for the more abundant heavy elements in the AMS-02 data taking period.

The procedure developed to correct for the non-linearities observed in signal collection on the sensors p-side resulted in a simultaneous improvement in the impact position measurement. As a consequence a spatial resolution of 5 µm, independent from the ion charge, has been achieved in the bending coordinate measurement. This spatial resolutions will allow a AMS-02 Si Tracker rigidity measurement up to 3.7 TV for ions.

A signal-based correlation algorithm to pair p and n side clusters has been developed and tested on a sample of ion straight tracks. The resulting three-dimensional hits were used to reconstruct 3D linear tracks with an associated unique charge, i.e. *particles*. As a consequence also the fragmented, i.e. *not-straight*, events could be recognized and studied.

A FLUKA based simulation of the beam test setup has been developed to reproduce the ion nuclear interactions with the ladder material. The description of the Monte Carlo events in terms of digitized 3D hits has been used in order to drive the analysis of the experimental data.

A substantial agreement between the measured and expected nuclear fragmentation fraction in the silicon detectors has been found. This result leads the way to a FLUKA based detailed simulation of the CR nuclei interactions in the AMS-02 material, a key point for the accurate measurement of the GCRN fluxes.

Acknowledgements

I thank all the people involved in the development of this Ph.D. thesis. In particular I would like to express my gratitude to professor Roberto Battiston for the opportunity of collaborating with the AMS-02 Perugia group members. Working and sharing discussion with them has been the chance of a human and scientific growth. I would like to address special thanks to my advisor, professor Bruna Bertucci for her support, advice and endless patience in improving my writing. I would thank doctor Paolo Zuccon for his guidance and help in achievement of this work. Finally never enough thanks to my family, especially for the little newcomer Aurora, and to my dear patient Gaia.

Bibliography

[1] J. Alcaraz et al. The alpha magnetic spectrometer silicon tracker: performance results with electrons, protons and helium nuclei. Submitted to Nuclear Instruments and Methods in Physics Research A.

[2] R. Battiston et al. Cosmic ray physics from low to extreme energies: Status and perspectives Observations and Implications of the Ultra-High-Energy Cosmic Rays. *Advances in Space Research*, 37:1834–1840, 2006.

[3] A. Strong and I. Moskalenko. Propagation of Cosmic-Ray Nucleons in the Galaxy. *The Astrophysical Journal*, 509:212–228, 1998.

[4] W. Baade and F. Zwicky. Remarks on Super-Novae and Cosmic Rays. *Physical Review*, 46:76, 1934.

[5] R. D. Blandford and J. P. Ostriker. Supernova Shock Acceleration of Cosmic Rays in the Galaxy. *The Astrophysical Journal*, 237:793–808, 1980.

[6] F. Aharonian et al. Primary particle acceleration above 100 TeV in the shell-type Supernova Remnant RX J1713.7-3946 with deep H.E.S.S. observations. *The Astrophysical Journal*, 464:235–243, 2007.

[7] N. E. Yanasak et al. Measurement of the Secondary Radionuclides ^{10}Be, ^{26}Al, ^{36}Cl, ^{54}Mn and ^{14}C and Implications for the Galactic Cosmic-Ray Age. *The Astrophysical Journal*, 563:768–792, 2001.

[8] J. Hörandel. Cosmic-ray composition and its relation to shock acceleration by supernova remnants. astro-ph/0702370v2, 2007.

[9] T. Antoni et al. KASCADE measurements of energy spectra for elemental groups of cosmic rays: Results and open problems. *Physical Review Letters*, 24:1–25, 2005.

[10] M. Nagano and A.A. Watson. Observations and Implications of the Ultrahigh-Energy Cosmic Rays. *Review Modern Physics*, 72:689, 2000.

[11] V. Berezinsky et al. On Astrophysical Solution to Ultra High Energy Cosmic Rays. hep-ph/0204357, 2006.

[12] K. Greisen. End to the Cosmic Ray Spectrum? *Physical Review Letters*, 16:748, 1966.

[13] N. Hayashida et al. Observation of a Very Energetic Cosmic Ray Well Beyond the Predicted 2.7K Cutoff in the Primary Energy Spectrum. *Physical Review Letters*, 73:3491–3494, 1974.

[14] HiRes Collaboration. Measurement of the Flux of Ultrahigh Energy Cosmic Rays from Monocular Observations by the High Resolution Fly's Eye Experiment. *Physical Review Letters*, 92:151101, 2004.

[15] T. Yamamoto. The UHECR Spectrum Measured at the Pierre Auger Observatory and Its Astrophysical Implications. In *30th International Cosmic Ray Conferences*, 2007.

[16] S. Burles et al. Big-Bang Nucleosynthesis: Linking Inner Space and outer Space. astro-ph/9903300, 1999.

[17] M. Garcia-Munoz et al. Cosmic-Ray Propagation in the Galaxy an in the Heliosphere: the Path-Lenght Distribution at Low Energies. *The Astrophysical Journal Supplement*, 64:269–304, 1987.

[18] D. Maurin et al. Cosmic Rays Below $Z = 30$ in a Diffusion Model: New Constraints on Propagation Parameters. *The Astrophysical Journal*, 596:555–585, 2001.

[19] J. A. Simpson and J. J. Connell. Cosmic-Ray ^{2}6Al and Its Decay in the Galaxy. *The Astrophysical Journal*, 497:L85–L88, 1998.

[20] A. Strong and I. Moskalenko. Models for Galctic Cosmic-Rays Propagation. *Advance in Space Research*, 27:717–726, 2001.

[21] A. Strong and I. Moskalenko. Solar System Abundances And Condensation Temperatures of The Elements. *The Astrophysical Journal*, 591:1220–1247, 2003.

[22] J.-P. Meyer et al. Galactic Cosmic Rays from Supernova Remnants: II Shock Acceleration of Gas and Dust. *The Astrophysical Journal*, 487:182, 1997.

[23] M. E. Wiedenbeck et al. Refractory Nuclides in the Cosmic-Ray Source. In *28th International Cosmic Ray Conference*, 2003.

[24] W. R. Binns et al. Wolf-Rayet Stars, OB Associations, and the Origin of Galactic Cosmic Rays. *New Astronomy Reviews*, 50:516–520, 2006.

[25] M. E. Wiedenbeck et al. Constraints on the Time Delay between NucleoSynthesis and Cosmic-Ray Acceleration from Observations ^{5}9Ni and ^{5}9Co. *The Astrophysical Journal*, 523:L61–L64, 1999.

[26] E. Vangioni-Flam et al. Lithium-6: evolution from Big Bang to present. *New Astronomy*, 4:245–254, 1999.

[27] A. Castellina and F. Donati. Diffusion Coefficient and Acceleration Spectrum from Direct Measurements of Charged Cosmic Ray Nuclei. *Astroparticle Physics*, 24:146–159, 2005.

[28] T. Hams et al. Measurement of the Abundance of Radioactive ^{10}Be and Light Isotopes in Cosmic Radiation up to 2 GeV/n with the Balloon-borne Instrument ISOMAX. *The Astrophysical Journal*, 611:892–905, 2004.

[29] S. M. Niebur et al. CRIS Measurements of Electron-Capture-Decay Isotopes: ^{37}Ar, ^{44}Ti, ^{49}V, ^{51}Cr, ^{55}Fe and ^{57}Co. In *27th International Cosmic Ray Conference*, 2001.

[30] E. C. Stone et al. The Cosmic Ray Isotope Spectrometer for the Advanced Composition Explorer. *Space Science Reviews*, 86:1–4, 1998.

[31] Y. Ajima et al. A Superconducting Solenoidal Spectrometer for a Balloon-borne Experiment. *Nuclear Instruments and Methods A*, 443:71–100, 2000.

[32] T. Yoshida et al. BESS-Polar Experiment. *Advances in Space Research*, 33:1755–1762, 2004.

[33] M. Boezio et al. The CosmicRay Proton and Helium Spectra measured with the CAPRICE98 balloon experiment. *Astroparticle Physics*, 19:583–604, 2003.

[34] R. Bellotti et al. Measurement of the Negative Muon Spectrum between 0.3 and 40 GeV/c in the Atmosphere. *Physics Review D*, 53:35, 1996.

[35] M. Aguilar et al. The Alpha Magnetic Spectrometer (AMS) on the International Space Station, Part I, Results from the test flight on the Space Shuttle. *Physics Reports*, 366/6:331–404, 2002.

[36] A. D. Panov et al. Relative abundances of cosmic ray nuclei B-C-N-O in the energy region from 10 GeV/n to 300 GeV/n. Results from ATIC-2 (the science flight of ATIC). In *30th International Cosmic Ray Conferences*, 2007.

[37] F. Gahbauer et al. A New Measurement of the Intensities of the Heavy Primary Cosmic-Ray Nuclei around 1 TeV per amu^{-}1. *The Astrophysical Journal*, 607:333–341, 2004.

[38] E. S. Seo et al. Cosmic-ray energetics and mass (CREAM) balloon project. *Advances in Space Research*, 33:1777–1785, 2004.

[39] Auger Collaboration. Properties and performance of the prototype instrument for the Pierre Auger Observatory. *Nuclear Instruments and Methods in Physics Research A*, 523:50–95, 2004.

[40] G. DAli Staiti for the EUSO Collaboration. EUSO A Space Mission Searching for Extreme Energy Cosmic Rays and Neutrinos. *Nuclear Physics B (Proc. Suppl.)*, 136:415–432, 2004.

[41] Y. Takizawa et al. JEM-EUSO: Extreme Universe Space Observatory on JEM/ISS. *Nuclear Physics B (Proc. Suppl.)*, 166:72–76, 2007.

[42] D. Nitz for the Pierre Auger Collaboration. The Northern Site of the Pierre Auger Observatory. In *30th International Cosmic Ray Conference*, 2007.

[43] S. A. Stephens and R. E. Streitmatter. Cosmic-Ray Propagation in the Galaxy: Techniques and the Mean Matter Traversal. *The Astrophysical Journal*, 505:266–277, 1998.

[44] E. Júliusson. Charge composition and Energy Spectra for Cosmic Rays at Energies above 20 GeV per Nucleon. *The Astrophysical Journal*, 191:331–348, 1974.

[45] C. D. Orth et al. Abundances and Spectra for Cosmic-Ray Nuclei from Lithium to Iron from 2 to 150 GeV per Nucleon. *The Astrophysical Journal*, 226:1147–1161, 1978.

[46] R. C. Maehl et al. Energy Spectra of Cosmic Ray Nuclei: $4 \leq Z \leq 26$ and $0.3 \leq E \leq 2$ GeV/amu. *Astrophysics and Space Science*, 43:163, 1977.

[47] J. H. Caldwell. Charge composition and Energy Spectra for Cosmic Rays Nuclei at Energies above 5 GeV per Nucleon. *The Astrophysical Journal*, 218:269–285, 1977.

[48] J. A. Lezniak et W. R. Webber. The Charge composition and Energy Spectra of Cosmic Rays Nuclei from 300 MeV per Nucleon to 50 GeV per Nucleon. *The Astrophysical Journal*, 223:676–696, 1978.

[49] M. Simon et al. Energy Spectra of Cosmic-Ray Nuclei to above 100 GeV per Nucleon. *The Astrophysical Journal*, 239:712–724, 1980.

[50] R. Dwyer et P. Meyer. Cosmic-Ray Elemental Abundances from 1 to 10 GeV per AMU from Boron through Nickel. *The Astrophysical Journal*, 322:981–991, 1987.

[51] Y. Takahashi for the JACEE Collaboration. Elemental Abundance of High Energy Cosmic Rays. *Nuclear Physics B (Proc. Suppl.)*, 60B:83–92, 1998.

[52] J. J. Engelmann et al. Charge Composition and Energy Spectra of Cosmic-Ray Nuclei for Elements from Be to Ni. Results from HEAO-3-C2. *Astronomy and Astrophysics*, 233:96–111, 1990.

[53] D. Müller et al. Energy Spectra and Composition of Primary Cosmic Rays. *The Astrophysical Journal*, 374:356–367, 1991.

[54] J. Buckley et al. A New Measurement of Flux of the Light Cosmic-Ray Nuclei at High Energies. *The Astrophysical Journal*, 429:736–747, 1994.

[55] M. Hareyama and T. Shibata for the RUNJOB collaboration. Results of RUNJOB and Related Topics. *Journal of Physics: Conference Series*, 47:106–112, 2006.

[56] J. T. Link et al. Measurements of the Ultra-Heavy Galactic Cosmic-Ray Abundances between Z=30 and Z=40 with the TIGER Instrument. In *28th International Cosmic Ray Conferences*, 2003.

[57] J. S. Young et al. The Elemental and Isotopic Composition of Cosmic Rays: Silicon to Nickel. *The Astrophysical Journal*, 246:1014–1030, 1981.

[58] E. C. Stoner et al. Cosmic Ray Investigation for the Voyager Missions; Energetic Particle Studies in the Outer Atmosphere - and Beyond. *Space Science Reviews*, 21:355, 1977.

[59] R. A. Mewaldt et al. The Isotopic Composition of the Anomalous Low Energy Cosmic-Rays. *The Astrophysical Journal*, 283:450–456, 1984.

[60] M. A. DuVernois and M.R. Thayer. The Elemental Composition of the Galcatic Cosmic-Ray Source: Ulysses High-Energy Telescope Results. *The Astrophysical Journal*, 465:982–984, 1996.

[61] D. Müller et al. The TRACER Project: Instrument Concept, Balloon Flights, and Analysis Procedures. In *30th International Cosmic Ray Conferences*, 2007.

[62] P. J. Boyle et al. Cosmic Ray Energy Spectra of Primary Nuclei from Oxygen to Iron: Results from the TRACER 2003 LDB Flight. In *30th International Cosmic Ray Conferences*, 2007.

[63] P. Picozza et al. PAMELA – A Payload for Antimatter Matter Exploration and Light-nuclei Astrophysics. *Astroparticle Physics*, 27:296–315, 2007.

[64] P. Chardonnet et al. The Production of Anti-Matter in Our Galaxy. *Physics Letters B*, 409:313–320, 1997.

[65] AMS-01 Collaboration. Cosmic-ray positron fraction measurement from 1 to 30 GeV with AMS-01. *Physics Letters B*, 646:145–154, 2007.

[66] B. Bertucci et al. AMS-gamma: High energy photons detection with the Alpha Magnetic Spectrometer on the ISS. In *27th International Cosmic Ray Conference*, 2001.

[67] The AMS Collaboration. AMS on ISS Construction of a particle physics detector on the International Space Station. to be published on Nuclear and Instruments Methods.

[68] B. Blau et al. The Superconducting Magnet System of the Alpha Magnetic Spectrometer AMS-02. *Nuclear Instruments and Methods in Physics Research A*, 518:139–142, 2004.

[69] Th. Kirn et al. The AMS-02 transition radiation detector. *Nuclear Instruments and Methods in Physics Research A*, 535:165–170, 2004.

[70] Ph.v. Doetinchem et al. Performance of the AMS-02 Transition Radiation Detector. *Nuclear Instruments and Methods in Physics Research A*, 558:526–535, 2006.

[71] L. Amati et al. The TOF counters of the AMS-02 experiment: space qualification tests and beam test results. *Nuclear Physics B (Proc. Suppl.)*, 150:276–280, 2006.

[72] A. Oliva. Riconoscimento di raggi cosmici con numero atomico Z ¡ 20 con gli scintillatori plastici del sistema TOF di AMS-02. Master's thesis, Universita degli studi di Bologna, 2004.

[73] T. Bruch and W. Wallraff. The Anti-Coincidence Counter Shield of the AMS Tracker. *Nuclear Instruments and Methods in Physics Research A*, 572:505–507, 2007.

[74] E. Lanciotti. *Estudio de las capacidades del detector RICH de AMS mediante el analisis de los datos de un prototipo e un haz de iones.* PhD thesis, Universitad Complutense de Madrid, 2006.

[75] F. Cadoux et al. The AMS-02 Electromagnetic Calorimeter. *Nuclear Physics B (Proc. Suppl.)*, 113:159–165, 2002.

[76] W. M. Yao et al. Review of particle physics. *Journal of Physics G*, 33:1+, 2006.

[77] B. Alpat et al. Charge Determination of Nuclei with the AMS-02 Silicon Tracker. *Nuclear Instruments and Methods in Physics Research A*, 518:121–130, 2004.

[78] C. N. Chou. The Nature of the Saturation Effect of Fluorescent Scintillators. *Physical Review*, 87:904–905, 1952.

[79] J. Casaus. Cosmic-Ray Astrophysical with AMS-02. In *28th International Cosmic Ray Conferences*, 2003.

[80] N. W. Ashcroft and N. D. Mermin. *Solid State Physics*. Saunders College Publishing, 1976.

[81] G. Lutz and A. S. Shwarz. Silicon Devices for Charged-Particle Track and Vertex Detection. *Annual Review in Nuclear Particle Science*, 45:295–335, 1995.

[82] W. Dabrowski et al. Study of Spatial Resolution and Efficiency of Silicon Strip Detectors with Charge Division Readout. *Nuclear Instruments and Methods in Physics Research A*, 383:137–143, 1996.

[83] P. Azzarello. Tests And Production of the AMS-02 Silicon Tracker Detectors. Master's thesis, Universite de Geneve, 2004.

[84] G. Ambrosi. The AMS Silicon Tracker readout system: Design and Performance. *Nuclear Instruments and Methods in Physics Research A*, 435:215–223, 1999.

[85] P. Aguayo et al. Prototype Study of the Cherenkov Imager of the AMS Experiment. *Nuclear Instruments and Methods in Physics Research A*, 560:291–302, 2006.

[86] M. Buénerd and I. Efthymiopoulos. A High Energy Secondary Beam of Ion Fragments for Instrumental Tests at CERN. Technical report, CERNAB2003052 ATB, 2003.

[87] R. Brun and F. Rademakers. ROOT – An Object Oriented Data Analysis Framework. *Nuclear Instruments and Methods in Physics Research A*, 389:81–86, 1997.

[88] A. Fassò et al. The Physics Models of FLUKA: Status and Recent Developments. In *Computing in High Energy and Nuclear Physics*, 2003.

[89] A. Fassò et al. FLUKA: a Multi-Particle Transport Code. *CERN*, 10, 2005.

[90] A. S. Goldhaber. Statistical Models of Fragmentation Processes. *Physics Letters B*, 53:306–308, 1974.

[91] for the MAGIC Collaboration Daniel Ferenc. The MAGIC Gamma-Ray Observatory. *Nuclear Instruments and Methods in Physics Research A*, 553:274–281, 2007.

[92] F. Aharonian et al. Cosmic Ray Proton Spectrum Determined with the Imaging Atmospheric Cherenkov Technique. *Physical Review D*, 59:092003, 1999.

[93] T. C. Weekes et al. VERITAS: the Very Energetic Radiation Imaging Telescope Array System. *Astroparticle Physics*, 17:221–243, 2002.

[94] W. R. Binns et al. Cosmic-Ray Neon, Wolf-Rayet Stars, and the Superbubble Origin of Galactic Cosmic Rays. *The Astrophysical Journal*, 634:351–364, 2005.

[95] R. Zei et al. Preliminary Measurements of Carbon and Oxygen Spectra from the Second Flight of CREAM. In *30th International Cosmic Ray Conferences*, 2007.

[96] H. M. Cathey et al. Design and Testing of the ULDB Vehicle. *Advances in Space Research*, 30:1215–1220, 2002.

[97] G. Bertone et al. Particle Dark Matter: Evidence, Candidates and Constraints. *Physics Reports*, 405:279–390, 2005.

[98] S. Schael. Cosmic positron spectrum measurement from 1 to 50 GeV with AMS-01. In *30th International Cosmic Ray Conferences*, 2007.

[99] P. Zuccon. The AMS Tracker Performance. In *29th International Cosmic Ray Conferences*, 2005.

[100] W. R. Leo. *Techniques for Nuclear and Particle Physics*. Springer-Verlag, 1987.